

Crustal structure and subduction erosion
in the central Costa Rica subduction zone

Dissertation
zur Erlangung des Doktorgrades
der Mathematischen-Naturwissenschaftlichen Fakultät
der Christian-Albrechts-Universität zu Kiel

vorgelegt von

Junjiang Zhu

Kiel, 2010

Referentin:

Prof. Dr. Heidrun Kopp

Koreferent:

Prof. Dr. Ernst Flueh

Tag der mündlichen Prüfung:

10. Februar 2010

Zum Druck genehmigt:

20. Juli 2010

Der Dekan

gez.

ABSTRACT

On the Pacific margin off central Costa Rica, an anomalous lens-shaped zone is located between the overriding plate and the subducting oceanic lithosphere approximately 25 km landward of the deformation front. This feature was previously recognized in reflection seismic data when it was termed ‘megalens’. Its origin and seismic velocity structure, however, could not unambiguously be derived from earlier studies. Therefore during RV SONNE cruise SO163 in 2002, seismic wide-angle data were acquired using closely spaced ocean bottom hydrophones and seismometers along two parallel strike lines and two parallel dip lines above the ‘megalens’, intersecting on the middle slope. In this study, the P-wave velocities and structure of the subducting oceanic Cocos Plate and overriding Caribbean Plate are determined from modeling of the wide-angle seismic data of cruise SO163. In addition, coincident reflection seismic data are analyzed and incorporated into the forward modeling and tomographic inversion of the refraction data. Based on the results of the velocity modeling, synthetic seismograms are calculated for an amplitude analysis of the refraction data to determine seismic attenuation variations across the seaward extent of the margin.

The margin wedge is defined by high seismic velocities (4.3-6.1 km/s) identified within a wedge-shaped body covered by a slope sediment drape. It is divided into two layers with different velocity gradients. Seismic velocities of the upper margin wedge vary from 4.0 to 4.3 km/s near the trench to 4.0-5.1 km/s close to the shoreline. The lower margin wedge is clearly constrained by decreasing velocities towards the trench and terminates beneath the middle slope at the location of the ‘megalens’. Seismic velocities of the ‘megalens’ are lower (3.8-4.3 km/s) relative to the margin wedge, implying that the ‘megalens’ represents hybrid material composed of subducted sediment and eroded fragments from the base of the upper plate. Upward-migrating overpressured fluids weaken the base of the margin wedge through hydrofracturing,

thus causing material transfer from the upper plate to the lower plate. Results from amplitude modeling confirm that the ‘megalens’ observed off central Costa Rica is bound by a low velocity zone documenting fluid drainage from the plate boundary to the upper plate.

Seismic attenuation of the central Costa Rica margin wedge is determined from amplitude analysis of the wide-angle seismic data. Travel time and amplitude modeling is applied to ocean bottom hydrophones along two trench-parallel profiles, located 30 km (P21&P22) and 35 km (P18) landward of the deformation front northeast of Quepos Plateau. Tomographic inversion images a progressively thinning margin wedge from the coast to the lower slope at the trench. A 1-1.5 km thick décollement zone with seismic velocities of 3.5-4.5 km/s is sandwiched between the margin wedge basement and the subducting Cocos plate. For strike line P21, amplitude modeling indicates a Q_p value of 50-150 for the upper margin wedge with velocities of 3.9-4.9 km/s. Along strike line P18, Q_p values of 50-150 are determined with velocities of 4.3-5.0 km/s in the upper margin wedge, increasing to 5.1-5.4 km/s in the lower margin wedge. Quantitative amplitude decay curves support the observed upper plate Q_p . In conjunction with earlier results from offshore Nicoya Peninsula, our study documents laterally landward decreasing attenuation across the margin wedge, consistent with a change in lithology from the sediment-dominated frontal prism to the igneous composition of the forearc middle prism.

ZUSAMMENFASSUNG

Am pazifischen Kontinentalrand vor zentralen Costa Rica, etwa 25 km landwärts der Deformationsfront, befindet sich eine linsenförmige Struktur zwischen der abtauchenden und der überfahrenden Platte. Diese als "Megalinse" bezeichnete Struktur wurde zunächst Ende der neunziger Jahre des letzten Jahrhunderts in seismischen Reflexionsdaten identifiziert; ihr Ursprung und ihre seismische Geschwindigkeitsstruktur sind jedoch nach wie vor unklar. Im Rahmen der FS SONNE Fahrt SO163 im Jahr 2002 wurden daher vier weitwinkelseismische Kreuzungsprofile im Bereich der "Megalinse" abgeschossen. Die Geschwindigkeitsmodellierung der aufgenommenen Ozeanbodenhydrophon- und Ozeanbodenseismometerdaten ergibt, unter Einbeziehung der Reflexionsdaten, die detaillierte P-Wellen Geschwindigkeitsstruktur der abtauchenden Cocos Platte und der überfahrenden Karibischen Platte. Aufbauend auf den Ergebnissen der Geschwindigkeitsmodellierung wurden im Rahmen einer Amplitudenanalyse synthetische Seismogramme erstellt, welche die räumliche Variation der seismischen Dämpfungsparameter im seewärtigen Teil der Oberplatte dokumentieren. Der marine Bereich des Kontinenthangs weist hohe seismische Geschwindigkeiten auf ($V_p=4.3-6.1$ km/s) und besteht aus einer keilförmigen Struktur, überdeckt von einer dünnen Schicht Hangsedimente. Er ist unterteilt in einen oberen und unteren Bereich mit jeweils unterschiedlichen Geschwindigkeitsgradienten. Der untere Bereich des Forearc-Keils ist gekennzeichnet durch landwärts zunehmende Geschwindigkeiten und endet mit dem Auftreten der "Megalinse". Die "Megalinse" ist eine Inversionsstruktur mit Geschwindigkeiten von 3.8-4.3 km/s, die als eine Ansammlung von subduzierten Sedimenten und erodiertem Material von der Unterkante der Oberplatte interpretiert wird. Durch Entwässerungsprozesse in den subduzierten Sedimenten freigesetzte und aufwärts migrierende Fluide, unter hohen Drücken stehend, führen zur Erosion darüberliegender Gesteinsschichten und damit zum Materialtransfer von der Ober- zur Unterplatte. Die Ergebnisse der Amplitudenmodellierung zeigen, dass die "Megalinse" von einer Niedriggeschwindigkeitsschicht umgeben ist, was auf entsprechende Entwässerungsvorgänge entlang der Plattengrenze hindeutet.

In dieser Arbeit wird die seismische Attenuation (Q_p) des unteren Kontinentalhanges vor Costa Rica aus der Amplitudenanalyse zweier parallel zum Tiefseeegraben verlaufender weitwinkelseismischer Profile abgeleitet. Für jeweils ein 30 km (P21&P22) und ein 35 km (P18) landwärts der Deformationsfront verlaufendes Profil werden Laufzeit- und Amplitudenmodellierungen vorgestellt. Die tomographischen Modelle bestätigen die sukzessive Ausdünnung der Oberplatte von der Küste zum Tiefseeegraben. Die "Megalins" wird dabei als ein 1-1.5 km mächtiger Bereich des Décollements zwischen Ober- und Unterplatte mit seismischen Geschwindigkeiten von 3.4-4.5 km/s abgebildet. Der obere Kontinenthang ist auf Profil 21 durch Geschwindigkeiten von 3.9-4.9 km/s und Q_p Werte von 50-150 gekennzeichnet. Für Profil 18 ergeben sich entsprechende Geschwindigkeitswerte von 4.3-5.0 km/s und Q_p Werte von 50-150 sowie Geschwindigkeiten von 5.1-5.4 km/s für den tieferen Bereich des Kontinentrands. Die ermittelten Q_p -Werte auf beiden Profilen stehen im Einklang mit quantitativen Amplitudenverlaufskurven. Unter Berücksichtigung früherer Arbeiten vor der Nicoya Halbinsel bestätigen die Ergebnisse eine landwärtige Zunahme der seismischen Attenuation und damit den lithologischen Wechsel vom überwiegend sedimentären frontalen Prisma zum krustalen Bereich des mittleren Forearcs.

ABSTRACT IN CHINESE

科学是永无止境的，它是一个永恒之谜

——爱因斯坦

摘要

在中哥斯达黎加太平洋边缘，有一棱镜体形状异常体存在上驮板块和俯冲岩石圈之间，距离向陆方向的变形前锋大约 25 公里。这个异常体在以前的反射地震数据中有所显示，被称为“巨大棱镜体”。然而它的来源和速度结构不能清晰地被早期的研究解决。因此 2002 年太阳号 (SONNE163) 开展了一个广角地震探测航次，在“巨大棱镜体”的上部，沿两条平行走向测线和两条平行倾向测线，按大约 2.5 公里的间距布设海底水听器 (OBH) 和海底地震仪 (OBS) 来获取广角地震数据，测线交叉于中斜坡的位置。在此次研究中，通过模拟广角地震数据，确定了俯冲带 P 波速度结构，获得了详细的俯冲可可大洋板块和上驮加勒比海板块的速度结构。此外，走时正演模拟和广角数据的层析成像反演的过程中充分地利用了多道地震反射数据。依据速度模拟结果，综合地震图被计算并用于分析向海延伸边缘楔的折射数据的侧向振幅变化。楔形的边缘楔展示了高的地震波速度 (4.3–6.1 km/s)，并被斜坡沉积物覆盖。由于不同的速度梯度，边缘楔分为两层 (上边缘楔和下边缘楔)，上边缘楔的地震速度靠近海沟变化从 4.0–4.3 km/s 到靠近海岸的 4.0–5.1 km/s，下边缘楔也被清晰的束缚，表现为向着海沟地震波速度降低和延伸终止在下斜坡底部“巨大棱镜体”的位置。“巨大棱镜体”的地震波速度相对于边缘楔是低的 (3.8–4.3 km/s)，暗示着“巨大棱镜体”代表着俯冲沉积物和来自上部板块底部剥蚀物质的混合组成。向上偏移的超压流体通过水破裂机制软化了边缘楔的底部，因此引起了物质从上部板块运输到下部板块。振幅模拟的结果证实了在哥斯达黎加滨海观察的“巨大棱镜体”被低速层包围并记录了流体排泄从板块边界到上部板块。

通过广角地震数据的振幅分析，确定了中哥斯达黎加边缘楔的地震衰减变化。走时和振幅模拟被应用于两条平行于海沟的海底地震水听器剖面，一条 (剖面 P21) 位于 Quepos 高地东北部变形前锋 30 公里，另一条位于 35 公里。层

析成像反演影像了边缘楔厚度从海岸到海沟的下斜坡逐渐减薄。1-1.5 公里厚的 *décollement* 带是夹在边缘楔基底和俯冲可可板块之间，地震波速度是 3.5-4.5 km/s。沿走向线 (P21)，振幅模拟结构展示了上边缘楔的 Q_p 值是 50-150，地震波速度是 3.9-4.9 km/s。沿走向线 (P18)，振幅模拟结构展示了上边缘楔的 Q_p 值是 50-150，地震波速度是 4.3-5.0 km/s，下边缘楔地震波速度增加从 5.1-5.4 km/s。定量振幅亏损曲线支持上边缘楔的 Q_p 值。结合早期的尼科亚半岛滨海的地震衰减的结果，我们的研究记录了边缘楔的地震衰减侧向向陆减小，结果证实了从沉积物控制的前楔 (Frontal prism) 到花岗岩组成的弧前中楔 (Middle prism) 岩性的变化。

Contents

ABSTRACT	V
ZUSAMMENFASSUNG	VII
ABSTRACT IN CHINESE	IX
1 Introduction	6
2 Geology and Tectonic Setting	10
2.1 Regional Tectonic Framework and Geology	10
2.1.1 Geological Evolution and Plate Reconstruction of Central America	10
2.1.2 Chorotega Block	12
2.2 Overview of Previous Seismic Studies	17
2.2.1 Seismic Structure	17
2.2.2 Subduction Erosion and Accretion	20
2.2.3 Fluids and Seeps at the Continental Slope.....	22
3 Methods	25
3.1 Forward Ray Tracing Method	25
3.2 Travel-time Tomography Method	26
3.2.1 Forward Traveltime Calculation	27
3.2.2 Traveltime Inversion	28
4 Crustal Structure of the central Costa Rica Subduction Zone: Implications for Basal Erosion from Seismic Wide-angle Data	31
4.1 Introduction	31
4.2 Geodynamic Setting	33
4.3 Wide-angle Experiment	35

4.3.1	Data Acquisition and Processing	35
4.3.2	Modeling	35
4.3.2.1	Forward Modeling	35
4.3.2.2	Amplitude Modeling	36
4.4	Interpretation	37
4.4.1	Dip-lines SO163-P15 and SO163-P24	37
4.4.1.1	Sediment	37
4.4.1.2	Upper and Lower Margin Wedge	43
4.4.1.3	“Megalens” and Low Velocity Zone	45
4.4.1.4	Upper and Lower Oceanic Crust	45
4.4.2	Strike-lines SO163-P18 and SO163-P22	46
4.4.3	Amplitude Modeling of Wide-angle Data	51
4.4.4	Model Sensitivity and Uncertainty Tests	52
4.5	Discussion	55
4.5.1	Margin Wedge	55
4.5.2	“Megalens” and LVZ	56
4.5.3	Subducted Oceanic Crust	57
4.5.4	The Nature of the “Megalens”	58
4.6	Conclusions	59
5	Margin Architecture and Seismic Attenuation in the central Costa Rican Forearc	62
5.1	Introduction	62
5.2	Wide-angle Seismic Data.....	64
5.3	Seismic Travel Time Tomography	67
5.3.1	Method	67
5.3.2	Results of Tomographic Inversion and Interpretation	69
5.3.2.1	Seismic Structure	69
5.3.2.2	Model Uncertainty and Resolution Tests	71
5.4	Reflectivity Method	75
5.4.1	Strike Line P18 and Line P21.....	76

5.4.2	Quantitative Estimation of Qp Values	79
5.4.3	Uncertainty Estimations of Seismic Attenuation	82
5.5	Discussion	84
5.6	Conclusions	86
6	Conclusions and Outlook	87
	Acknowledgments	90
	Bibliography	91
	Appendix	106
	Curriculum Vitae	128

List of Figures

1.1	Subduction zone system in Central America.....	8
2.1	Schematic cross section of plate tectonics.....	11
2.2	Tectonic setting of Central America.....	12
2.3	Tectonic evolution model of the eastern Pacific and Caribbean.....	13
2.4	The evolutionary model of the Chorotega block.....	14
2.5	Geological map of southern Costa Rica.....	16
2.6	Crustal structure across the Middle American landbridge.....	18
2.7	Crustal structure obtained from previous wide-angle data.....	19
2.8	Schematic cartoons of erosive and accretionary margins.....	21
2.9	Generic subduction erosion model.....	22
2.10	Seismic images of the megalens.....	24
3.1	Schematic diagram of 2D ray tracing	25
3.2	Ray calculation based on different methods	28
4.1	Tectonic setting of the Central America convergent margin.....	32
4.2	Location map of seismic wide-angle profiles.....	34

4.3	Time migrated section of SO81 Line 4.....	34
4.4	Detailed location map of wide-angle profiles in this study.....	37
4.5	Four velocity-depth models along the Pacific margin of central Costa Rica.....	38
4.6	Record section from station OBS52.....	39
4.7	Record section and ray diagram for station OBH56.....	40
4.8	Record section and ray diagram for station OBS57.....	41
4.9	Record section and ray diagram for station OBS96.....	42
4.10	Record section and ray diagram for station OBS106.....	43
4.11	Ray coverage of the lower margin wedge displayed for dip-line P24.....	44
4.12	Record section and ray diagram for station OBH65.....	47
4.13	Record section and ray diagram for station OBH74.....	48
4.14	Record section and ray diagram for station OBS79.....	49
4.15	Record section and ray diagram for station OBH86.....	50
4.16	1-D reflectivity modelling for OBH 88.....	52
4.17	Sensitivity tests of the velocity and the geometry of the megalens.....	53
4.18	Standard deviations for velocity and reflector depth nodes.....	55
4.19	Seismic image and the interpretative velocity structure.....	60
5.1	Location map of seismic refraction profiles discussed in this study.....	63
5.2	Record section and raypaths for OBH53 deployed on profile P15.....	65
5.3	Record section and raypaths for OBH64 deployed on strike line P18.....	66
5.4	Record section and raypaths for OBS66 deployed on strike line P18.....	68
5.5	Velocity-depth distributions for profiles P15 and P24.....	70
5.6	Velocity-depth distributions for profiles P18 and P22.....	71
5.7	Upper plate resolution test for profile P15.....	73
5.8	Standard deviations for velocity and reflector depth nodes of profile P24.....	74
5.9	Frequency spectrum of OBS 68.....	77
5.10	Amplitude-distance curves for models m1, m2, and m3.....	78
5.11	Record section and synthetic seismograms of strike line P18 and P21.....	80
5.12	Amplitude versus offset variations for refracted phases.....	83
A.1.	Dip line P15, OBS48.....	107
A.2.	Dip line P15, OBH58.....	108
A.3.	Dip line P24, OBH98.....	109

A.4. Dip line P24, OBH103.....	110
A.5. Dip line P24, OBH104.....	111
A.6. Strike line P18, OBH69.....	112
A.7. Strike line P18, OBH71.....	113
A.8. Strike line P22, OBH78.....	114
A.9. Strike line P22, OBH80.....	115
A.10. Strike line P22, OBS84.....	116
A.10. Strike line P22, OBS85.....	117
A.11. Strike line P22, OBH87.....	118
B.1. Monto Carlo analysis.....	119
C.1. Amplitude versus offset variations.....	120
D.1. Synthetic seismogram, OBH62.....	121
D.2. Synthetic seismogram, OBH73.....	122
D.3. Synthetic seismogram, OBH76.....	123
D.4. Synthetic seismogram, OBH79.....	124
D.5. Synthetic seismogram, OBH87.....	125
D.6. Synthetic seismogram, OBH89.....	126
D.7. Synthetic seismogram, OBH90.....	127

List of Tables

Table 4.1. Phase nomenclature for wide-angle arrivals.....	36
Table 5.1. Model parameters.....	77
Table 5.2. Margin wedge velocities and Qp values	85
Table A.1. Phase nomenclature for wide-angle arrivals.....	105

Chapter 1

Introduction

The noble science of Geology loses glory from the extreme imperfection of the record. The crust of the earth with its imbedded remains must not be looked at as a well-filled museum, but as a poor collection made at hazard and at rare intervals. The accumulation of each great fossiliferous formation will be recognized as having depended on an unusual concurrence of favourable circumstances, and the blank intervals between the successive stages as have been vast duration.

Charles Darwin in “The origin of species by means of natural selection”, November 24th, (1859). *Page. 303, vol. 2.*

Central America is an area of high tectonic activity resulting from the subduction of the Cocos plate beneath the Caribbean plate along the Middle America Trench (Molnar and Sykes, 1969). It shows large lateral variations over relatively short distances regarding the structure of the incoming oceanic plate, overriding plate, seismicity and arc volcanism. Considering these aspects, Central America provides an excellent natural laboratory to study subduction zone processes at a variety of scales.

The collaborative research center SFB574 in Kiel has focused on volatiles and fluids in the Central America subduction zone since 2001 (Fig. 1.1). Many disciplines including geophysics, seismology, geochemistry, geology and other inter-disciplines contribute to the research along this erosive margin. In this study, I analyzed marine geophysical data acquired during RV SONNE cruise SO163 in 2002 to investigate the fine seismic structure of the central Costa Rica subduction zone, especially focusing on an anomalous local structure termed ‘megalens’ by Flueh et al. (1999) and Ranero et al. (2000). On the previously recorded seismic reflection profile SO81 Line 4, this feature shows a strong plate-boundary reflection, which bifurcates 25 km landward of the trench at about 5 s two-way travel time.

Based on a priori information and an extensive refraction data set, this thesis addresses the following scientific questions:

1. How does the ‘megalens’ relate to basal erosion processes off central Costa Rica?
2. What is the physical nature of this feature as evidenced from seismic data?
3. What is the lateral seismic velocity variation of the margin wedge off Costa Rica?
4. To what degree do physical property variations influence seismic attenuation along the lower slope?

To tackle these questions, I firstly obtained the seismic structure of the central Costa Rica forearc, and subsequently analyzed its seismic properties.

The thesis is organized as follows:

Chapter 2 describes the geological and kinematic evolution of Central America under the influence of the Galápagos hotspot from Miocene to present times. The evolutional model of the Chorotega block including all of Costa Rica and western Panama since late Cretaceous to present is presented based on the results of Berrange and Thorpe (1988). Significant geomorphic features of the fore-arc, volcanic front and back-arc provinces are outlined and previous seismic studies of onshore and offshore experiments are summarized. Moreover, in central Costa Rica, the detailed seismic structure obtained from the previously acquired wide-angle profiles is presented. Studies and recent models of subduction erosion and accretion in convergent margins are indicated. In addition, different mechanisms of subduction erosion are reviewed using Costa Rica for benchmark studies. Finally, the effect of fluids along the continental slope and plate boundary is discussed.

Chapter 3 provides an overview of the seismic methods that I used during the thesis. The forward modeling technique using the “MacRay” tool (Luetgert, 1992) is employed to obtain the seismic velocity structure (Chapter 4). Subsequently, the travel time tomography method (Korenaga et al., 2000) is applied to the refraction data. The algorithms and equations of travel time calculation used in these methods are introduced in this chapter. The amplitude modeling (reflectivity method) is

presented in Chapter 5.

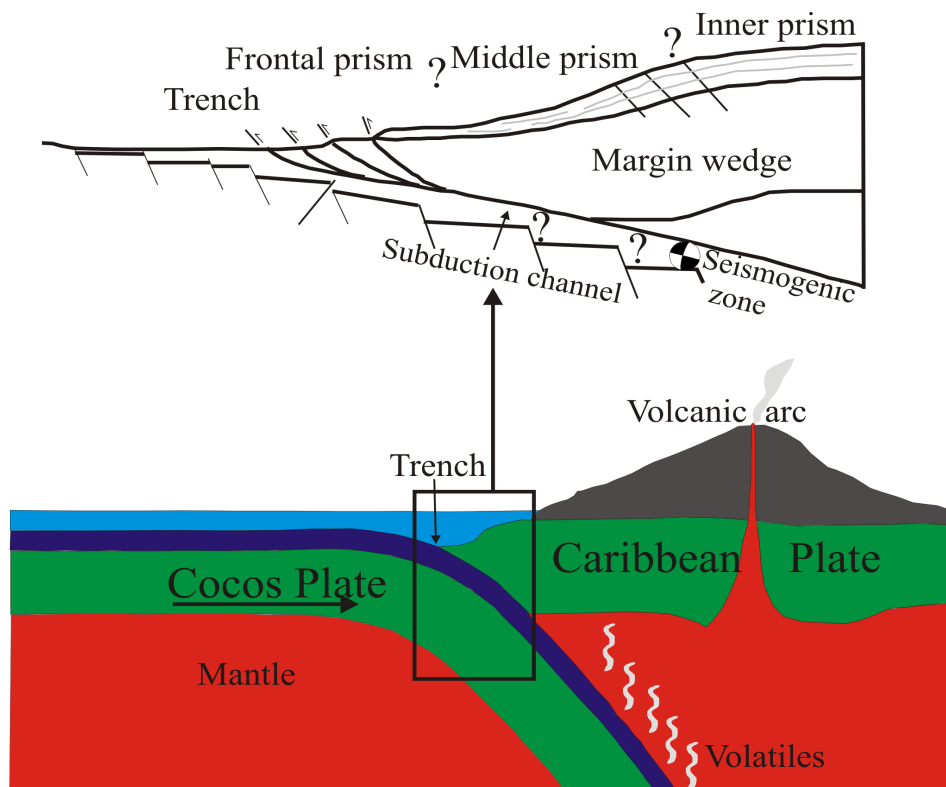


Figure 1.1 Subduction zone system in Central America. The upper panel presents the tectonic units of the convergent margin (modified after von Huene et al., 2009).

Chapter 4 presents the crustal structure of the central Costa Rica subduction zone. This Chapter as well as Chapter 5 are in the form of journal manuscripts. Chapter 4 was published in *Geophysical Journal International*, v178, p. 1112-1131, 2009. Forward modeling results of two dip lines P15 and P24 and two strike lines P18 and P22 are presented and interpreted in this chapter. The structure of the ‘megalens’ found on the seismic image SO81 Line 4 is discussed. The results show that the wide-angle data clearly define two layers within the margin wedge: the high velocity gradient upper margin wedge with velocities of 4.3-5.0 km/s and the reduced velocity gradient lower margin wedge with velocities ranging from 5.2-6.1 km/s. As documented by the two strike lines, the leading edge of the lower margin wedge terminates above the ‘megalens’ about 32 km landward of the trench. The ‘megalens’ is 15-20 km wide and has a thickness of 1-1.5 km. Its seismic velocities fall between 3.8 km/s and 4.3 km/s and are clearly much lower than the velocities of subducted

seamounts or plateaus. The ‘megalens’ is a low velocity body with respect to the margin wedge above and is bounded by thin layers of lower velocities above and below. Our preferred interpretation is that the ‘megalens’ is a mixture product, which consists of a buried sedimentary mélangé including rocks sheared from the lower plate and highly fractured material derived by basal erosion from the upper plate. The low velocity zone above the ‘megalens’ is characterized by a discontinuous amplitude distribution in the seismic image which is likely caused by fluids and associated localized pore pressure anomalies.

As mentioned previously, Chapter 5 is also in manuscript form; it is in press with *Marine Geology* (2010). Chapter 5 describes the seismic attenuation variations of the margin wedge in central Costa Rica determined from amplitude analysis of wide-angle seismic data. The wide-angle data and synthetic data provide unambiguous measurements of seismic amplitude decay of the first arrivals of the margin wedge. Travel time and amplitude modeling is applied to ocean bottom hydrophones along two trench-parallel profiles, located 30 km (P21&P22) and 35 km (P18) landward of the deformation front northeast of Quepos Plateau. Tomographic inversion images a progressively thinning margin wedge from the coast to the lower slope at the trench. The 1-1.5 km thick décollement zone, which was previously resolved during the forward modeling, displays seismic velocities of 3.5-4.5 km/s and is sandwiched between the margin wedge basement and the subducting Cocos plate. For the strike line P21, amplitude modeling indicates a Q_p value of 50-150 for the upper margin wedge with velocities of 3.9-4.9 km/s. Along the strike line P18, similar Q_p values of 50-150 are determined with velocities of 4.3-5.0 km/s in the upper margin wedge, increasing to 5.1-5.4 km/s in the lower margin wedge. Q_p values of 50-150 for the strike lines are supported by quantitative amplitude decay curves. In conjunction with earlier results from offshore Nicoya Peninsula, our study documents landward decreasing attenuation across the lower margin wedge, consistent with a change in lithology from the sediment-dominated frontal prism to the igneous composition of the forearc middle prism.

Chapter 2

Geology and Tectonic Setting

2.1 Regional Tectonic Framework and Geology

2.1.1 Geological Evolution and Plate Reconstruction of Central America

The concept of plate tectonics, as a description of relative motions of those parts of the Earth's outer shell that are internally semirigid, has been proven and the plate tectonic circulation is largely or entirely limited to the upper mantle shallower than the discontinuity near 660 km (Hamilton, 2007). Hamilton (2007) addressed that Earth was highly fractionated very early in its history, and its subsequent evolution, understood to be a consequence of changes enabled by cooling, has involved progressive enrichment of the upper mantle by downward recycling of crustal materials back into it. Most movement occurs along narrow zones between plates where the results of plate-tectonic forces are most evident, and four types of plate boundaries (divergent boundaries, convergent boundaries, transform boundaries and plate boundary zones) have been identified in the earth sciences (Kious and Tilling, 1996) (see also Figure 2.1) and are discussed by Bird (2003).

The early history of Central America is characterized by the opening of a spreading center between North and South America sometime after about 170 Ma (more probably 130 Ma) following the Late Triassic-Jurassic break-up of Pangaea (Mann et al., 2007). The North and South American plates are moving westward in response to seafloor spreading along the Mid-Atlantic ridge, and are overtaking the eastern margins of the Caribbean plate, which are drifting slowly to the southeast. The Cocos plate is moving towards the northeast, and the northern edge of the Nazca plate is moving northward, in both cases subducting beneath the Caribbean plate. The collision of the Cocos and Caribbean plates is manifested in the Middle America trench (MAT) that parallels the Pacific coast. The collision results in crustal instability and tectonic activity, evidenced primarily as earthquakes and volcanism, which are

fundamental elements of Central American geomorphology (Bundschuh et al., 2007). The present plate configuration is presented in Figure 2.2.

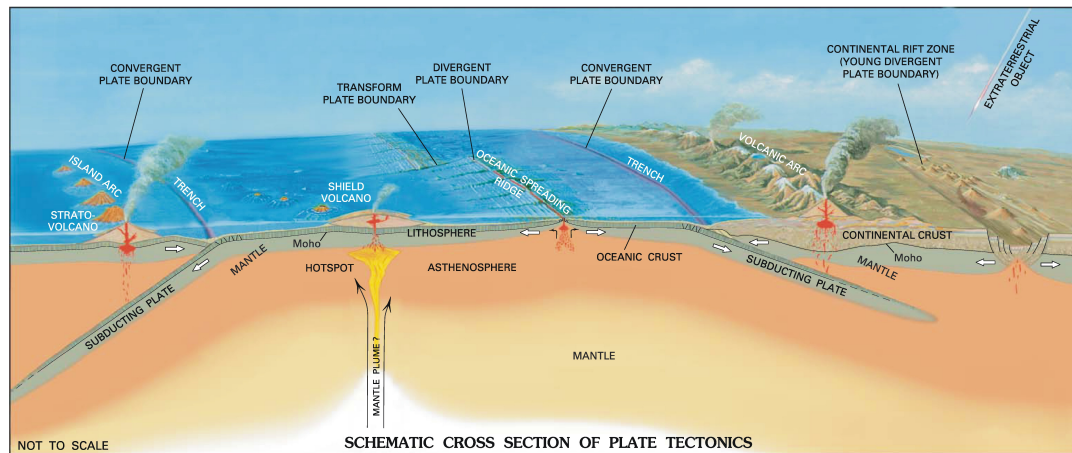


Figure 2.1. Schematic concept of plate tectonics (from Simkin et al., 1989).

The Galápagos hotspot plays a fundamental role in the plate tectonic evolution of the eastern Pacific and Caribbean and also in the development of land bridges between the Americas. Sampling results from Malpelo Island and accreted igneous complexes in Central America show that the Galápagos hotspot was active from 16-71 Ma, confirming that the Caribbean large igneous province formed from the Galápagos hotspot and that the Caribbean plate originated in the Pacific (Hoernle et al., 2002). A tectonic model for the evolution of the eastern Pacific and Caribbean for past 90 m.y. was reconstructed (Hoernle et al., 2002) and presented in Figure 2.3. In the Jurassic, North America separated from Gondwana (southern supercontinent) and drifted to the northwest. Africa and South America began drifting apart ca. 130 Ma, leaving South America as a continental island. The Caribbean oceanic plateau formed above the Galápagos hotspot and began to drift northeastward toward the Greater Antilles arc ca. 85 Ma. The thick and young oceanic plateau choked east-dipping subduction beneath the Greater Antilles trench ca. 70-75 Ma, causing uplift of the arc and the formation of a land bridge between the Americas in the latest Cretaceous. The Caribbean large igneous province inserted between the Americas in the early Paleocene (Hoernle et al., 2002). The present Galápagos islands are 3–4 m.y. old (e.g., White et al., 1993). At present, Central America is bounded by the MAT and

subduction system to the southwest and the strike-slip faults of the Motagua-Swan islands to the north, and it is attached to the stable Caribbean plate to the east and southeast (Mann et al., 2007, Figure 2.2).

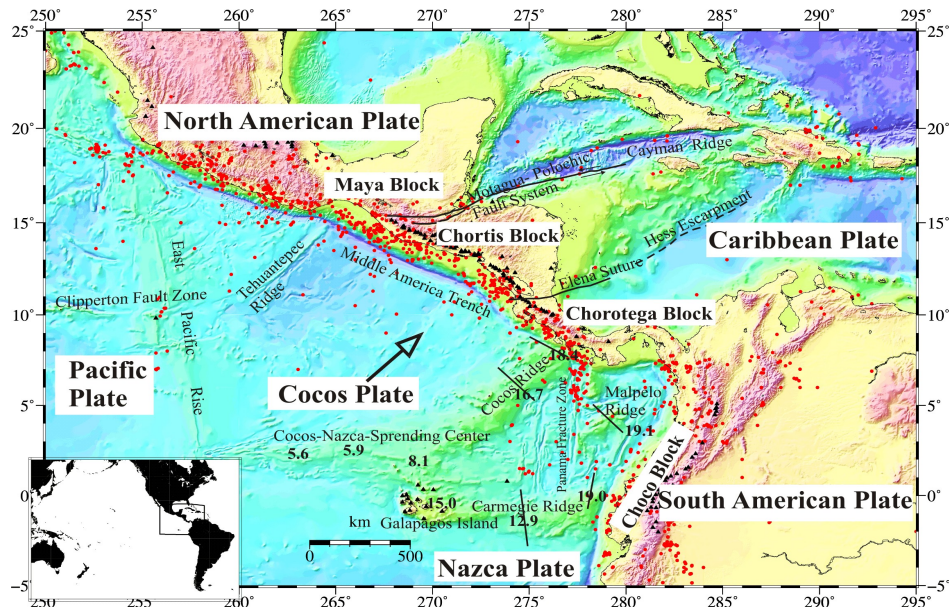


Figure 2.2. Tectonic setting of Central America. Red dots show the earthquakes ($M > 6.0$) from 1960 to 2009 (data from IRIS event catalogs, <http://www.iris.edu/data/event/eventsearch.htm>). Black triangles show the locations of volcanoes (data from the Smithsonian Institution Global Volcanism Program "Volcanoes of the World" <http://www.volcano.si.edu/gvp/>). Bathymetric data is the GEBCO one-minute grid (http://www.gebco.net/data_and_products/). Several aseismic ridges were investigated by active seismic experiments and the black lines show the locations of these seismic profiles and the numbers indicate crustal thickness (Sallares and Charvis, 2003).

2.1.2 Chorotega Block

Central America is segmented into four major structural regions: the Maya, Chortis, Chorotega and Choco blocks (Dengo, 1985; Escalante, 1990, detailed location in Fig. 2.2). Most of southern Central America consists of a Neogene-Quaternary volcanic belt that overlies the Mesozoic oceanic basement of Caribbean plate origin (Weyl, 1980; Dengo, 1985; Escalante, 1990). This region is referred to as

the Chorotega Block, which includes all of Costa Rica and western Panama. The detailed physiographic provinces of the Chorotega blocks were defined and characterized by Marshall et al., (2007).

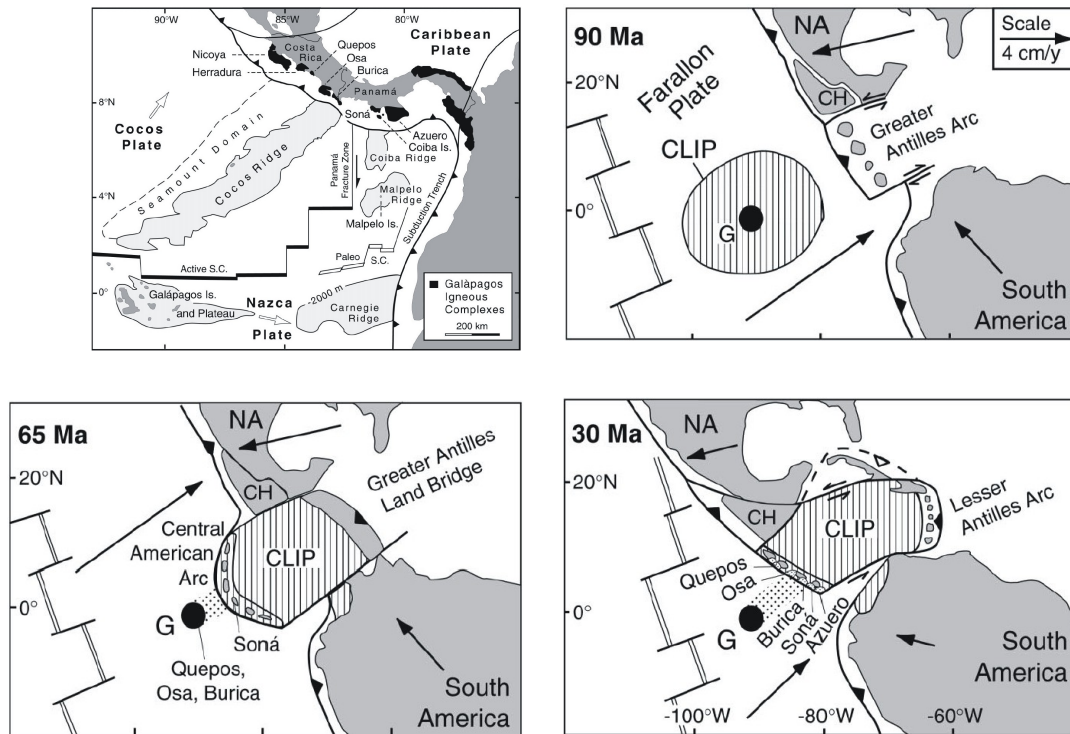


Figure 2.3. Tectonic evolution model of the eastern Pacific and Caribbean (~90 m.y.) (after Hoernle et al., 2002) illustrating the role of the Galápagos hotspot. The Galápagos island and hotspot tracks (Cocos, Coiba, Malpelo, and Carnegie Ridges) and the igneous complex in Central America with the Galápagos geochemical affinities are shown in the left corner panel.

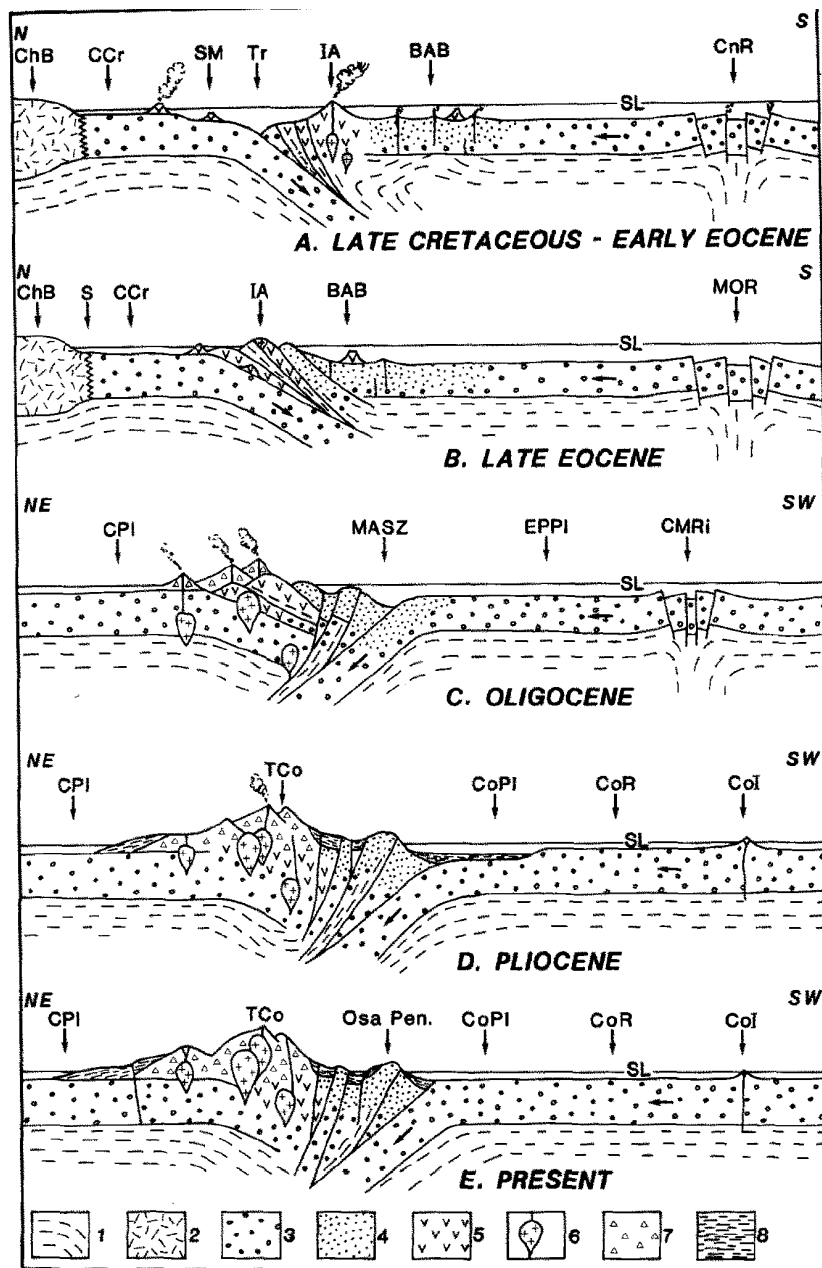


Figure 2.4. The evolutionary model of the Chorotega block of the Southern Central America Orogen (from Berrange and Thorpe, 1988). 1. mantle peridotite; 2. continental crust; 3. oceanic crust, undifferentiated; 4. oceanic crust, back-arc type; 5. oceanic crust, early basaltic island arc and off-arc volcanic type; 6. intrusion (mafic to silicic composition); 7. late andesitic volcanic and volcanoclastic rocks; 8. sediments. BAB-Back-arc basin; CCr-Caribbean crust; ChB-Chortis block; CMRi-Clipperton-Mathematicians Ridge; CnR-Carnegie Ridge; CoI-Cocos Island; CoPI-Cocos plate; CoR-Cocos Ridge; CPI-Caribbean plate; EPPI-East Pacific plate; IA-Island arc; MASZ-Middle America Subduction Zone; S-suture; SM-seamount; SL-sea level; Tr-trench.

The main geomorphic-tectonic units of Costa Rica comprise the forearc province, the active volcanic front and backarc region:

1. Forearc province: it extends along the Pacific coast from Costa Rica's Santa Elena peninsula in the north to the Gulf of Panama in the south, highly segmented with sharp contrasts in structure and coastal morphology linked to variations in the subducting Cocos and Nazca plates offshore.
2. Volcanic front province: In Costa Rica, a dynamic history of Cenozoic tectonics generated a complex volcanic belt that includes the Guanacaste, Tilarán, Aguacate, Central, and Talamanca cordillera. Spatial and temporal variations in the subduction system have led to sharp contrasts in magma chemistry and eruption style along the length of the Chorotega volcanic front (Carr, 1984).
3. Backarc province: it extends from the vast Caribbean plains of the Tortuguero lowlands in northeastern Costa Rica to the abrupt emergent shoreline of the southern Limón and Bocas del Toro basins near the Costa Rica-Panama border. The sharp geomorphic contrast between these regions reflects a sudden shift along the backarc from the stable tectonics in the north to active crustal deformation within the North Panama deformed belt in the south (Marshall et al., 2007).

Figure 2.4 summarizes the main evolution processes related to the Chorotega block since the late Cretaceous described by Berrange and Thorpe (1988). Although southern Costa Rica contains no active volcanoes, it was the locus of arc magmatism until fairly recently and the overall architecture of this area resembles a typical arc. It contains a back-arc basin (Limón basin), arc highlands region (Cordillera de Talamanca), inner fore-arc basin (Terraba Trough), fore-arc fold and thrust belt (Fila Costeña), and outer fore-arc basin (Burica and Osa peninsula) (Fig. 2.5).

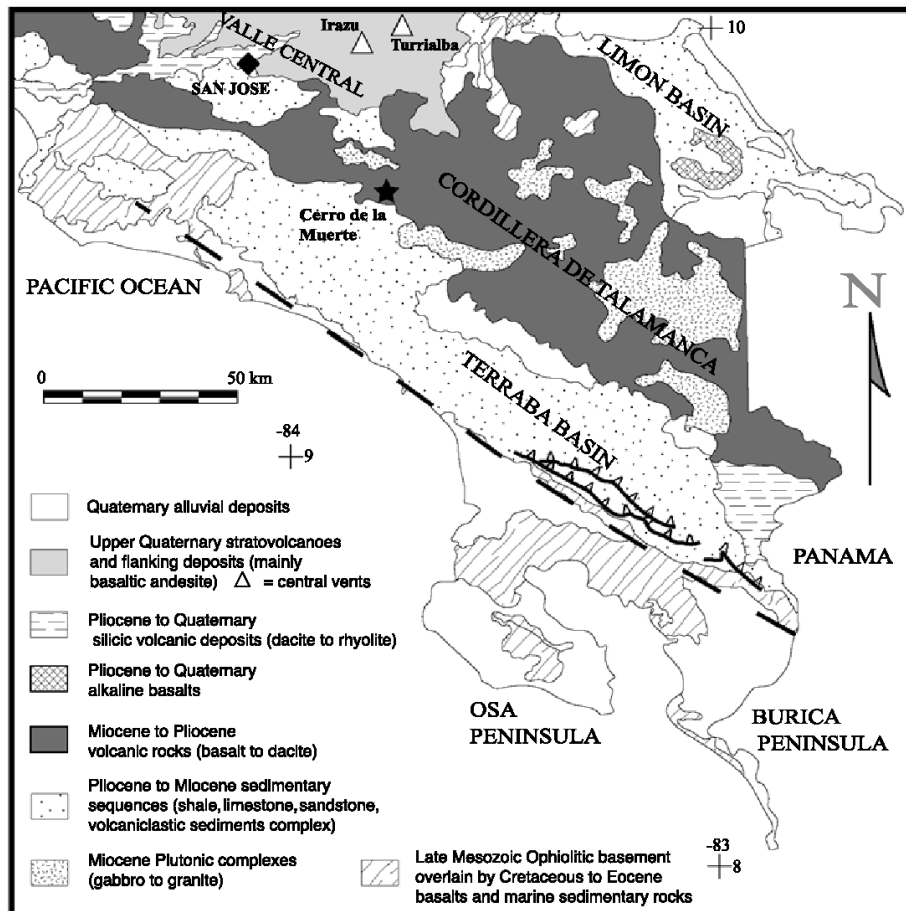


Figure 2.5. Geological map of southern Costa Rica (from MacMillan et al., 2004). Heavy line with barbs indicates thrust faults in the Fila Costeña. Heavy dashed line indicates the Ballena-Celmira Fracture Zone.

Offshore, the subduction of Cocos Ridge plays an important role for the geological evolution of Costa Rica (for location of Cocos Ridge see Figure 2.2). The Cocos Ridge and seamount samples have compositions similar to volcanic rocks from the Galápagos hotspot (Werner et al., 1998). The age of Cocos Ridge subduction beneath Costa Rica is still under debate (MacMillan et al., 2004). An age of 8 Ma was proposed based on the back-arc basalts (Abratis and Wörner, 2001). De Boer et al., (1995) suggested an age of 5 Ma based on a regional unconformity and the cessation of volcanism at ~3.5 Ma. A younger age of 3.5 Ma was proposed based on the differential subsidence and uplift rates in the fore-arc and back-arc, and ~1 Ma based on the uplift fore-arc marine terraces (Gardner et al., 1987, 1992), Lonsdale and Klitgord (1978) also proposed an age of 1 Ma based on the distribution of oceanic magnetic an-

omalies on the Nazca and Cocos plate.

2.2 Overview of previous seismic studies

2.2.1 Seismic Structure

A detailed review and summary of early seismic investigations are presented by Flueh and von Huene (2007). Early seismic refraction and reflection studies along the MAT (Fisher et al., 1961; Shor et al., 1961; Ross et al., 1965; Ibrahim et al., 1979) indicated a comparatively simple seismic structure. However, processing and interpretation were limited due to computer techniques and methods. The deep crustal structure was first investigated by Matumoto et al., (1977) based on seismic data in southern Central America. The results indicated an about 43 km thick crust with a continental affinity beneath the volcanic province of northern Costa Rica. Four layers were identified with P-wave velocities of 2.6 km/s, 5.1 km/s, 6.2 km/s and 6.6 km/s and an upper mantle velocity is 7.9 km/s (Matumoto et al., 1977). Kim et al. (1982) indicated a three-layered crustal model in northern Central America based on shallow earthquakes along the Motagua Polochi fault in Guatemala recorded by a seismological station in Tegucigalpa, Honduras, and estimated a crustal thickness of 37.4 km. However, Ligoría and Molina (1997) indicated a thicker continental crust (about 50 km). These studies have some limits due to the small number of instruments that recorded a few widely separated explosive sources or local earthquakes (Flueh and von Huene, 2007). Since then, both onshore and offshore seismic investigations have well established the entire crustal structure across the Middle American landbridge on the Pacific margin of Nicaragua (Walther et al., 2000), in northern Costa Rica (Sallares et al., 1999; Sallares et al., 2001) and in southern Costa Rica (Stavenhagen et al., 1998). The results indicate a 40 km thick Costa Rica Isthmus crust (Sallares et al., 2001, Figure 2.6) similar to the previously reported Moho depths of 43 km (Matumoto et al., 1977). Crustal velocities increase from about 6.0 km/s at 5 km depth to 7.2 km/s at the Moho, and the velocity model reveals low mantle velocities between 7.3 km/s and 7.6 km/s supported by amplitude modelling of PmP critical distances (Sallares et al., 2001, in Figure 2.6). Stavenhagen et al., (1998) presented a thick low velocity zone (up to 6 km) above the downgoing plate constrained by the delay of the mantle phases. Due to the limited ray coverage and limited profile lengths, the thickness of the crust beneath the forearc could not be constrained and the thickness of the downgoing oceanic crust indicated an anomalous thickness (about 14 km) compared to normal oceanic thickness (White et al., 1992). Walther et al., (2000) observed a mantle sliver beneath the landward flank of the

Sandino basin with velocities of 7.5 km/s at a shallow depth of 12-18 km (Figure 2.6). They interpreted the mantle sliver as a remnant of a former subducting slab. In summary, the crustal structure beneath the Central America landbridge shows a high degree of complexity and lateral variations from the Nicaragua Pacific margin to the southern Costa Rica margin.

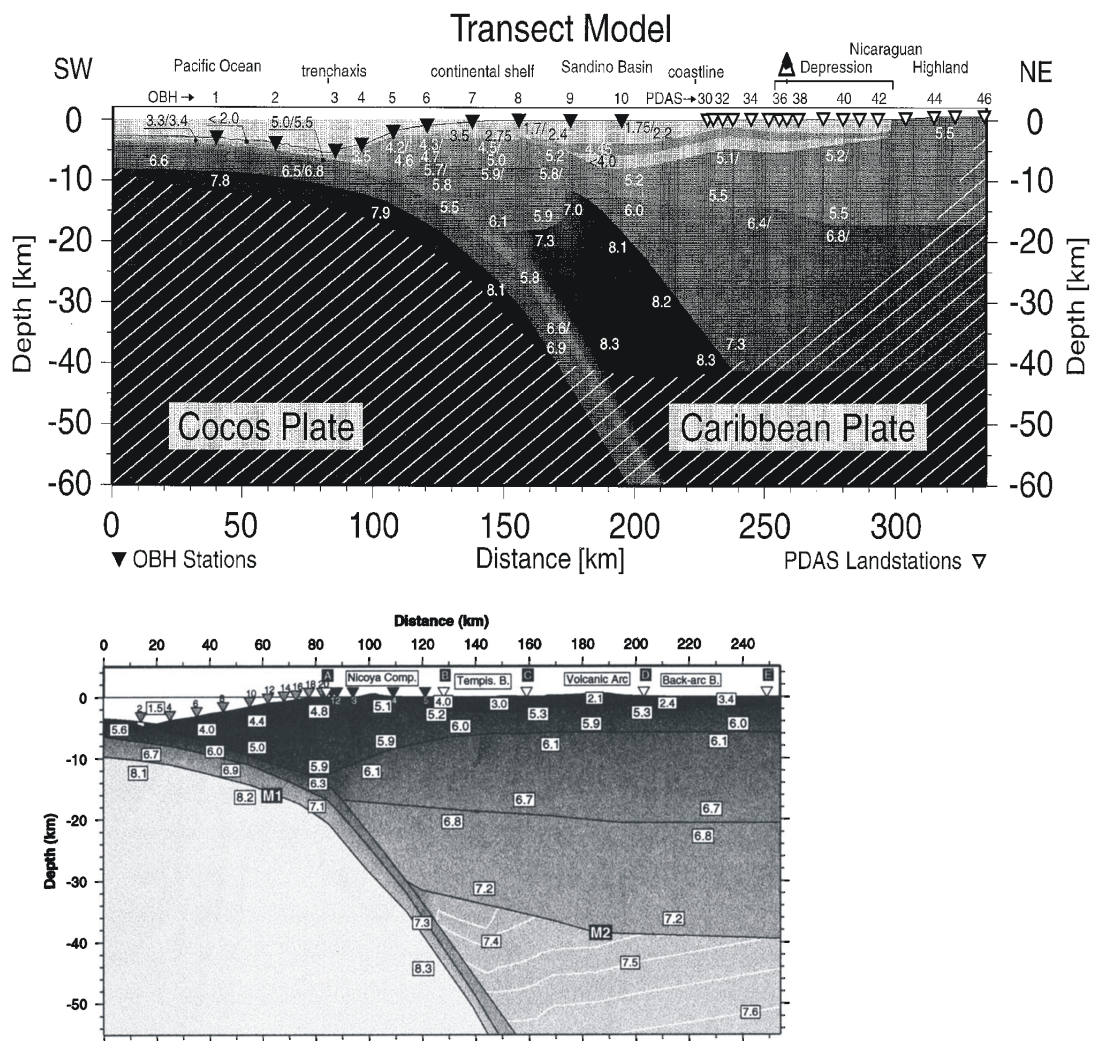


Figure 2.6. Crustal structure across the Middle American landbridge. The upper panel shows a transect on the Pacific margin of Nicaragua (Walther et al., 2000) and the lower panel shows a transect in northern Costa Rica (Sallares et al., 2001)

In the following, we briefly summarize some features of the seismic structure

in central Costa Rica mainly based on the numerous wide-angle seismic profiles deployed since 1996 (Ye et al., 1996; Stavenhagen et al., 1998; Christeson et al., 1999; Walther et al., 2003; Zhu et al., 2009) (Fig. 2.7). The results of these investigations reveal the crustal structure of the subduction zone. The age, thickness and seismic velocities of the downgoing plate vary from the Nicoya Peninsula in the northwest to the Osa Peninsula in the southeast (Fig. 2.7). In general, the thickness of

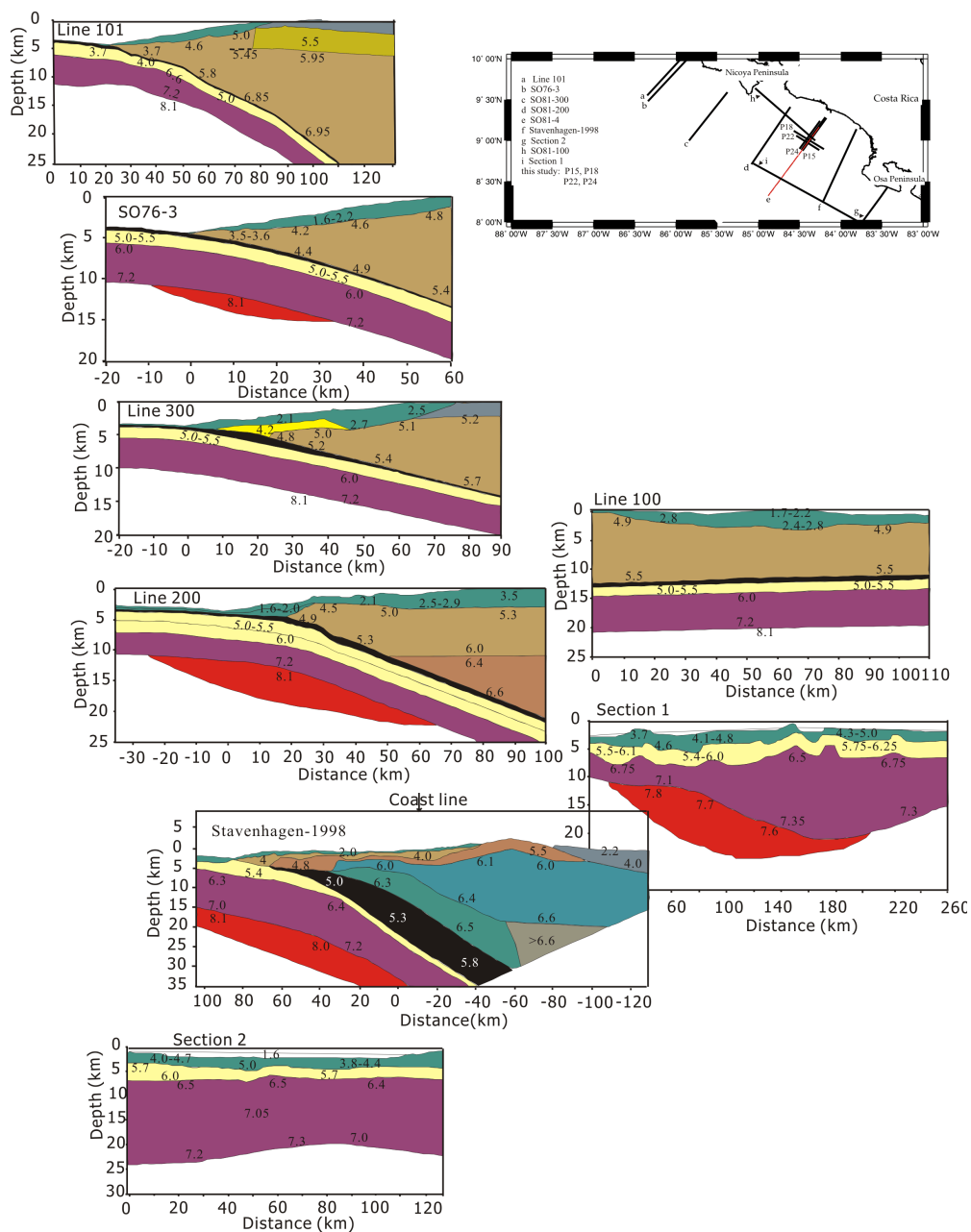


Figure 2.7. Crustal structure obtained from previous acquired wide-angle data. The model

data are extracted from published results (Ye et al., 1996; Stavenhagen et al., 1998; Christeson et al., 1999; Walther et al., 2003). For detailed locations of the seismic profiles see the upper corner panel. The velocity values are marked by numbers. The different colors just show the different structural units. The scale is not identical. The black color zone shows the low velocity zone between the upper plate and the lower plate.

the oceanic crust varies from 5-6 km in the northwest to 9-14 km in the southeast. The variation of ages of the oceanic crust is gained from seafloor magnetic anomalies (Barckhausen et al., 2001) (23-24 Ma at Line 101 and SO76-3, 22 Ma at Line 300 and 15-18 Ma at Line 100, Line 200, Stavenhagen-1998, section 1 and section 2 and this study) (Fig. 2.7). Most profiles show an upper mantle velocity of 8.0-8.1 km/s, however, a reduced upper mantle velocity of 7.6-7.8 km/s occurs beneath Quepos plateau and the outer flank of the Cocos Ridge (section 1, Fig. 2.7). These portions were interpreted as remnants of mafic material in the upper mantle or a plume signature (Walther, 2003). A very interesting characteristic of these models is a low velocity zone (LVZ) sandwiched between the upper Caribbean plate and the lower Cocos plate, which however is quite intricate to constrain from the wide-angle data. The thickness and seismic velocities of this LVZ show some variations: the thickness ranges from several hundred meters to several kilometers and the velocity from 3.0 km/s to 5.8 km/s (Fig. 2.7). The LVZ has been proposed to represent the subduction channel (Cloos and Shreve, 1988a, b). Trench sediments are the main component of subducted material and are clearly observed beneath the décollement (Hinz et al., 1996).

2.2.2 Subduction erosion and accretion

Marine observations of the past decade have advanced the understanding for the mechanics of convergent margins. This is fundamental to assess risks from earthquakes and other geological disasters e.g. oceanic sliding and tsunamis. Scholl et al. (1980) suggested that there are four different basic types of tectonic processes that may act on the sediments and rocks at subduction zones: subduction accretion, sediment subduction, subduction erosion and subduction kneading. Some observations support the notion that erosion and accretion can be coeval, for instance, subducted seamounts erode the upper plate as adjacent sediments accrete (Le Pichon and Henry, 1992; Lallemand et al., 1994; Kukowski et al., 1994; Gutscher et al., 1994; Collot et al., 2008; von Huene et al., 2009). The different features of the two types of active margins (accretionary and erosive) are outlined in schematic cartoons by Clift and Vannucchi (2004). Accretionary margins are characterized by forearc regions com-

posed of thrust and deformed trench and oceanic sediments that often develop mud diapirism and volcanism. In contrast, erosive margins are marked by steep trench slopes, composed of volcanic, plutonic and mantle rocks. Normal faulting is commonly observed cutting through the top of the crystalline basement and eroded material occupies the décollement zone between the upper plate and lower plate (Fig. 2.8). However, subduction erosion mechanisms are still not fully understood, but mainly inferred from seismic observations. One of the problems in direct observation is that erosion along the plate interface commonly occurs beyond the depths at which out-crop scale structures are resolved in seismic records, or penetrated by scientific drilling (von Huene et al., 2004).

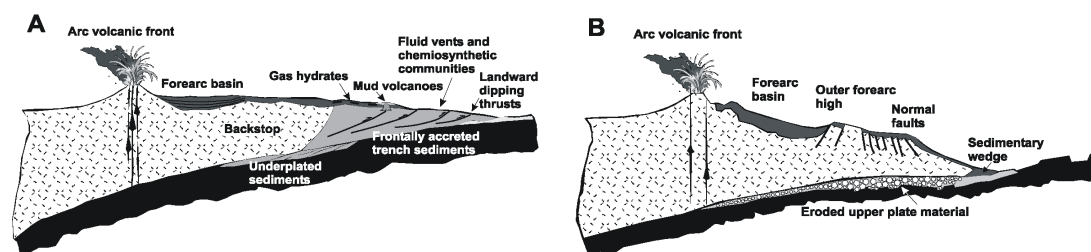


Figure 2.8. Schematic cartoons displaying the two basic types of active margins: (a) accretionary and (b) erosive (from Clift and Vannucchi, 2004).

It is important to recognize that for Costa Rica the accretionary and non-accretionary/erosive concepts are based on the interpretations of seismic reflection and refraction information and the subsidence pattern of the margin. The concept of subduction erosion was clearly defined by von Huene and Scholl (1991). Subduction erosion, a form of tectonic erosion, describes the subduction-caused break up, wearing away, and removal of the rock and sedimentary bodies of an ocean margin. Two types of subduction erosion were proposed by von Huene and Lallemand (1990), frontal and basal subduction erosion. Processes of frontal erosion loosen and remove rock and sediment masses located at the front or toe of the landward trench slope. Processes of basal erosion subcrustally remove the underside of the upper plate, in particular the margin's rock framework (von Huene and Scholl, 1991).

Hilde (1983) proposed that the bending-induced graben structures of subducting plates are a major factor for sediment subduction and tectonic erosion. Horsts act as strong teeth that rasp material from the underside of the upper plate

(Hilde, 1983). This “chainsaw” model can not be applied to explain the upper plate erosion due to volumetric mismatch (Flueh et al., 1999). Recently, a hydrofracturing mechanism by overpressured fluids (von Huene et al., 2004) is proposed to explain the erosion-related events, e.g. subsidence of the margin (Vanucchi et al., 2003, 2004; von Huene et al., 2004). This generic erosion model has integrated all previous geophysical observations and shapes the basic erosive margin (Fig 2.9). Three observations are central to this model: (1) erosion along the underside of the upper plate to explain subsidence, (2) a frontal prism that reduces friction and allows subduction of all trench sediment, and (3) a middle slope progressively deformed by normal faults until it breaks down at the frontal prism (von Huene et al., 2004). Erosion modeled in sandbox experiments (Lallemand et al., 1994) appears to require high basal friction (Adam and Reuther, 2000). Clearly, ridge collision events have been key in controlling long-term (>10 m.y.) tectonic erosion rates (Clift and Vannucchi, 2004). From seismic images of SO81 Line 4 two mechanisms of basal erosion were identified: One is erosion by seamount tunnelling and another is removal of large rock masses of a distending upper plate (Ranero and von Huene, 2000). Ranero et al., [2008] further proposed that tectonic erosion is closely linked to the presence of overpressured fluids migrating through the upper plate.

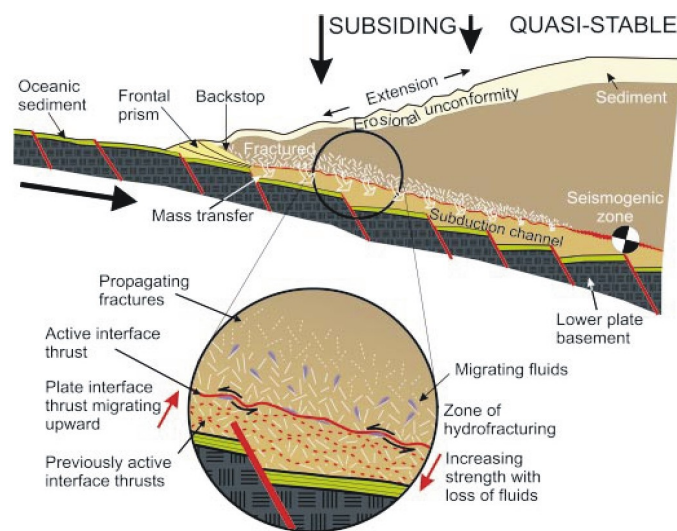


Figure 2.9. Generic model of subduction erosion (from von Huene et al., 2004).

2.2.3 Fluids and seeps at the continental slope

Fluid flow of mainly pore water at the frontal ~1.5 km of the lower slope has previously been recognized from drilling results (Kimura et al., 1997; Silver et al.,

2000). Subducted sediment contains both pore water and chemically bound water. Most pore water is released by compaction during initial subduction. Underthrust sediment beneath the frontal prism is under-consolidated and porosities are reduced to 5-10% about 10-20 km landward of the trench (Kimura et al., 1997). Along the plate boundary fluids play an important role to facilitate basal erosion of the upper plate (Le Pichon et al., 1993; von Huene and Ranero, 2003; Sallarès et al., 2005; Ranero et al., 2008). Initial sediment dewatering processes involve pore water squeezed from the subducted sediment at temperature domains of $< 60^{\circ}\text{C}$ (Fig. 2.10). At greater depth and increased temperatures of $50^{\circ}\text{C} - 160^{\circ}\text{C}$, mineral dehydration reactions pose the dominant process generating fluids at the plate boundary (e.g. Moore and Vrolijk, 1992; Hensen et al., 2004). As suggested by Ranero et al., 2008, plate boundary fluids will migrate upward through the fractured upper plate where they are detected at seeps. Geochemical evidence from Cl-depleted fluid samples of Mound 11 (see Fig.4.4 for location) and other seeps along the Costa Rica margin (Hensen et al., 2004) as well as the inverse amplitude polarity of the plate boundary reflections (Ranero et al., 2008) suggest a deep origin of the fluids (Fig. 2.10). Most seeps including mounds occur near or at faults/fractures reaching the seafloor, which indicates a causal link. The faults penetrate deep into the slope sediment and some extend into the basement (Ranero and von Huene, 2000; Hensen et al., 2004) providing a channel for fluid percolation from deep sources across the igneous basement rock. Most water beneath the deformation front or frontal prism may come from sediment compaction due to the temperature lower than 60°C at the plate boundary, and pore water expulsion occurs at the toe of the margin wedge.

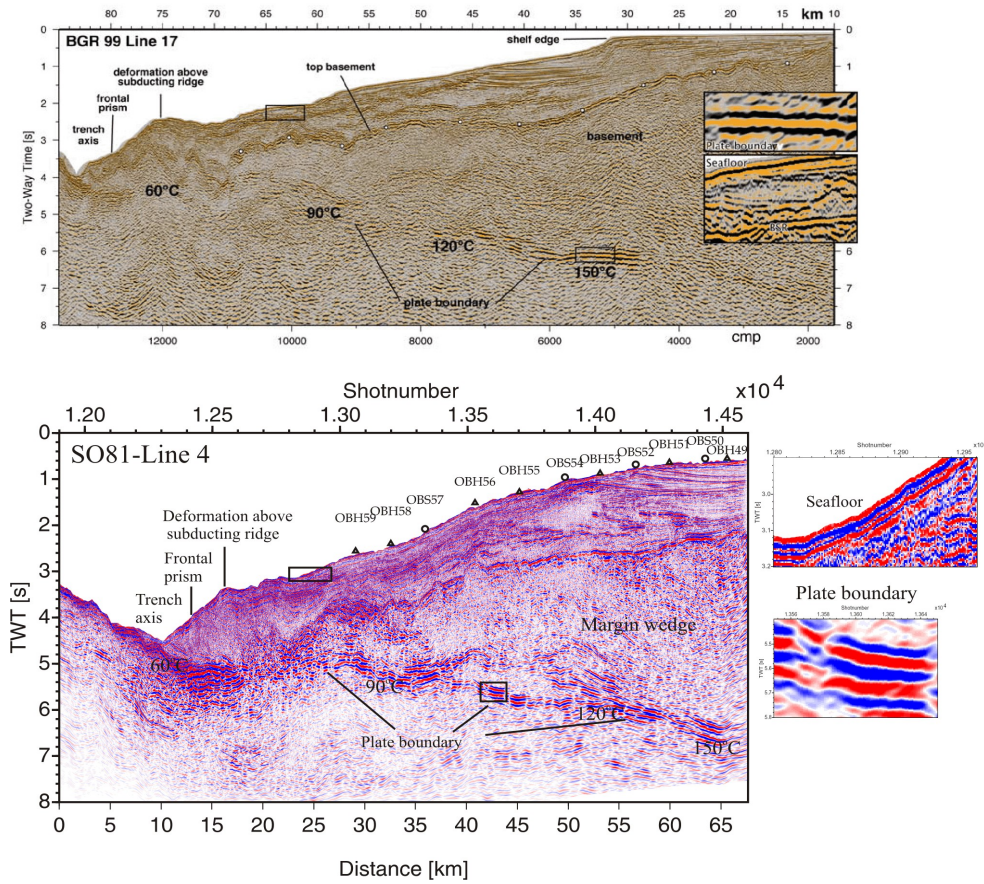


Figure 2.10. Seismic images show clear and strong plate-boundary reflections. Insets show the negative polarity of the plate boundary reflection compared to the positive polarity of the seafloor. The BGR Line 17 (from Ranero et al., (2008)) show a negative polarity patterns (orange-black-orange), as does SO81-Line 4 (blue-red-blue) of the plate boundary reflection. The negative polarity indicates free fluids at the plate boundary. The plate boundary temperature is projected above the seismic lines from ~60 °C to ~150 °C.

Chapter 3

Methods

3.1. Forward modelling method

To reveal the detailed crust and upper mantle velocity structure, the wide-angle data are at first analyzed using forward modelling techniques. First arrivals and secondary arrivals are picked and subsequently calculated and modeled using the 2-D seismic ray-tracing tool “MacRay” (Luetgert, 1992).

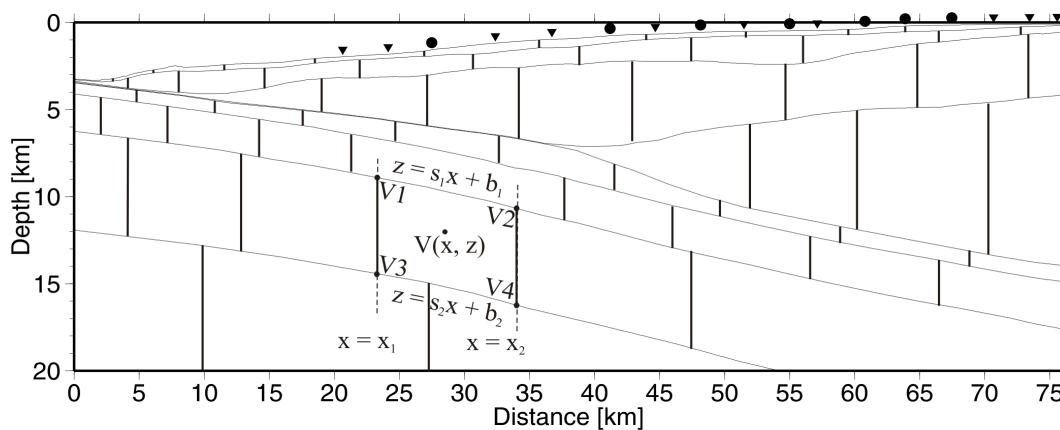


Figure 3.1. Schematic diagram of 2D ray tracing. Vertical bold lines represent the velocity net. Velocities are defined at the intersections of these lines and interfaces.

“MacRay” is an interactive application for calculating travel-time curves from two-dimensional velocity models with the ability to quickly manipulate velocity models and display the resulting travel-times (Luetgert, 1992). Velocity models are defined by two or more interfaces extending across the model from left to right. Interfaces may “pinch out” but may not cross. Any pair of successive interfaces describes a layer, within which the velocity may be defined in terms of the velocity at the top and the bottom of the layer (Fig. 3.1). Within any layer the velocity may be inhomogeneous, but continuous. The lithologic interfaces are represented in the models as first or second order velocity discontinuities. When an interface is encountered in the calculation of a ray, Snell’s law is applied and the calculation is

continued.

The ray tracing algorithm calculates the propagation of rays within a layer by the stepwise integration of the system of first order differential equations (*Cerveny et al.*, 1977)

$$\begin{aligned} \frac{d}{dt}x(t) &= V(x, z)\text{Sin}\theta \\ \frac{d}{dt}z(t) &= V(x, z)\text{Cos}\theta \\ \frac{d}{dt}\theta(t) &= \frac{dv}{dx}\text{Cos}\theta - \frac{dv}{dz}\text{Sin}\theta \end{aligned}$$

where θ is the ray's angle from the vertical. By supplying a definition $V(x, z)$ and initial values for x, z, t , and θ , subsequent values of x, z, t , and θ may be calculated by simultaneously integrating the above three equations over small steps in time. For the derivation and details see *Cerveny et al.*, (1977, p.12).

At any point in the model (Fig. 3.1) the velocity and velocity gradient are defined by bilinear interpolation from the nearest four velocity definition points (*Luetgert*, 1992). The trapezoid model (*Zelt and Smith*, 1992) which has four boundaries in the x - z plane defined by

$x = x_1, x = x_2, z = s_1 + b_1, z = s_2 + b_2$. The P-wave velocity, v , within the trapezoid is defined by:

$$v(x, z) = \frac{(c_1x + c_1x^2 + c_3z + c_4xz + c_5)}{(c_6x + c_7)},$$

where the coefficients, c_i , are linear combinations of the corner velocities,

$$c_1 = s_2(x_2v_1 - x_1v_2) + b_2(v_2 - v_1) - s_1(x_2v_3 - x_1v_4) - b_1(v_4 - v_3),$$

$$c_2 = s_2(v_2 - v_1) - s_1(v_4 - v_3),$$

$$c_3 = x_1v_2 - x_2v_1 + x_2v_3 - x_1v_4,$$

$$c_4 = v_1 - v_2 + v_4 - v_3,$$

$$c_5 = b_2(x_2v_1 - x_1v_2) - b_1(x_2v_3 - x_1v_4),$$

$$c_6 = (s_2 - s_1)(x_2 - x_1),$$

$$c_7 = (b_2 - b_1)(x_2 - x_1).$$

3.2. Travel Time Tomography Method

In this study, I applied the joint refraction and reflection seismic tomography method (TOMO2D code by *Korenaga et al.*, 2000) to invert the wide-angle data. The TOMO2D code allows for forward traveltimes calculation and inversion and offers algorithms for synthetic resolution tests.

3.2.1 Forward traveltimes calculation

The TOMO2D code (*Korenaga et al.*, 2000) uses a hybrid ray-tracing scheme based on the graph method (shortest path method) (*Moser*, 1991) and the ray-bending method, similar to the one developed by *Papazachos and Nolet* (1997) and *Van Avendonk et al.*, (1998). This hybrid method provides an accurate and efficient calculation of travel times and ray paths in terms of both memory and computation time.

The physical significance of the results follows from a combination of Huygen's principle and Fermat's principle. The paths are shortest in traveltimes between the source and the interfaces and between the interfaces and the receiver, and the points on the interfaces connecting the shortest path segments act as secondary sources, provided they are real scatters (*Moser*, 1991). One drawback of the graph method is that representation of a ray path is restricted by a forward star, which defines the structure of possible model connections (*Van Avendonk*, 1998; *Zhang and Toksoez*, 1998). To overcome overestimation of travel times and problems resulting from seismic rays zigzag in the graph solution, *Korenaga et al.*, (2000) incorporated the ray-bending method (*Um and Thurber*, 1987; *Moser et al.*, 1992) to refine the graph solution by using a high-order forward star and a finer mesh to improve the accuracy. The ray-bending procedure employs the conjugate gradient method to directly minimize the travel time along a ray path. Rays are parameterized as beta splines, which can express a variety of curves with a small number of control points, thereby enhancing the convergence in a conjugate gradient search. A constrained conjugate gradient search is used to handle interfaces such as seafloor or a reflector (*Moser et al.*, 1992). A graph solution serves as a good initial guess, which is required for the ray-bending refinement to converge to the global minimum (Fig 3.2). On the basis of bench mark tests, the hybrid approach appears to be more compact both in memory and computation time for typical experimental configurations employed in crustal seismology (*Korenaga et al.*, 2000).

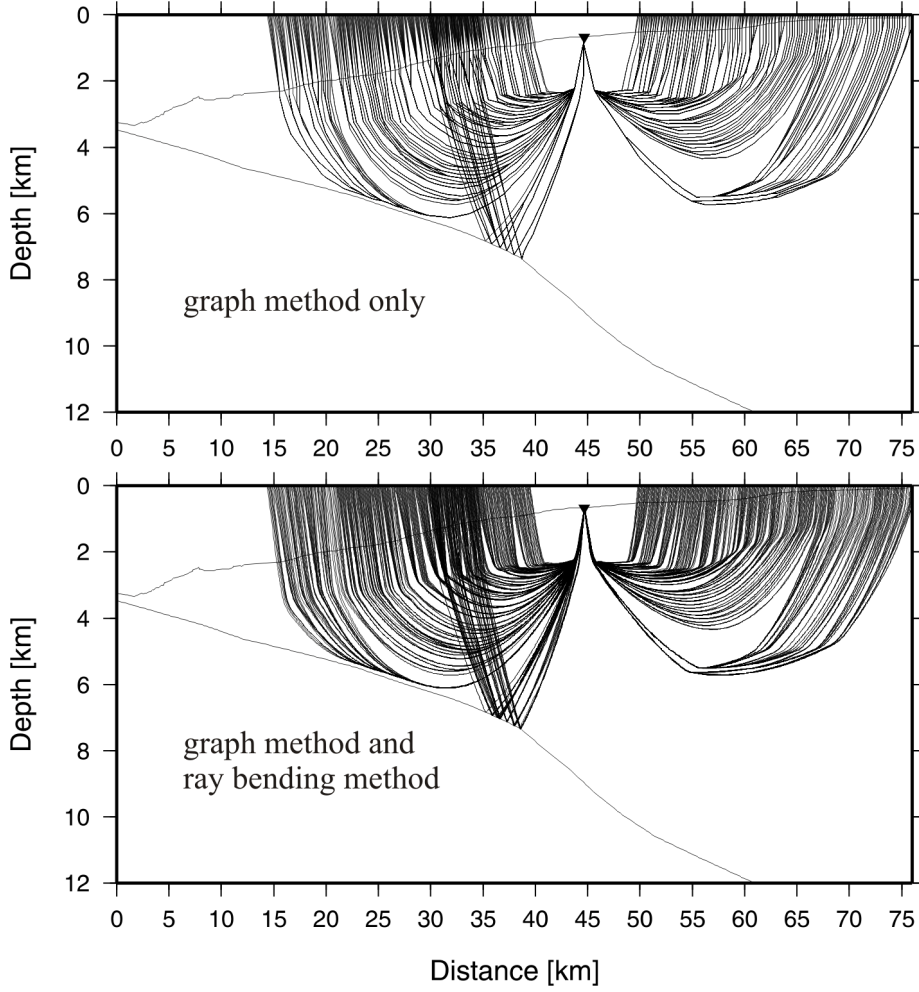


Figure 3.2 Rays calculated with the graph method and hybrid method (graph and ray bending method), respectively. The background velocity model is from profile 15.

3.2.2 Traveltime inversion

In the inverse step, the linear system of equations is solved by using the matrix solver LSQR (*Paige and Saunders, 1982*). Given an initial reference velocity model, refraction travel time residuals δT_j can be mapped into slowness perturbations δu along the ray paths Γ_j in a reference model, using the following integral:

$$\delta T_j = \int_{\Gamma_j} \delta u d\Gamma .$$

Similarly, reflection travel time residuals can be written in 2-D Cartesian coordinates as

$$\delta T_j = \int_{\Gamma_j} \delta u d\Gamma + \left. \frac{\partial T}{\partial z} \right|_{x=x_j} \delta z(x_j),$$

where x_j is the reflecting point of the j th ray. Using finite dimensional approximation of velocity and reflector models, the above residual equations can be discretized and written collectively as a matrix equation

$$d = G\delta m,$$

where d is the travel time residual vector, G is the Fréchet derivative matrix, and δm is the unknown model perturbation vector. When a starting model is far from the true model, the above linearized inversion must be applied iteratively until the model converges. The velocity sensitivity part of the Fréchet matrix is a path length distributed to relevant velocity nodes according to the bilinear interpolation used for slowness interpolation. The depth sensitivity part can be expressed using an incident angle upon reflection, the slope of a reference reflector, and the velocity at the reflecting point as derived by Bishop et al., (1985). The normalization of model parameters is beneficial to minimize a possible solution bias due to the magnitude of reference model parameters (Toomey et al., 1994). Thus the matrix equation is normalized through the following relations:

$$G' = C_d^{-1}GC_m^{-1/2},$$

$$\delta m' = C_m^{-1/2}\delta m,$$

$$d' = C_d^{-1/2}d,$$

where the model scaling matrix C_m is a diagonal matrix whose elements are each a square of a model parameters. To restrict the model space to the reasonable way, Korenaga et al., (2000) applied smoothness constraints on both velocity and depth perturbations using predefined correlation lengths by using 1-D smoothing constraints for horizontal and vertical directions (e.g. Toomey et al., 1994). A regularized linear system can be written as

$$\begin{bmatrix} d \\ 0 \\ 0 \\ 0 \end{bmatrix} = \begin{bmatrix} G_v & wG_d \\ \lambda_v L_{Hv} & 0 \\ \lambda_v L_{Vv} & 0 \\ 0 & w\lambda_d L_d \end{bmatrix} \begin{bmatrix} \delta m_v \\ \frac{1}{w}\delta m_d \end{bmatrix}$$

where subscripts v and d for the Fréchet matrix and the model vector denote their velocity and depth components, respectively. λ_v and λ_d control the relative importance of the smoothing constraints. L_{Hv} and L_{Vv} are the horizontal and vertical smoothing matrices for slowness perturbations. L_d is the smoothing matrix for depth perturbations. The depth kernel weighting parameter, w , adjusts the relative weighting of depth sensitivity in the matrix. When a starting model is far from a true solution, the model update may be too large and cause unstable succeeding iterations, requiring

the addition of damping constraints for velocity and depth nodes to regularized equation above. Increasing the weighting parameter (w) should lead to larger depth perturbations with smaller velocity perturbations if the system is singular. Generally this parameter is applied to test velocity-depth ambiguity with the single controlling parameter. The inversion strategy used is an iterative 'jumping' (Shaw and Orcutt, 1985) which selects the smoothest model that provides a satisfactory fit to the data. The ray coverage in the model can be concisely represented by the derivative weight sum (DWS)(Toomey and Foulger, 1989), which is the column-sum vector of the Fréchet velocity kernel. The DWS can be regarded as a crude measure of the linear sensitivity for a velocity model in the inversion (Korenaga et al., 2000).

Chapter 4

Crustal structure of the central Costa Rica subduction zone: implications for basal erosion from seismic wide-angle data

4.1. Introduction

Convergent margins are dynamic plate boundaries characterized geomorphically by deep ocean trenches, seismically by landward dipping zones of earthquakes, tectonically by regional-scale crustal faulting and terrane movements, and magmatically by arcuate and linear belts of eruptive centers- the volcanic arc (von Huene and Scholl, 1991). Convergent margins appear to fall into one of two classes, accretionary and non-accretionary/erosive (Clift and Vannucchi, 2004). Subduction erosion at present dominates the Middle America convergent margin (Meschede et al., 1999a; 1999b; Ranero and von Huene, 2000; Vannucchi, et al., 2001; 2003) where the frontal prism or outer wedge structure (Wang and Hu, 2006) is limited to approximately 15 km adjacent to the trench axis (von Huene and Flueh, 1994; Hinz et al., 1996). The process of subduction erosion is defined as the mass removal and transport of upper plate material toward subcrustal and mantle depth resulting in extension and subsidence of the forearc (Vannucchi et al., 2001; 2003). The recovery of shallow water sediment at Site 1042 (Fig. 4.1) documents margin-wide subsidence off Costa Rica during the past 16-17 Myr (Vannucchi et al., 2001). The short-term rate of removal of rock from the forearc in Central America was calculated to be about 107-123 km³Myr⁻¹km⁻¹ (Vannucchi et al., 2003). Subduction of positive morphological features like seamounts, ridges and rises has been reported to facilitate subduction erosion at convergent plate margins (von Huene, 1986; von Huene, et al., 2000; Miura, et al., 2004; Kopp et al., 2006). In addition, hydrofracturing was proposed as a possible mechanism to explain the material removal from the base of the upper plate (Behrmann, 1991; Le Pichon et al., 1993; von Huene and Ranero, 2003). Separated upper plate fragments are subsequently dragged along the plate interface to subcrustal depth (von Huene et al., 2004).

In a previous study, multichannel seismic data (MCS) with 48 channels at a 4-

ms sampling rate were acquired off central Costa Rica (R/V Sonne Cruise SO81 in 1992) (Hinz et al., 1996). On profile SO81 Line 4 (Fig. 4.2), a strong plate-boundary reflection bifurcates 25 km landward of the trench at about 5 s two-way travel time (TWTT). This bifurcation extends laterally for about 15 km, the enclosed unit has been termed a ‘megalsens’ by Flueh et al. [1999] and later also by Ranero and von Huene [2000] (Fig. 4.3). From seismic images of SO81 Line 4 two mechanisms of basal erosion were identified: One is erosion by seamount tunnelling and another is removal of large rock masses of a distending upper plate (Ranero and von Huene, 2000). Sage et al., [2006] proposed fluid-rich trench sediment rapidly being underthrust along the Ecuadorian margin. The thin subduction channel here locally forms thickened lenses of sedimentary material resulting in interplate coupling variations (Tsuru et al., 2002; Sage et al., 2006). Ranero et al., [2008] proposed that tectonic erosion is closely linked to the presence of overpressured fluids migrating through the upper plate.

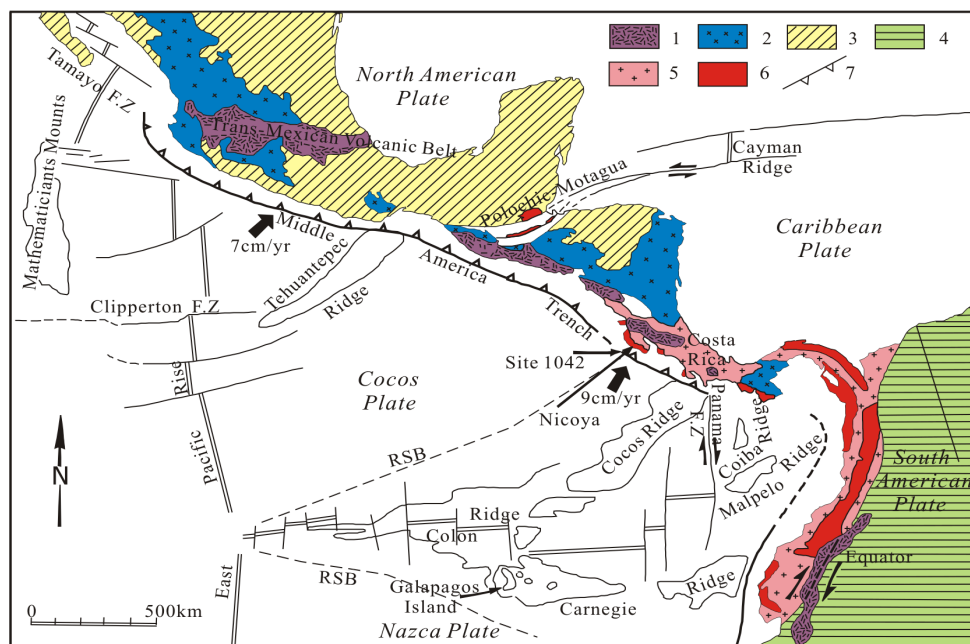


Figure 4.1. Tectonic setting of the Central America convergent margin (after Azéma et al [1985]). 1, Pliocene and Pleistocene volcanism; 2, Oligocene and Miocene volcanism; 3, North America plate; 4, South America plate; 5, Cenozoic formations of ophiolitic Andes and southern Central America; 6, Mesozoic and Cenozoic ophiolitic complex; 7, Subduction zone. RSB = rough –smooth boundary.

In this study we use refraction seismic data acquired during cruise SO163 of the German R/V Sonne in 2002 (Weinrebe and Flueh, 2002) to derive a detailed velocity-depth model along the continental slope of central Costa Rica. The newly acquired data resolve the velocity structure of the ‘megalens’. Our results imply a mixture composition of the ‘megalens’ consisting of subducted sediment and dismembered upper plate material in a fluid-rich environment.

4.2. Geodynamic setting

The Farallon plate broke up into the Cocos plate and the Nazca plate along a pre-existing fracture zone about 25 Ma (Fig. 4.1). The Cocos Ridge and the Carnegie Ridge are interpreted as hotspot tracks formed at the Galapagos hot spot (Hey, 1977). The Cocos plate is bordered by the East Pacific Rise, the Galapagos rift zone, the north-trending Panama fracture zone near 82°W, and the Middle America arc. The Middle America trench (MAT) is a convergent plate boundary that marks the subduction of the Cocos plate beneath Central America and Mexico with varying convergence rates (Fig. 4.1). An estimate for the Cocos-Caribbean convergence rate is 84 ± 5 mm/yr, accompanied by a dextral, trench-parallel slip rate of 14 ± 2 mm/yr at 88-85.5°W (DeMets, 2001; DeMets et al, 1990; 1994). The variable morphology of the Cocos plate off Costa Rica has been recognized from high resolution multibeam swath mapping (Fig. 4.2). Three morphotectonic domains were defined by von Huene et al., [1995; 2000]. Fisher Ridge marks the boundary between the smooth segment off Nicoya Peninsula and the seamount segment to the south (Fig. 4.2). The Cocos Ridge segment off Osa Peninsula is a broad shallow domain to the south. The segmentation is implied to have an influence on the forearc structure and the seismogenesis of the subduction zone. The Quepos plateau is dated 14 m.y. and the oldest part of Cocos Ridge near the MAT is 13-15 m.y. (Werner et al., 1999; Barckhausen et al, 2001). The isodepth contours of the Wadati-Benioff zone between the Nicoya Peninsula and Osa Peninsula is about 40 km and the dip angle of the Wadati-Benioff zone decreases from 84° under Nicaragua to 60° under central Costa Rica (Protti et al., 1995). Bending-related earthquakes along the MAT occur in the northwest of Costa Rica and no bend-faulting occurs in the vicinity of the thick-crust Cocos Ridge (Ranero et al., 2005).

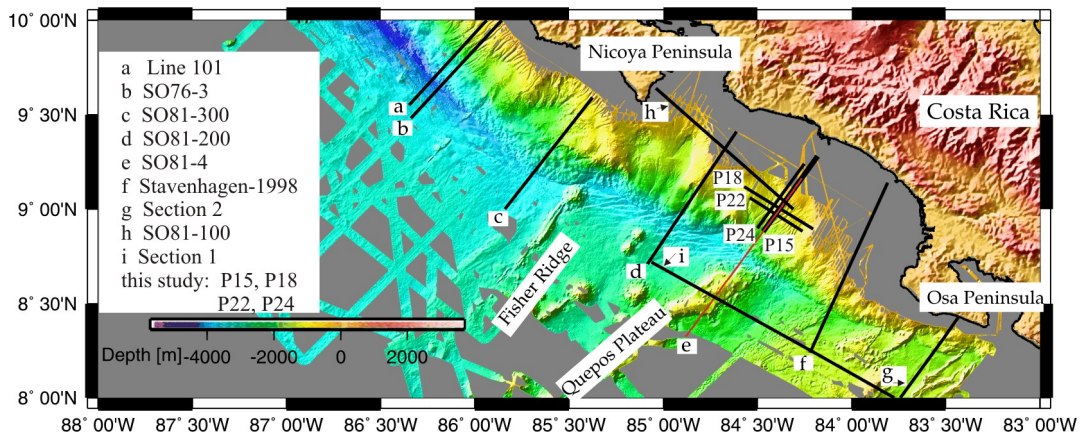


Figure 4.2. Location map of seismic wide-angle profiles offshore of Costa Rica with seafloor bathymetry illuminated from the NE. The positions of wide-angle profiles SO76-3, SO81-100, SO81-200 and SO81-300 are from Ye et al., (1996). Section 1 and section 2 are after Walther, (2003). Line 101 is after Christeson et al., (1999). Stavenhagen-1998 line is after Stavenhagen et al., (1998). P15, P18, P22 and P24 profiles are from this study. SO81-4 (red line) used in this study is a MCS line coincident with our wide-angle profile 15.

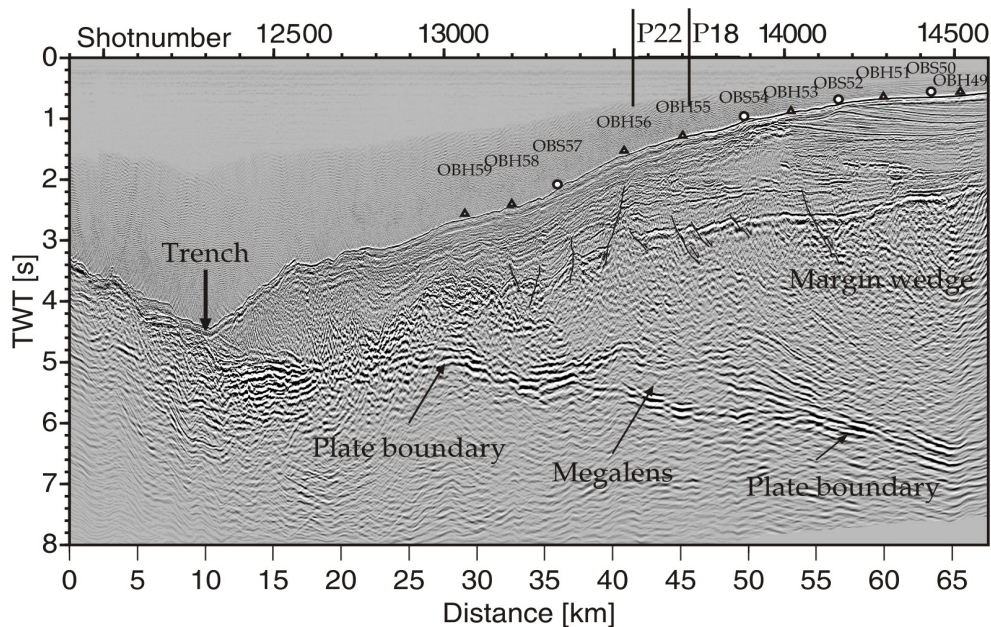


Figure 4.3. Time migrated section of SO81 Line 4. The ‘megalens’ is bounded by strong-amplitude reflections, which bifurcate from the plate boundary. OBH(S) stations along profile

SO163-P15 are superimposed on Line 4. Black triangles mark OBH stations and circles mark OBS stations.

4.3. Wide-angle Experiment

4.3.1 Data Acquisition and Processing

During cruise SO163 in 2002 four profiles were collected, located approximately 25 km northeast of the Quepos plateau (SO163 P15, 18, 22, and 24, in Fig. 4.2). Wide angle profile 15 was shot coincident with the previous multichannel reflection seismic profile SO81 Line 4 (Hinz et al., 1996) (Fig. 4.2). In addition, a parallel wide-angle dip line and two perpendicular wide-angle strike lines were shot. Along the four profiles a total of 42 IFM-GEOMAR ocean bottom hydrophones (OBH) (Flueh and Bialas, 1996) and 22 ocean bottom seismometers (OBS) (Bialas and Flueh, 1999) were deployed. The average instrument spacing is about 2.5 km. The detailed station positions are displayed in Figure 4.4 The sample rate for the instruments was 4 ms or 5 ms. Along each line, shots with two G-Gun clusters with a total volume of 1700 cinch were triggered at 30 s interval at an average speed of 3.5 knots, resulting in an average shotpoint distance of 54 m. Data quality for the majority of instruments is excellent. Wide-angle data processing included relocation of the instrument positions by analysis of the water wave arrivals. Frequency analysis of the data reveals that the signal is focused in a narrow frequency band. The main frequencies of arrivals recorded by OBH stations are between 9 and 16 Hz. A time- and offset- dependent frequency filter was applied to adjust for the time- and offset-dependent variations. Subsequently, a predictive deconvolution was applied to the data to improve the temporal resolution. Only selected record sections are shown here.

4.3.2 Modelling

4.3.2.1 Forward Modelling

To image the structure of the margin and to obtain the P-wave velocity field, especially in the vicinity of the 'megalens', a 2-D forward modelling technique (Luetgert, 1992) using a top-bottom approach was performed for all profiles. First and secondary arrivals were picked for all stations. Phase nomenclature is given in Table 1. The MCS data were used to constrain the upper units of the dip line P15, including the top of margin wedge, the periphery of the 'megalens', and the top of the

downgoing slab (Fig. 4.3). The two strike-lines P18 and P22 were later tied to the dip-lines and thus further constrained the velocity-depth model along the continental slope off central Costa Rica (Fig. 4.5). The vertical velocity gradient within the different layers is constrained by the wide-angle data. However, the velocity gradient within the ‘megalens’ cannot directly be retrieved from the refraction data due to the velocity inversion. Therefore different velocity gradients were tested during the forward modelling until an optimal fit of phases from the ‘megalens’ and the upper oceanic crust was achieved.

Table 4.1. Phase nomenclature for wide-angle arrivals

Phase	Description
Ps	sedimentary phases
Pumw	refraction through the upper margin wedge
Plmw	refraction through the lower margin wedge
PtP	reflection from the top of the ‘megalens’
PbP	reflection from the bottom of the ‘megalens’
PtlmP	reflection from the top of the lower margin wedge
Puoc	refraction through upper oceanic crust
PiP	reflection from the top of lower oceanic crust
Ploc	refraction through lower oceanic crust
PmP	reflection from crust-mantle boundary
Pn	refraction through the upper mantle

4.3.2.2 Amplitude Modelling

The forward raytracing modelling technique is limited to the use of travel times and does not utilize the seismic amplitude information. Some high amplitude events identified in the data were modeled by calculating synthetic seismograms, especially wide-angle reflection phases when their traveltimes were not sensitive enough to sharply define the velocity gradients or the nature of interfaces. The amplitude modelling was performed using the 1D reflectivity code of Sandmeier and Wenzel [1986]. The 1-D velocity-depth model was provided by strike-lines P18 and P22. The modelling procedure is a trial-and-error process in which we propose a model consisting of many plane homogeneous layers, each showing a distinct P wave velocity (V_p), S wave velocity (V_s), density, and P and S attenuation quality factors Q_p and Q_s . Calculated synthetic seismograms were compared with the observed

seismograms, until an optimal fit is realized. For our amplitude modelling, we used a constant Poisson ratio of 0.28 and set $Q_p = 2Q_s$ (as used by Spudich and Orcutt, 1980; Christeson et al., 2000). Q_p was varied during modelling. A Q_p value of 300-500 for the forearc region is in agreement with earlier observations (Bowman, 1988). Densities were set to 1.5 g/cm^3 for the slope sediments and 1.8 g/cm^3 within the margin wedge (Kimura et al., 1997; Christeson et al., 2000). Densities for oceanic crust were calculated using the relationship $\rho = 1.85 + 0.165V_p$ (Christensen et al., 1970; Christeson et al., 2000).

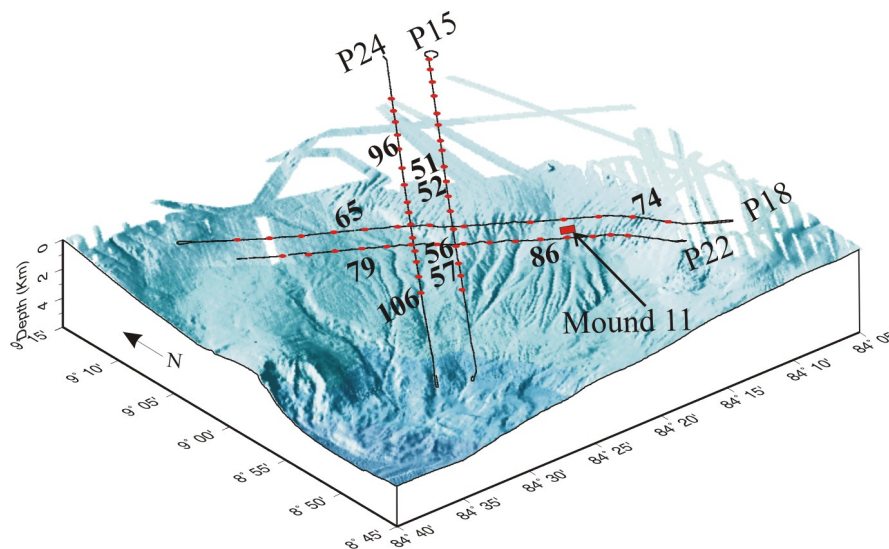


Figure 4.4 Detailed location map of wide-angle profiles in this study. 64 OBH(S) stations were deployed. Record sections from numbered OBH(S) stations are displayed in Figs. 4.6-4.10 and 4.12-4.15. The location of Mound 11 is from Soeding et al., [2003].

4.4. Interpretation

The crustal models of the Central Costa Rica margin along two parallel dip-lines and two parallel strike-lines are presented in Figure 4.5. In the following, models are described individually from top to bottom, and related record sections are shown to demonstrate the fit between observed and modeled arrival times.

4.4.1 Dip-lines SO163-P15 and SO163-P24

4.4.1.1 Sediment

The sediment phase P_s is clearly observed on all record profiles and is modeled as a refraction through the sedimentary layer, which has a variable thickness

of 500-1800 m, with P-wave velocities of 1.6-2.4 km/s. This thickness is constrained by the MCS data (Fig. 4.3) and refraction phase P_{umw} from the upper margin wedge. The thickness of the sediment near the trench increases to 1.5 km (Fig. 4.5) at profile km 10 and displays velocities of 1.8-2.3 km/s. The thickness of the sedimentary cover on the mid-shelf increases to 1.8 km beneath station OBH51 and the velocities reach 2.4 km/s. Towards the coast, sediment thickness decreases to 500 m and the velocities reach a value of 2.1 km/s.

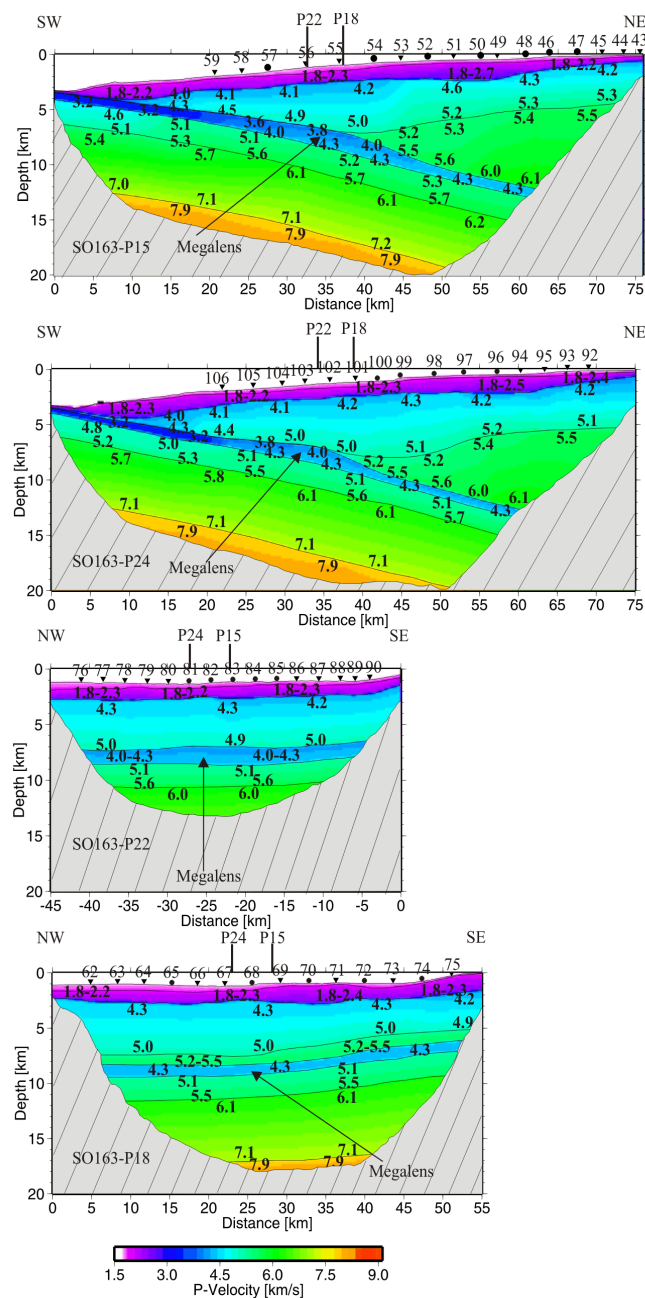


Figure 4.5. Four velocity-depth models along the Pacific margin of central Costa Rica. The

subducted slab and the ‘megalens’ (located updip of the profile intersection) are recorded along the two dip-lines SO163 profile P15, P24 and two strike-lines P18 and P22. The detailed positions of OBH(S) and the P-wave velocities are marked on the profiles.

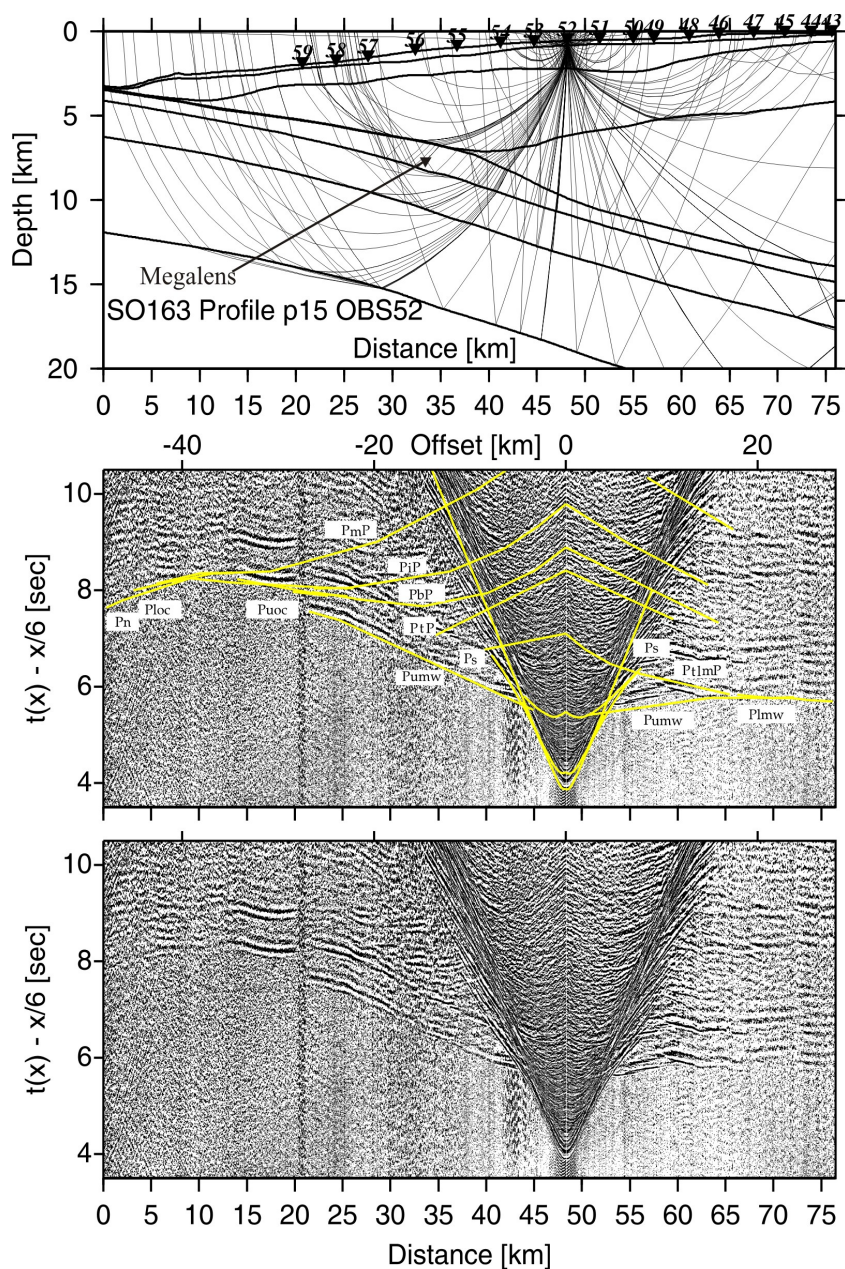


Figure 4.6. Record section from station OBS52 deployed along the dip-line SO163-P15. The uppermost image displays the ray paths through the model subsurface. The data are shown with modeled traveltimes overlain in the upper images and the raw data displayed in the lower section. Refer to Table 1 for nomenclature. Refracted phases Puoc and Ploc and associated near vertical reflections PbP and PiP track the top of the upper oceanic crust and the top of the

lower oceanic crust, respectively.

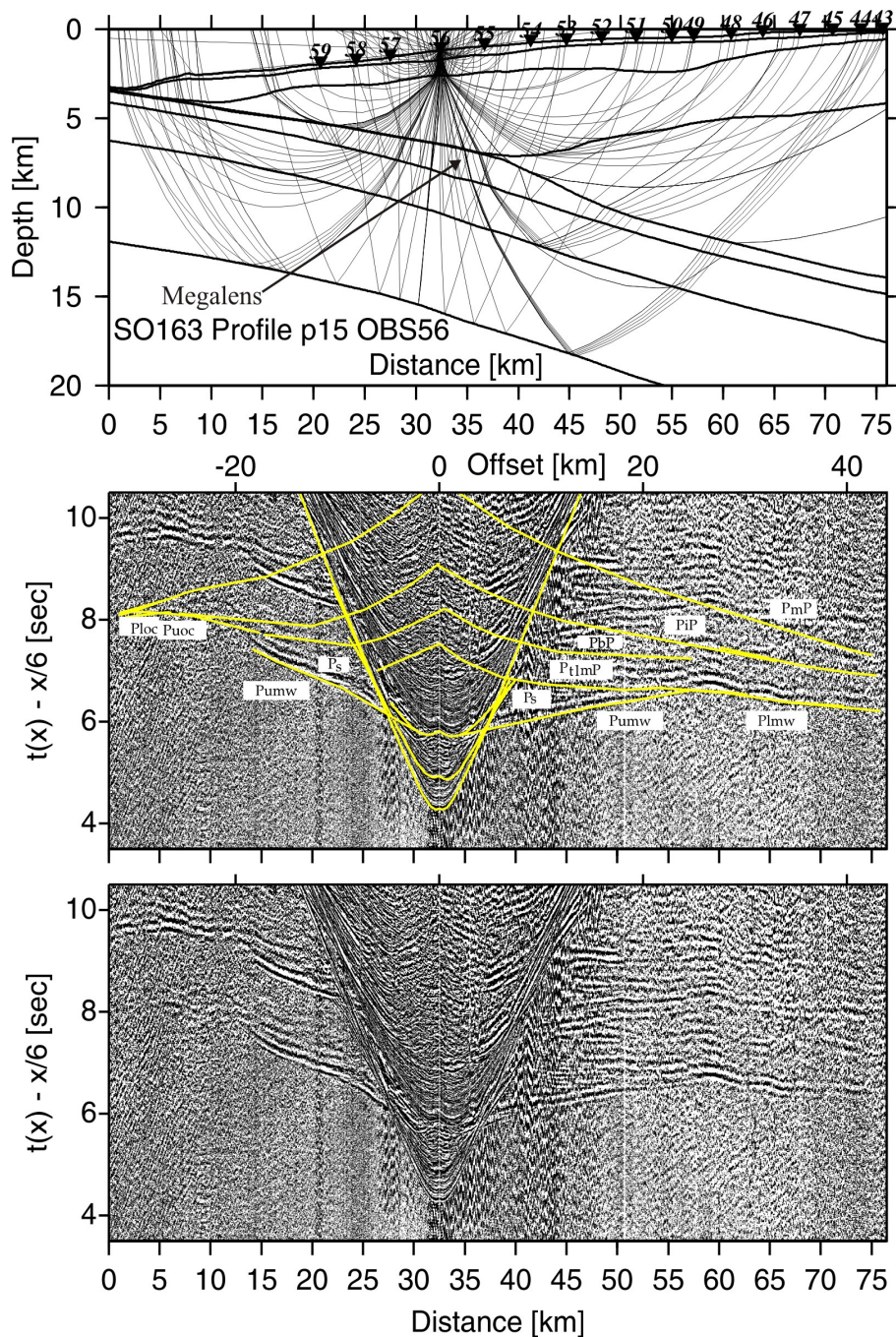


Figure 4.7. Record section and ray diagram for station OBH56 deployed along the dip-line SO163-P15. Please refer to Fig. 4.6 for display information. Phases PtlmP and Plmw track the lower margin wedge. Refraction phase Puoc tracks the upper oceanic crust. The oceanic crust-mantle boundary is tracked by PmP and Pn phase.

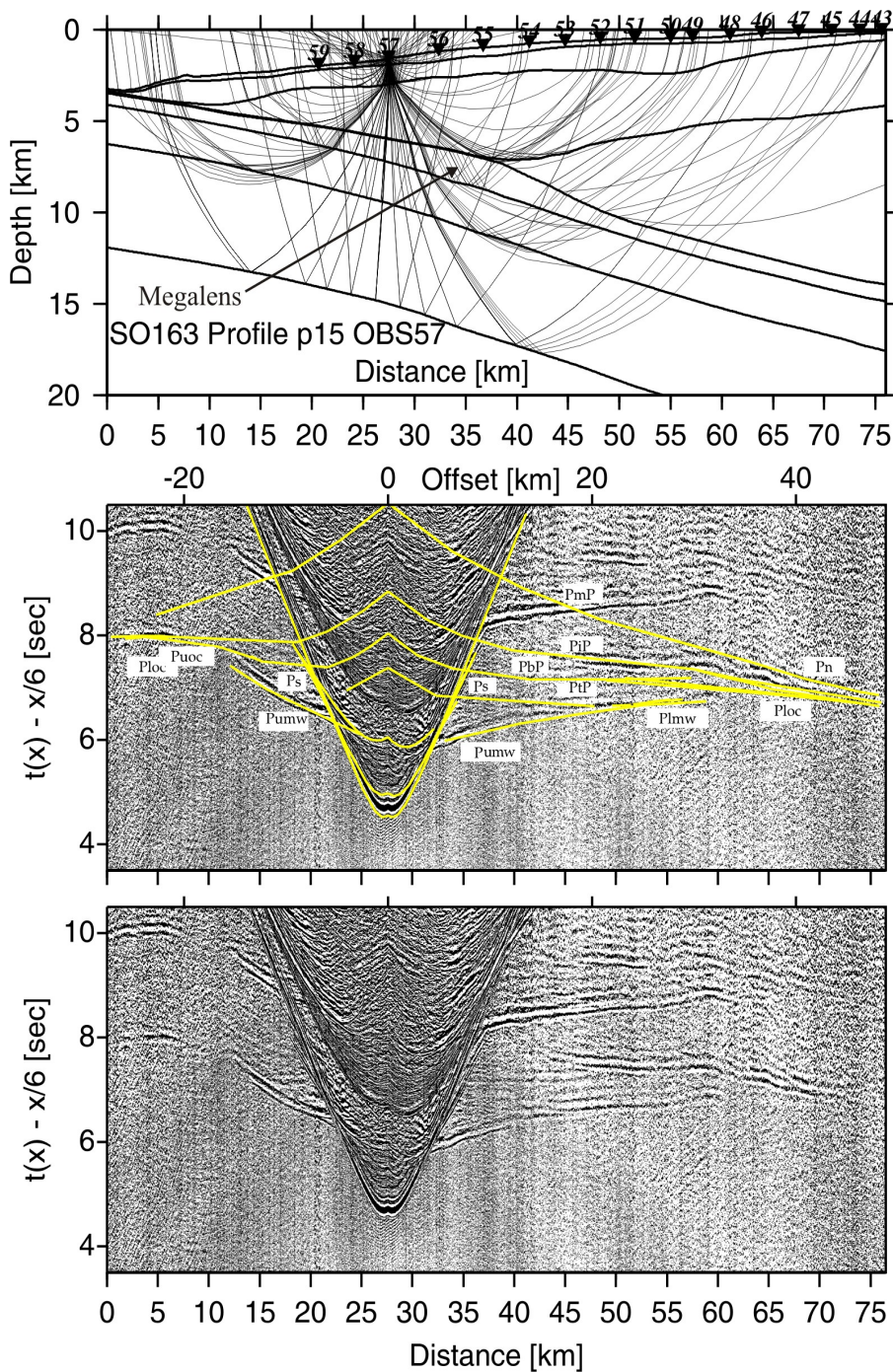


Figure 4.8. Record section and ray diagram for station OBS57 deployed along the dip-line SO163-P15. Please refer to Fig. 4.6 for display information. The oceanic crust-mantle boundary is recorded by phase Pn. Strong phases PiP and Ploc track the lower oceanic crust. The plate boundary is recorded as a pre-critical reflection PbP. Phase Plmw tracks the lower margin wedge and the top of the lower margin wedge is recorded as wide-angle reflection PtlmP.

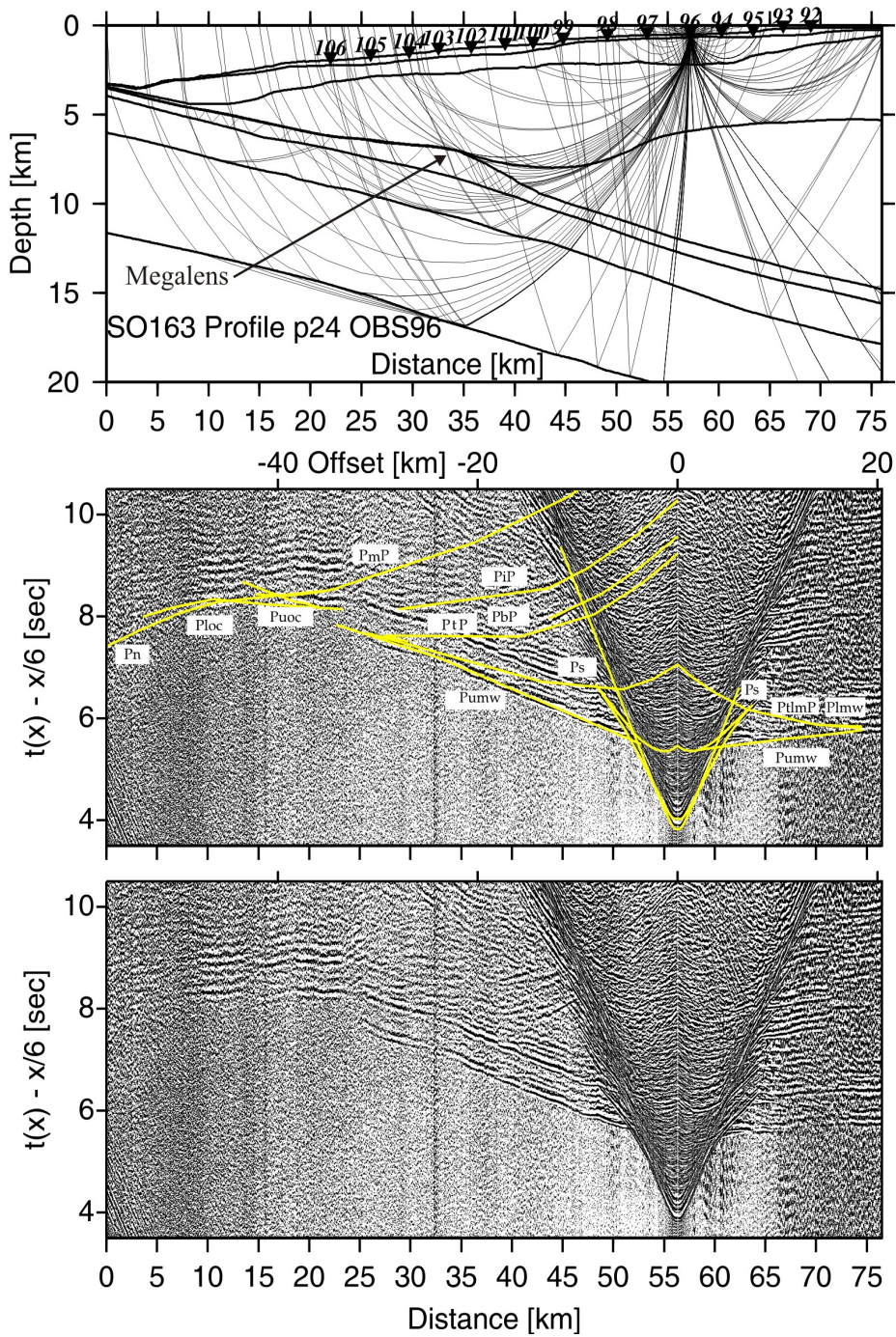


Figure 4.9. Record section and ray diagram for station OBS96 deployed along the dip-line SO163-P24. Please refer to Fig. 4.6 for display information. Phases Puoc and PbP track the downgoing slab. Phase Plmw travels through the lower margin wedge.

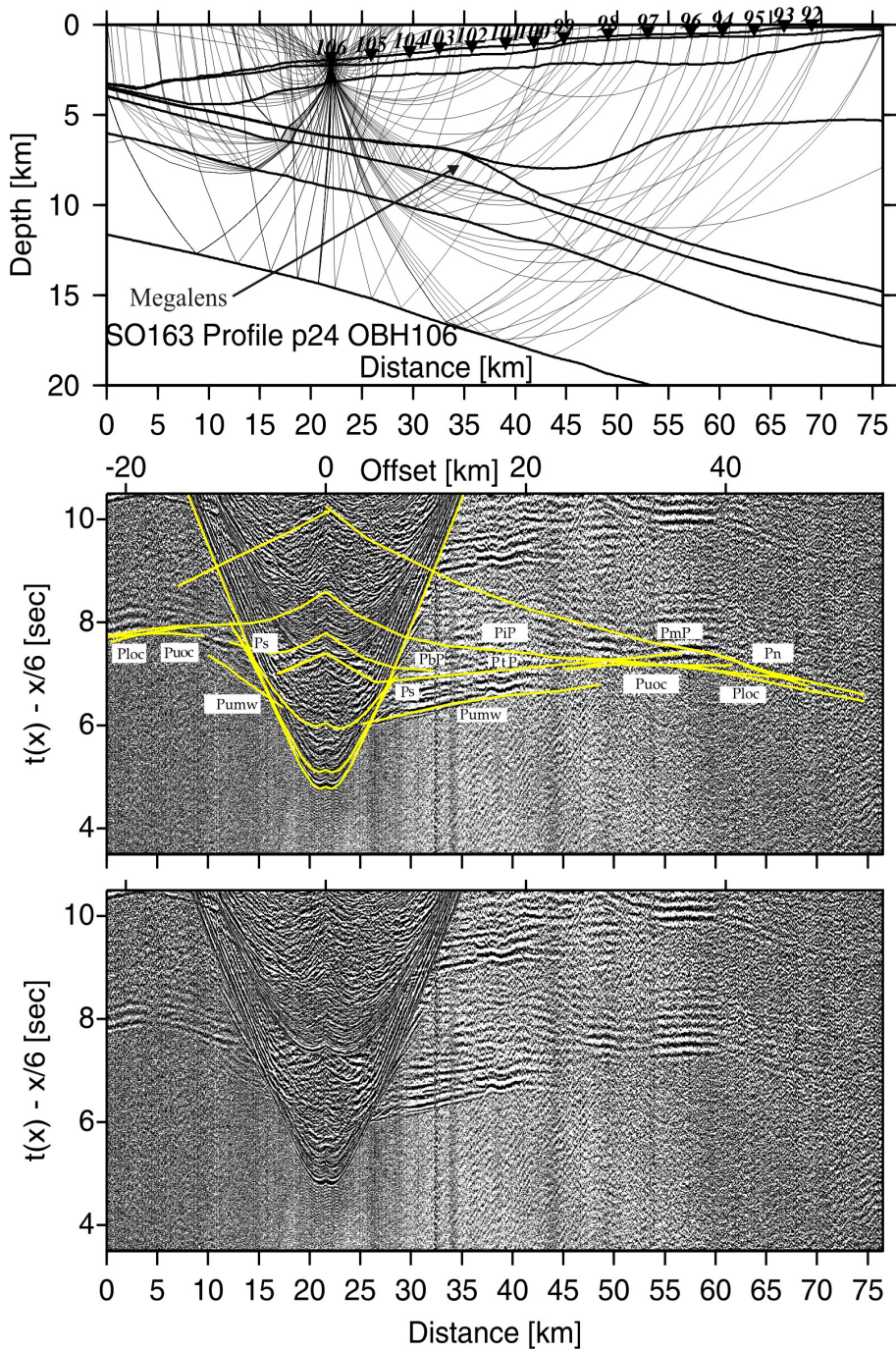


Figure 4.10. Record section and ray diagram for station OBS106 deployed along the dip-line SO163-P24. Please refer to Fig. 4.6 for display information. Phases Puoc and PbP track the downgoing slab. The oceanic crust-mantle boundary is tracked by PmP and Pn phase.

4.4.1.2 Upper and lower margin wedge

The margin wedge is divided into two layers with different velocity gradients. Clear first arrivals observed on all OBH(S) stations are used to constrain the margin wedge (see refraction phases Pumw and Plmw through the margin wedge, Figs. 4.6-10). The P-wave velocity of the upper margin wedge varies from 4.0-4.3 km/s near the trench to 4.0-5.1 km/s close to coastline (dip-line P24, Fig. 4.5). On the parallel dip-line P15 the velocity of the upper margin wedge varies from 4.1-4.5 km/s near the trench to 4.2-5.3 km/s near the coastline. Lateral velocity and thickness variations are observed along the two dip-lines (Fig. 4.5). Vertical velocity gradients are well constrained within the margin wedge by modelling of travel time data because the reflection phase (PtlmP) from the top of the lower margin wedge and the refraction phase (Plmw) through this layer are clearly observed (Figs. 4.6-9). Between stations OBH 105 to OBH 92 the interface between the upper and lower margin wedge is constrained with high confidence from the refraction phase Plmw (Fig. 4.11). The ray coverage through this layer is shown in Figure 4.11 along the dip-line P24. The top and bottom velocity of the lower margin wedge increases with depth from 5.2 km/s to 5.5 km/s and 5.5 km/s to 6.1 km/s, respectively. Near the landward edge of the ‘megalens’, the depth of this interface reaches to about 8 km and a lower margin wedge is not existent further seaward (beneath station OBH102, Fig. 4.11).

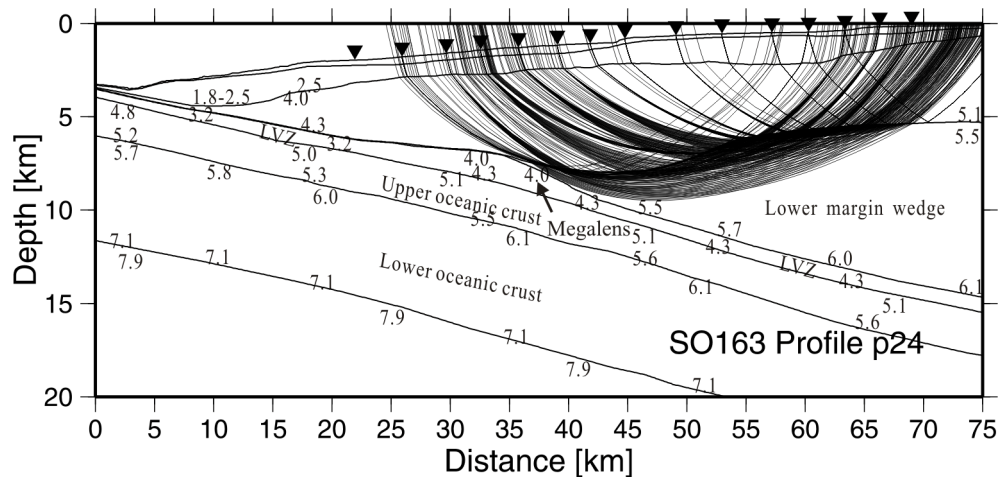


Figure 4.11. Ray coverage of the lower margin wedge displayed for dip-line P24. The top of the lower margin wedge is well constrained by the closely spaced OBH(S) stations in our velocity model.

4.4.1.3 ‘Megalens’ and low velocity zone

The ‘megalens’ is clearly observed in the MCS data (Fig. 4.3). In our starting model the interface and thickness of the ‘megalens’ are preliminarily estimated from the reflection data. We observe the reflection phase PbP at the bottom of the ‘megalens’ and the refracted phase Puoc from the top of the oceanic crust, which are used to indicate the thickness/velocity ambiguity of the ‘megalens’ (Fig. 4.6, profile distance 15-20 km; Fig. 4.7, Fig 4.10, profile distance 3-10 km). The uncertainty analysis will further show this ambiguity (refer to 4.4 Model sensitivity and uncertainty tests). A 1-1.5 km thick lens-shaped feature with velocities of 3.8-4.3 km/s best satisfies reflection arrivals as well as refraction arrivals through the upper oceanic crust.

A low velocity zone overlaying the subducted plate is universally observed along the Costa Rica convergent margin. It was presented in previous wide-angle velocity models varying in thickness and velocity (Ye et al., 1996; Stavenhagen et al., 1998; Christeson et al., 1999). In our data we observe a time delay of the slab refraction phase, which leads us to incorporate a LVZ above the oceanic crust to improve the fit of calculated to observed travel times in our model (see phase Puoc, Fig. 4.6, Fig. 4.7 and Fig. 4.10). Near the trench the thickness of the LVZ is about 400 m and we assume a constant velocity of 3.2 km/s for this layer, which is interpreted as subducted sediment. Beneath the margin wedge the strong plate boundary reflection is shown in the MCS data as well as on some wide-angle records (see phase PbP from these station records, Fig. 4.6 and Fig. 4.8). Negative polarity reflections indicate the presence of the fluids at the plate boundary in Costa Rica (Ranero et al., 2008) and are related to the LVZ.

4.4.1.4 Upper and lower oceanic crust

The subducting oceanic crust is divided into two layers: upper oceanic crust and lower oceanic crust. Due to the complex geometry of the dipping slab and the seafloor morphology, refracted arrivals through the oceanic crust display some travel-time variability along the dip-lines. All arrivals through the upper and lower oceanic crust were observed and modeled. In Figure 4.6 (OBS52) a distinct high amplitude event is observed at profile km 12-20. It is interpreted as a refraction phase Puoc through the upper oceanic crust, which has a high velocity gradient and therefore focuses the energy into a short offset interval. A refraction phase Ploc through the lower oceanic crust was observed on some records (Fig. 4.6, profile distance km 0-10; Fig. 4.8, profile distance km 0-8 and 60-73; Fig. 4.9 and Fig. 4.10). A clear reflection

phase PiP is visible at a distance of 41-60 km (Fig. 4.8), which is interpreted as a reflection from the interface between upper and lower oceanic crust. A short refraction phase Pn through the upper mantle is visible in the record of OBS57 at a distance of 66-73 km (Fig. 4.8) and in the record section of OBS106 (Fig. 4.10) at a distance of 61-68 km. These refracted and reflected phases constrain a 2-2.5 km thick upper oceanic crust with velocities of 5.0-5.5 km/s and a 5.5-6 km thick lower oceanic crust with velocities of 5.8-7.1 km/s (Fig. 4.5).

4.4.2 Strike-lines SO163-P18 and SO163-P22

Strike-lines P18 and P22 were deployed perpendicular to the two dip lines. Along line P18 a high velocity lower margin wedge is observed and modeled (Figs. 4.12-4.13). Beneath the lower margin wedge a thin LVZ is assumed based on the model result of dip-line P24. A clear refraction phase P_{umv} through the upper margin wedge with velocities ranging from 4.3 km/s to 5.0 km/s was recorded on all stations (Fig. 4.5). The thickness of the upper margin wedge is 5.1 km in northwestern part and decreases to 3.1 km in southeastern part (Profile 18, Fig. 4.5). It is also found at a more shallow depth when approaching Osa Peninsula. The top of the lower margin wedge is constrained by a clear reflection phase P_{tlmP} and refraction phase P_{lmw} at profile distance km 40-45 (Fig. 4.12). A distinct plate boundary reflection phase P_{bP} is seen on most record sections (Figs. 4.14-4.15). In Figure 14, the refraction phase P_{loc} with velocities of 6.0-7.1 km/s through the lower oceanic crust is observed at profile distance km 40-45. In Figure 4.15, a refraction phase P_{uoc} through the upper oceanic crust with velocities of 5.1-5.6 km/s is observed and it can be used to constrain the bottom interface of the 'megalens'/plate boundary. On line P22, the deep phases P_n and P_{mP} were not observed on any station records and the Moho can not be constrained on this line. If the result from the dip line is projected along the profile, it should appear at offsets of 23 km at about 16 km depth (Fig. 4.5).

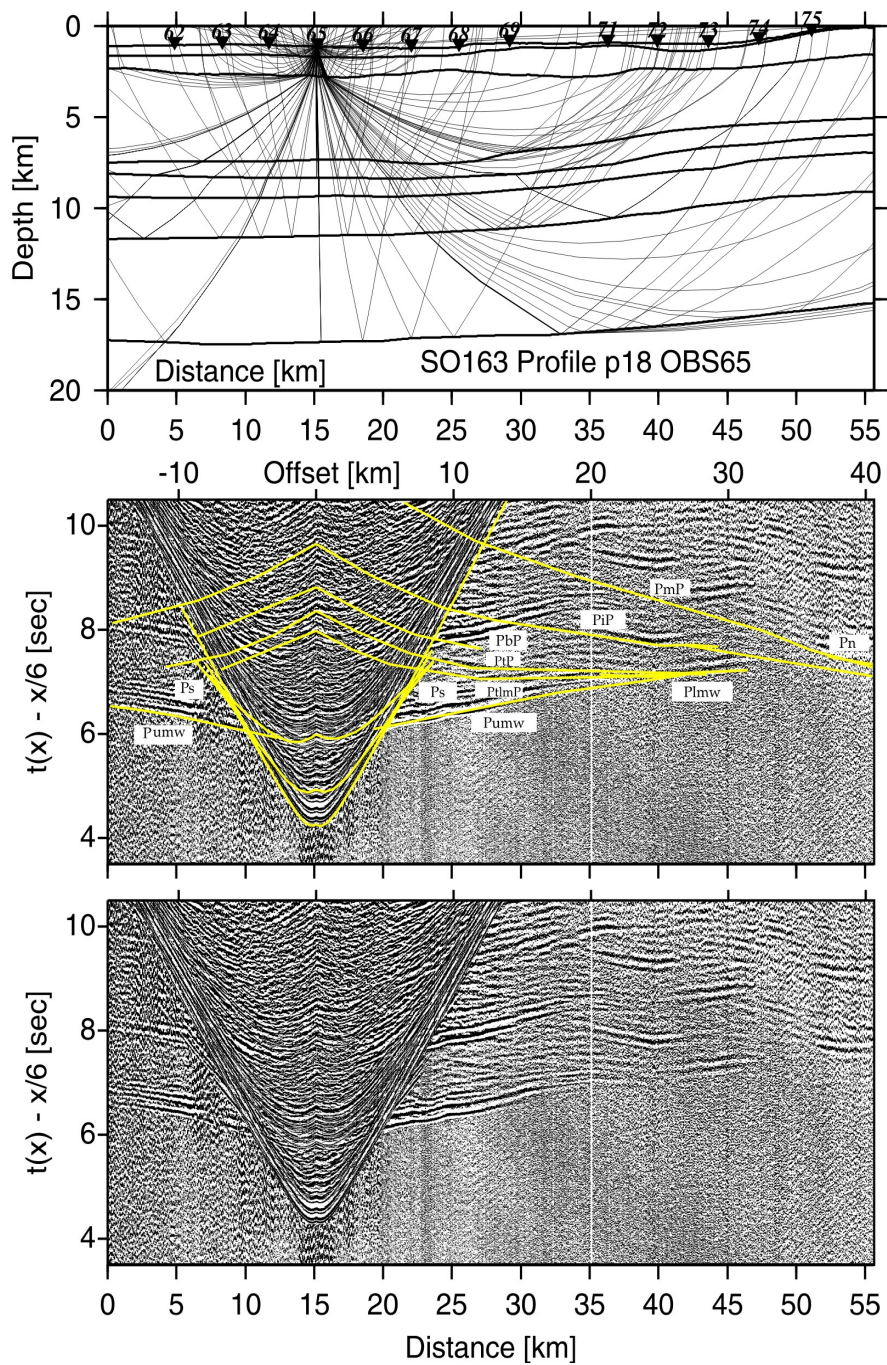


Figure 4.12. Record section and ray diagram for station OBH65 deployed along the strike-line SO163-P18. Please refer to Fig. 4.6 for display information. Strong phases P_{lmP} and P_{lmw} track the lower margin wedge. The reflection phase P_{iP} tracks the top of the lower oceanic crust. The oceanic crust-mantle boundary is recorded as reflection P_{mP} .

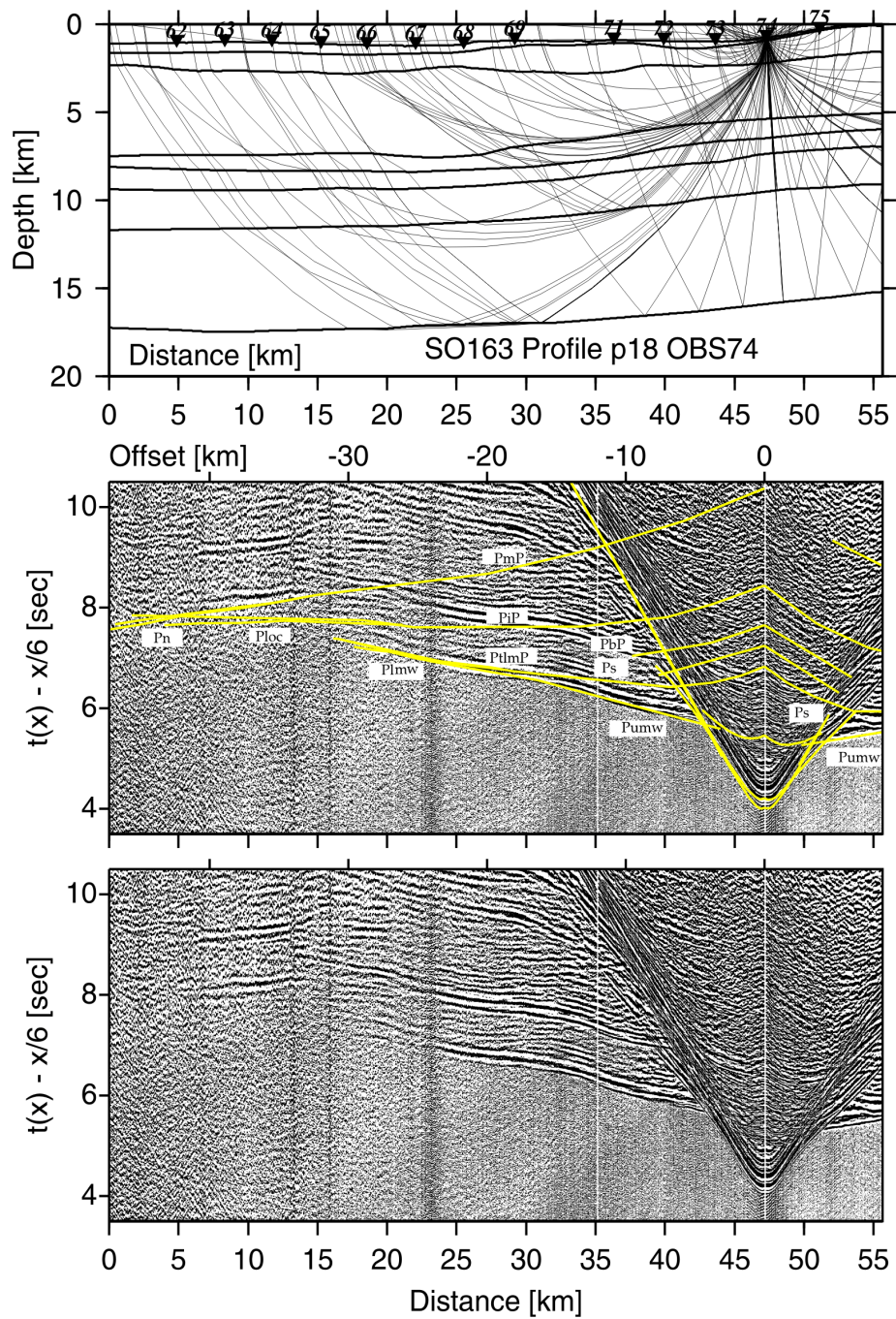


Figure 4.13. Record section and ray diagram for station OBH74 deployed along the strike-line SO163-P18. Please refer to Fig. 4.6 for display information. Phase Plmw travels through the lower margin wedge. The oceanic crust-mantle boundary is tracked by phases PmP and Pn.

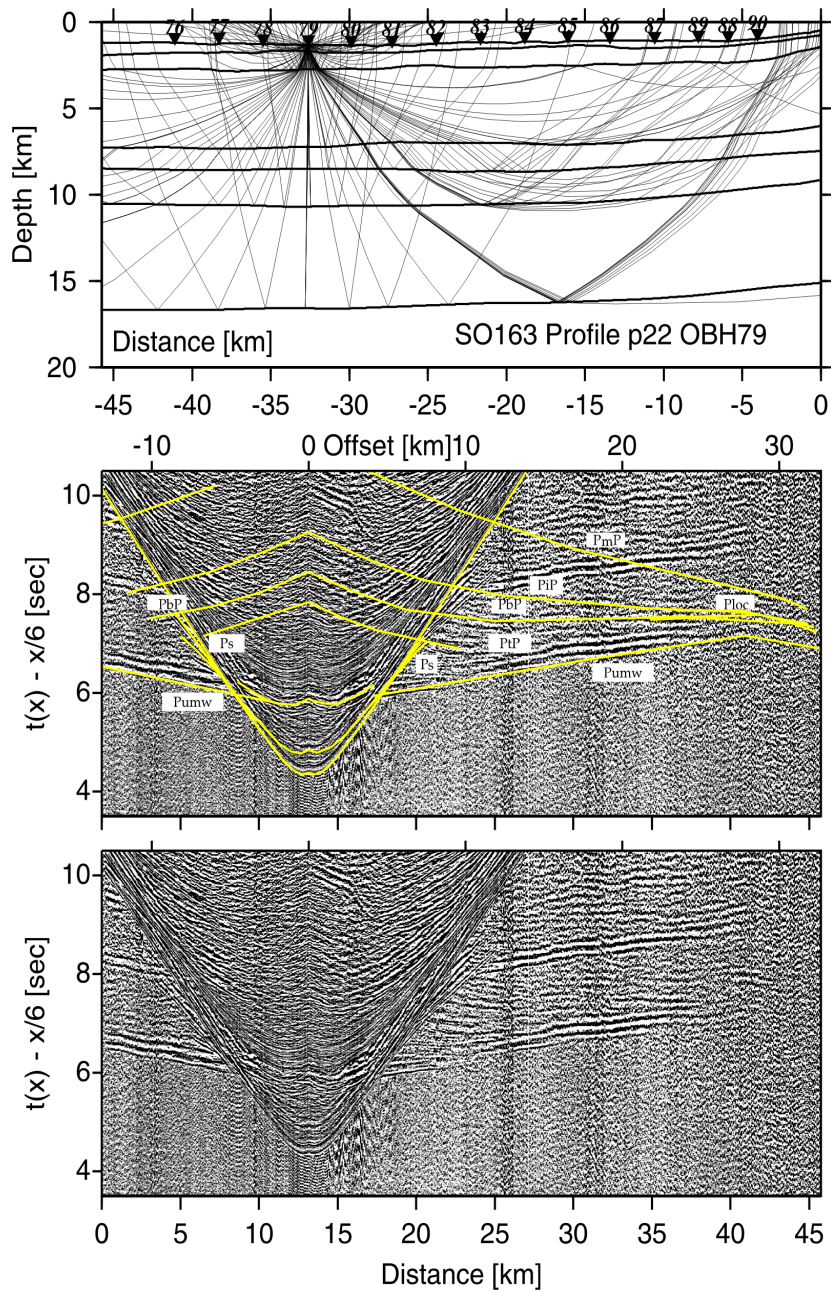


Figure 4.14. Record section and ray diagram for station OBS79 deployed along the strike-line SO163-P22. Please refer to Fig. 4.6 for display information. The pre-critical reflection phase PtP tracks the top of the ‘megalens’. The plate boundary reflection PbP tracks the downgoing slab. The reflection phase PiP records the top of the lower oceanic crust and the refraction phase Ploc travels through the lower oceanic crust.

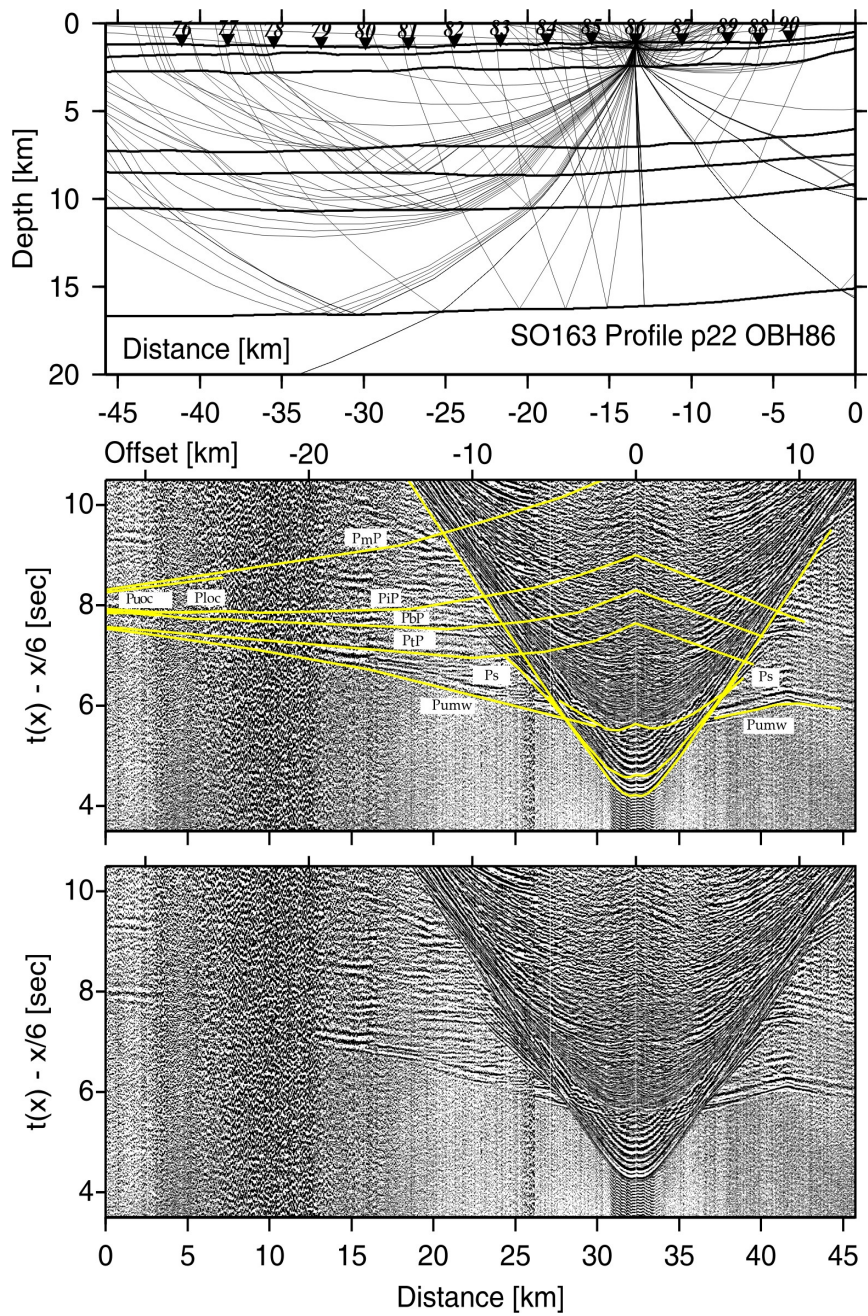


Figure 4.15. Record section and ray diagram for station OBH86 deployed along the strike-line SO163-P22. Please refer to Fig. 4.6 for display information. The pre-critical reflection phase PtP tracks the top of the ‘megalens’. Phases Puoc and PbP track the downgoing slab.

4.4.3 Amplitude modelling of wide-angle data

Along the two strike-lines there are only minor lateral velocity variations. Thus we can use the reflectivity method (Fuchs and Mueller, 1971; Mueller, 1985; Sandmeier and Wenzel, 1986) for one-dimensional amplitude modelling. Please refer to 3.2.2 for details on parameters and calculations. A comparison of the data to synthetic seismograms is displayed for OBH 88 in Figure 4.16. OBH 88 records the subducting plate beneath the bottom of the ‘megalens’ at about 8 km depth. Using the 1D velocity-depth function gained from the forward modelling as a reference model, we adjust the vertical velocity gradient within the margin wedge to match the amplitude-versus-offset variations. A vertical velocity gradient of approximately 0.22/s and constant Q_p values of 50 within the margin wedge will reproduce the refracted phase through the upper margin (Pumw) within 30 km offset (Fig. 4.16a-c). A decrease of the vertical velocity gradient by 0.03/s will enhance the appearance of the Pumw arrivals at offsets larger than 30 km (Fig. 4.16e). The refraction through the upper margin wedge (Pumw) as well as the reflection from the plate boundary (i.e. bottom of the ‘megalens’) and the top of the LVZ are well reproduced (Fig. 4.16b). Reflection amplitudes from the bottom of the ‘megalens’ increase from 11 km offset, whereas significant amplitudes from the reflection PbP appear at offsets of about 11-19 km (Fig. 4.16a). The velocity-depth profile used for the amplitude modelling is shown in Figures 4.16c and e. A 200-250 m thick layer of decreased velocities above and below the ‘megalens’ can best reproduce the reflection similar to the original data. Although the appearance of the reflection phases from two extreme low velocity layers is obscure due to noise and the interference with the multiple, they still may be discerned in the data (marked by arrows in Fig. 4.16a) and in the synthetic seismogram. The appearance of all other record sections is rather similar. The plate boundary is clearly indicated by a bright reflection in the MCS data and the amplitude of this reflection was explained by the presence of sediment and elevated pore pressure (Flueh, et al., 1999). The amplitude modelling suggests that the ‘megalens’ is bounded by a low velocity zone. Minor discrepancies in the travel times of real and synthetic data must be expected due to ray focusing and defocusing effects (Kopp et al., 2001).

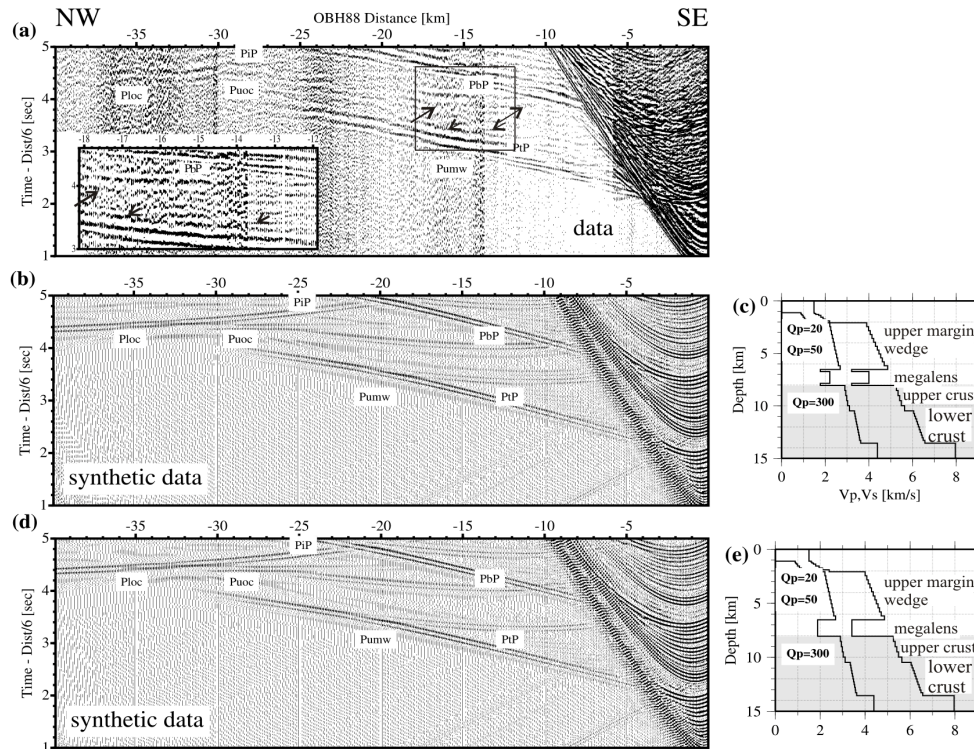


Figure 4.16. 1-D reflectivity modelling for OBH 88 deployed along the strike-line P22. (a) The different seismic phases are identified from the data of OBH 88. Phase PtP shows the reflection from the top of the first LVZ and PbP shows the reflection from the bottom of the second LVZ. The arrows show the reflections from the bottom and top of the two extreme low velocity thin layers. Lower inset shows an enlarged part indicated by a box in the data. (b) shows the preferred synthetic seismogram matching the data and (c) displays the corresponding velocity-depth profile. (d) The low velocity gradient within the margin wedge and only one LVZ in the velocity-depth profile are shown for comparison. Reflections from a single LVZ cannot adequately match the data. Source signal input is a 12.5 Hz Fuchs-Mueller signal. In the P- and S-wave velocity-depth profiles, the depth range of the subducted slab is grey shaded.

4. Model sensitivity and uncertainty tests

Sensitivity analysis of the velocity and the geometry of the ‘megalens’ were done by changing the inter-layer seismic velocities and the depths of the top interface of the ‘megalens’ using the forward modelling tool ‘MacRay’ (Luetgert, 1992). Figure 4.17 shows the match between the observed and predicted travel times for different seismic velocities and fixed top and bottom interfaces of the ‘megalens’. Assuming a constant seismic velocity of 3.2 km/s or 4.5 km/s within the ‘megalens’ does not fit well the predicted travel time (phase PbP) within the assigned 50 ms picking uncertainties (root mean square-RMS misfits >80 ms) (Fig. 4.17b). The best match of the calculated travel time curve to the observed data is achieved if we assume seismic velocities which increase linearly from 3.8-4.3 km/s. Figure 4.17b shows that the travel time curve is also strongly sensitive to depth changes (+/- 200 m) of the top interface of the ‘megalens’.

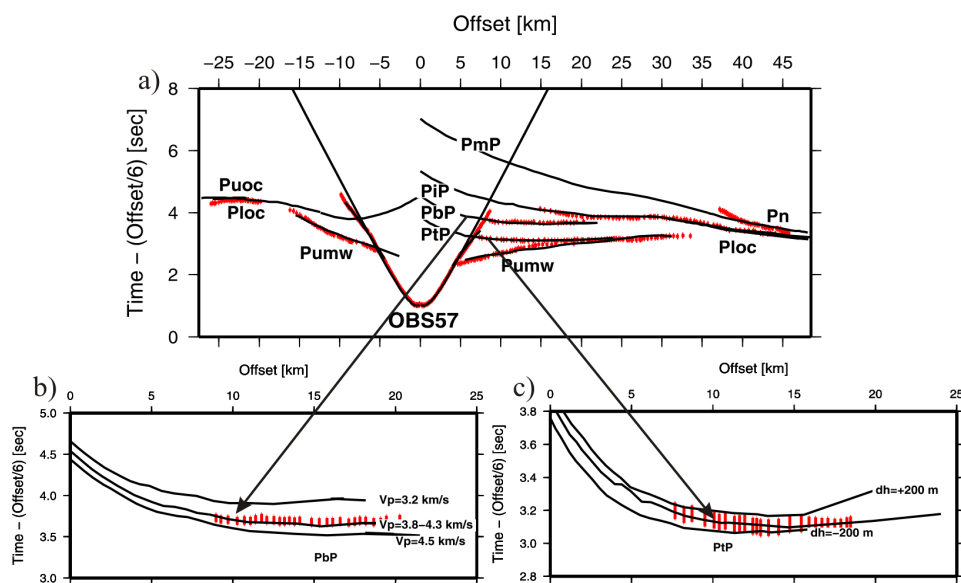


Figure 4.17. Sensitivity tests of the velocity and the geometry of the top and the bottom of the megalens demonstrated for OBS57. P-wave velocities of 3.2 km/s, 3.8-4.3 km/s, and 4.5 km/s within the layer of the megalens were calculated and compared to the observed travel times (b). Two different depths (± 200 m) of the top interface of the megalens were chose to show the fitting of the travel time curve. Observed traveltimes picks with 50 ms error are shown in red.

In order to assess the uncertainties of the velocity field and the depth of the

reflector, we used the tomographic inversion method of Korenaga et al. (2000) to apply a nonlinear Monte Carlo method (Tarantola and Valette, 1982; Tarantola, 1987; Korenaga et al., 2000). We constructed 100 Monte Carlo ensembles by inverting data with random errors with random initial velocity models. The 100 2-D initial velocity models were built by adding velocity values (randomly chosen between certain predefined limits) on a reference model beneath the basement. In addition, 100 noisy travel time data sets were constructed by adding random phase errors (± 50 ms) and common-receiver errors (± 50 ms) on the original data set (Zhang and Toksöz, 1998; Korenaga et al., 2000). Finally, we inverted each velocity model and corresponding reflector together with a noisy data set to estimate the influence of the starting model and the effect of realistic travel time errors. We applied a top-bottom strategy to run the inversion step for each reflector respectively. We applied the random velocities on our 2-D forward model of P15 including two floating reflectors (top and bottom of the ‘megalens’, random variations within ± 1 km) in the upper plate and one reflector (Moho, random variations within ± 2 km) in the lower plate. After 10 iterations of the inversion process, 100 inversion velocity models for the first reflector updated as 100 initial models for the second reflector. Travel time RMS misfits reduced dramatically from the beginning several hundred ms to about 70-90 ms and allowed us to assess the uncertainty of the velocity field.

The average and uncertainty of model parameters obtained by averaging all Monte Carlo solutions and computing the corresponding standard deviation is shown in Figs 4.18 (a), (c) and (e). Velocity uncertainties of the upper plate are usually lower than 0.15 km/s within the margin wedge and are lowest (< 0.05 km/s) in the upper margin wedge. Uncertainties are slightly higher within the lower margin wedge (0.06-0.16 km/s) because of sparse ray coverage (Fig 4.18b). The largest velocity uncertainties occur within the LVZ (‘megalens’) and reach up to 0.15 km/s (Fig. 4.18c). The depth uncertainties of the first and the second reflector are small and reach up to about 500 m within the range of ray coverage. The velocity uncertainties within the subducting oceanic crust are larger (0.06-0.15 km/s) because of the limited amount of available data (Fig. 4.18e and 4.18f). The Moho depth uncertainties show values around ± 1.5 km. In general, the uncertainties for upper plate are lower than in the lower plate and the velocity structure and geometry of the ‘megalens’ is a robust feature of the tomographic solutions.

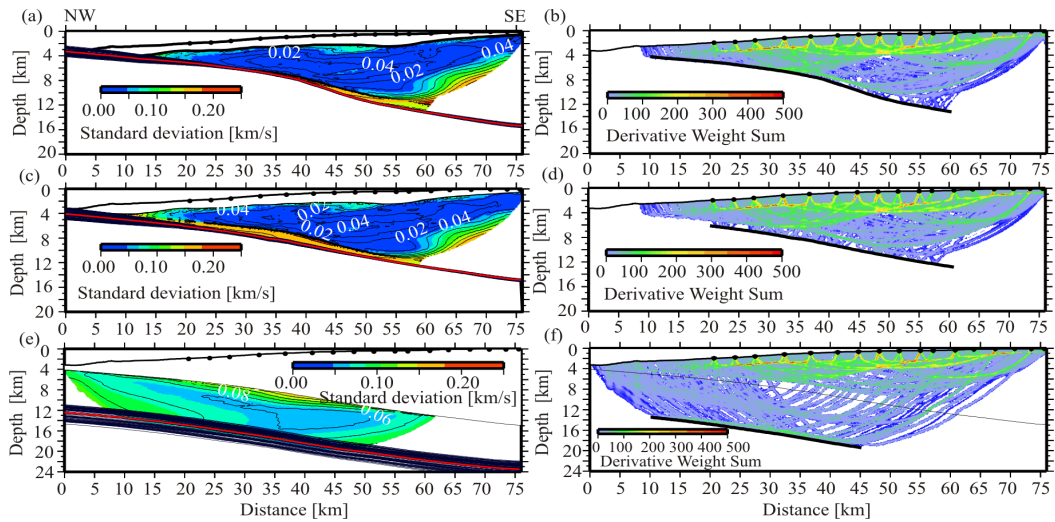


Figure 4.18. Standard deviations for velocity and reflector depth nodes derived by 100 Monte-Carlo ensembles (a, c, e) and corresponding derivative weight sum from the average 100 realizations (b, d, f). Red lines show the average depth of reflectors and contours are drawn at 0.02 km/s interval (a, c, e).

4.5. Discussion

4.5.1 Margin wedge

Below the cover of slope sediment, the margin wedge is defined by high velocities (4.3-6.1 km/s). Based on the P wave velocity variations we divide the margin wedge into the upper margin wedge with velocities ranging from 4.3-5.0 km/s and the lower margin wedge with velocities from 5.2-6.1 km/s. The top of the upper margin wedge is clearly imaged in the MCS dataset and also reliably modeled based on the wide-angle data. Its top is cut by numerous normal faults and indicates the extensional forearc stress environment (Fig. 4.3). The interface separating the upper and lower margin wedge is defined by a sharp velocity increase from 5.1 km/s to 5.5 km/s and is well constrained by our data (see Fig. 4.11). The relative high velocities of the lower margin wedge result in a velocity inversion at the transition to the subducted plate landward of OBS 101 (P24) and OBS54 (P15). The lower margin wedge terminates underneath the middle slope beneath OBH(S) station 102 and 55. On strike-line P22 it is not observed.

The origin and composition of the margin wedge is defined by geophysical observations and by comparison to neighboring stratigraphic sections onshore. The margin wedge off Nicoya and Central Costa Rica was interpreted as an offshore extension of the Nicoya Complex ophiolitic rocks (Ye et al., 1996; Stavenhagen et al.,

1998; Christeson et al., 1999; Sallarès et al., 2001). The uppermost unit of the Nicoya Complex onshore was constrained by land shots and shows velocities varying from 4.2-4.9 km/s. The middle unit of the Nicoya Complex displays velocities landward of the coastline varying from 4.6-5.5 km/s and velocities at the top of wedge varying from 3.6-4.7 km/s (Christeson et al., 1999). Our results for central Costa Rica show that the upper margin wedge is characterized by velocities varying from 4.0-5.2 km/s. An across-strike increase of velocities from 4.0 km/s at approximately 12 km landward of the trench to 4.4 km/s off the coastline (Fig. 4.5) is observed. The lower Nicoya complex (Christeson et al., 1999) corresponds to our lower margin wedge in terms of velocities. It indicates a low velocity gradient, but the velocity also decreases trenchward from 5.5 km/s to 5.0 km/s. This velocity information suggests that the upper and lower margin wedge can be interpreted as an offshore extension of the upper and the lower Nicoya complex.

The extent of the lower margin wedge within the forearc was not identified from previous wide-angle seismic studies. Previous seismic profiles could not resolve the transition between the upper margin wedge and the lower margin wedge (Ye et al., 1996; Stavenhagen et al., 1998; Christeson et al., 1999; Sallarès et al., 1999, 2001), whereas our data constrain the extent and termination of this layer. The corresponding dense ray coverage is shown in Figure 4.11.

Based on the approach of Clift and Vannucchi [2004] we calculate the average slope angle over a distance of 50 km to eliminate small-scale anomalous trends. A large slope angle ($> 8^\circ$) occurs close the trench over a distance of 5 km. The mean forearc slope angles are 3.2° for dip-line P15 and 3.8° for dip-line P24. The average dip angles of the oceanic plate are 9.0° for P15 and 9.1° for P24. These parameters then yield forearc tapers of 12.2° for P15 and 12.9° for P24, which are larger than observed to the northwest at 86°W (taper angle of 7.6°) and smaller than for Mexico (99°W), Guatemala (91°W) and Nicaragua erosive margins documented by Clift and Vannucchi [2004], but fall well within the range of erosive margins.

4.5.2 ‘Megalens’ and LVZ

Subducted sediment overlying the oceanic igneous crust is observed all along the convergent Pacific margin offshore Costa Rica and is manifested in a LVZ (Ye et al., 1996; Stavenhagen et al., 1998; Christeson et al., 1999). Along our dip lines, the LVZ shows a constant velocity of 3.2 km/s from the trench to approximately 20 km landward of the deformation front. The LVZ extends beneath the margin wedge with velocities increasing to 4.3 km/s at depths exceeding 10 km (Fig. 4.5). The ‘megalens’ is concealed between the margin wedge and the subducted slab, and was first

identified on MCS profile SO81 Line 4 (Hinz et al., 1996). We iteratively converted our velocity-depth model of P15 in two-way time to match the MCS data. In our model refracted phases from the upper oceanic crust and reflection phases from the bottom of the ‘megalens’ are observed and modeled on several OBH(S) stations, therefore we can be confident to constrain the bottom velocity of the ‘megalens’ with 4.3 km/s. The amplitude modelling reveals a LVZ bounding the ‘megalens’, which coincides with the high amplitudes observed in the MCS data.

Gravity surveys in our study area show a broad negative free-air anomaly (-50 to -30mgal) (Barckhausen et al., 1998), whereas seamounts and the Quepos plateau generate a positive gravity anomaly. A gravity model by Barckhausen et al., [1998] distinguishes between a model with and without a seamount. Their calculated positive gravity anomaly indicates a buried seamount beneath the margin, however, along our profiles, the gravity pattern cannot be correlated to a possible subducted seamount model. Subducted seamounts have however been detected at different margins worldwide: a 13 km thick by 50 km wide seamount at a depth of 10 km was imaged in the Nankai subducted zone (Kodaira et al., 2000), with P-wave velocities of 5 km/s increasing to 7.2 km/s. By comparison, the size of the ‘megalens’ is much smaller (1.5 km thick by 15 km wide) and its seismic velocities are lower (3.8-4.3 km/s). This is also true in comparison to the Moresby seamount in the Woodlark Basin ($v_p > 6$ km/s) (Zelt et al., 2001). At the central Ecuador margin, an 8 km long by 0.7 km high sediment lens at approximately 4 km depth was identified from seismic images (Sage et al., 2006). This sediment lens is much smaller than the Costa Rica ‘megalens’ (Fig. 4.19a) and is interpreted as material accumulated in the wake of a subducting seamount. Based on our observations, the ‘megalens’ cannot be explained by a seamount tunnelling mechanism.

4.5.3 Subducted oceanic crust

The igneous oceanic crust is divided into an upper and a lower crustal layer with varying velocity gradients. On the two dip-lines, the refracted and reflected phases constrain the interface within the oceanic crust (Figs. 4.6-4.10). The strong reflections from the plate boundary are all clearly observed (Fig. 4.6, Figs. 4.8-4.9). Deeper PmP and Pn phases are observed on a number of stations (OBS57, Fig. 4.8; OBH106, Fig. 4.10; OBS74, Fig. 4.13), and provide some constraint on the deep part of the model. On the strike-line P18, due to the higher velocities of the lower margin wedge (5.2-5.5 km/s) with respect to the upper oceanic crust, no refracted waves from the upper oceanic crust can be observed, but the strong wide-angle reflection PiP and pre-critical reflection PbP can be used to constrain the interfaces within the oceanic

crust (Fig. 4.12). At Quepos plateau, a 3 km thick basalt layer was interpreted as upper crust Layer-2A (Walther, 2003). Along our profile, the oceanic crust shows an increased thickness of 7.5-8 km corresponding to crustal thickening towards Cocos Ridge. Line SO81-200 to the north (line d in Fig. 4.2) displays a crustal thickness of 7.0 km (Ye et al., 1996), whereas the oceanic crust to the south increases to a thickness of 14 km along the neighboring refraction profile (line f in Fig. 4.2) (Stavenhagen et al., 1998), which is located on the flank of the Cocos Ridge.

4.5.4 The nature of the ‘megalens’

Understanding the nature and origin of the ‘megalens’ may be important to the concept of basal erosion in convergent margins. The nature of the ‘megalens’ was not unambiguously resolved since its first imaging in 1992 due to a lack of detailed seismic velocity information. The current study clearly precludes a seamount origin.

Along the plate boundary fluids play an important role to facilitate basal erosion of the upper plate (Le Pichon et al., 1993; von Huene and Ranero, 2003; Sallarès et al., 2005; Ranero et al., 2008). Initial sediment dewatering processes involve pore water squeezed from the subducted sediment at temperature domains of < 60 °C (Fig. 4.19a). At greater depth and increased temperatures of 50°C - 160°C, mineral dehydration reactions pose the dominant process generating fluids at the plate boundary (e.g. Moore and Vrolijk, 1992; Hensen et al., 2004). Along the upper boundary of the ‘megalens’ the expected temperatures fall between 100°C-120°C (compare Fig. 4.19). As suggested by Ranero et al., 2008, plate boundary fluids will migrate upward through the fractured upper plate where they are detected at seeps. In the vicinity of our seismic line, expulsion of fluids generated at deep structural levels occurs at Mound 11 mud volcano (Hensen et al., 2004) (Figs. 4.4 and 4.19a). Geochemical evidence from Cl-depleted fluid samples of Mound 11 (see Fig. 4.4 for location) and other seeps along the Costa Rica margin (Hensen et al., 2004) as well as the inverse amplitude polarity of the plate boundary reflections (Ranero et al., 2008) suggests a deep origin of the fluids. Compaction, increased porosity, loss of sediment and the smectite-illite transition can raise the seismic velocity of sediment to ~ 4 km/s at about 8 km depth (Sage, et al., 2006), thus increasing the velocity to values comparable to the ‘megalens’ seismic velocities. The observed velocities of 3.8 km/s to 4.3 km/s in the ‘megalens’ may best be explained by a hybrid composition, consisting of subducted sediment, fractured upper plate material and fluids. The lens-shaped feature is part of a LVZ (Fig. 4.19b), however, the modeled velocities are higher than the seismic velocities of 2.2-2.8 km/s determined for sediment lenses at the Ecuador margin (Sage et al., 2006). An exclusive composition of subducted trench

sediment is less likely due to the higher velocities as well as much larger dimensions of the Costa Rica ‘megalens’ compared to the Ecuadorian sediment lenses.

The fate of the ‘megalens’ remains enigmatic: its current position aligns with the lower margin wedge and the onset of local seismicity beneath the middle slope. The microseismicity events from a local network (Dinc et al., 2007) are projected onto the velocity model in Fig. 19 b and indicate the distribution of the intraplate seismicity and oceanic crustal seismicity. The lack of the microseismicity over the ‘megalens’ suggests slow displacement there.

4.6. Conclusions

The modelling and interpretation of the seismic wide-angle data, combined with coincident seismic reflection data and amplitude modelling, have enabled us to construct a detailed velocity-depth model covering the Pacific margin of central Costa Rica. The data clearly define two layers within the margin wedge, the high velocity gradient upper margin wedge with velocities of 4.3-5.0 km/s and the reduced velocity gradient lower margin wedge with velocities ranging from 5.2-6.1 km/s. The leading edge of the lower margin wedge terminates above the ‘megalens’ about 32 km landward of the trench. The two strike-lines confirm the seaward termination of the lower margin wedge. The ‘megalens’ is 15-20 km wide and has a thickness of 1-1.5 km. Its seismic velocities fall between 3.8 km/s and 4.3 km/s and are clearly much lower than the velocities of subducted seamounts or plateaus. The ‘megalens’ is a low velocity body with respect to the margin wedge above and is bounded by thin layers of lower velocities above and below. Our preferred interpretation is that the ‘megalens’ is a mixture product, which consists of a buried sedimentary mélange including rocks sheared from the lower plate and highly fractured material derived from the upper plate by basal erosion. The LVZ above the ‘megalens’ shows a discontinuous amplitude distribution in the seismic image (Fig. 4.19 a) and is caused by fluids and associated localized pore pressure anomalies.

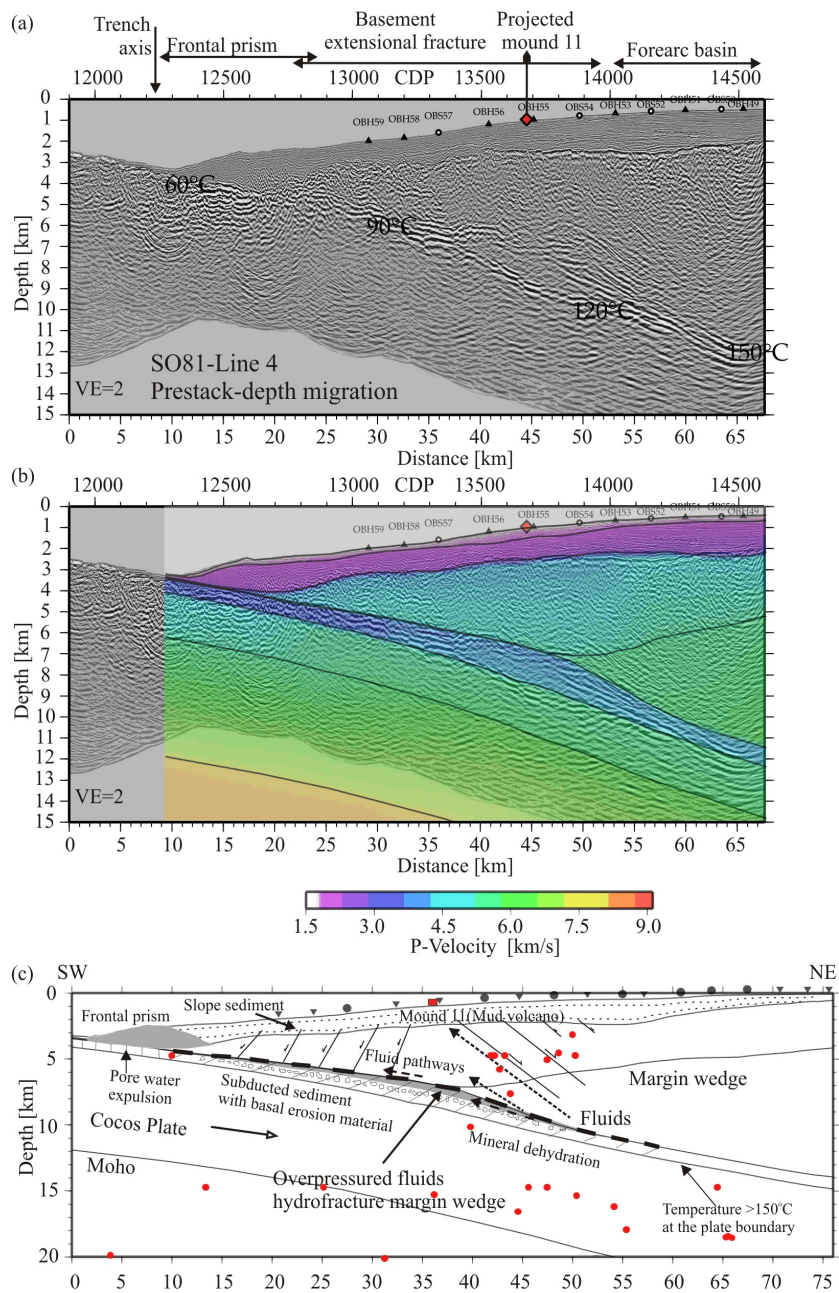


Figure 4.19. Seismic image and the interpretative velocity structure of the central Costa Rica subduction zone. (a) Prestack depth-migrated SO81-Line 4 (Ranero and von Huene, 2000). Basement extensional fractures are indicated by normal faults. The OBH(S) stations are marked on the seafloor. The location of Mound 11 (mud volcano) is projected onto the Line 4 (see Fig. 4 for a detailed location). Plate-boundary temperatures are from Ranero et al., [2008]. (b) Superimposed image of MCS Line 4 and the seismic velocity field of Profile 15. (c) The interpretative model of the basal erosion structure. Fluids are generated by mineral

dehydration and transported upward to the mound site (Hensen et al., 2004; Ranero et al., 2008). Red dots indicate local seismicity (Dinc, et al., 2007).

Chapter 5

Margin architecture and seismic attenuation in the central Costa Rican forearc

5.1. Introduction

Seismic attenuation is an inherent property of wave propagation and a measure of the total energy loss when a seismic wave propagates through the earth. The amplitude and waveform characteristics of seismograms may be modeled using the reflectivity method (Fuchs and Mueller, 1971; Braile and Smith, 1975), adapted to the calculation of pressure or displacement waveforms and thus suitable for either hydrophone or seismometer refraction recordings (Kennett, 1977). We employ the seismic attenuation factor for the calculation of synthetic seismograms to investigate the effect of inelastic attenuation in the Costa Rican margin wedge northeast of the Quepos Plateau (Fig. 1).

The Pacific margin of Costa Rica is characterized by the subduction of the oceanic Cocos plate underneath the Caribbean plate and has been imaged along several refraction profiles deployed since 1996 (Ye et al., 1996; Stavenhagen et al., 1998; Christeson et al., 1999; Walther et al., 2003; Zhu et al., 2009). The age, thickness and seismic velocities of the downgoing plate vary from the Nicoya Peninsula in the northwest to the Osa Peninsula in the southeast (Fig. 1, inset). Whereas the thickness of the oceanic crust increases from 5-6 km in the northwest to up to 14 km in the southeast, the age decreases from 22-24 Ma to 15-18 Ma from NW to SE as inferred from the seafloor spreading anomalies (Barckhausen et al., 2001). Along most profiles, an upper mantle velocity of 8.0-8.1 km/s is revealed. An exception to this is the area underneath the Quepos plateau where upper mantle velocities of 7.6-7.8 km/s prevail. Comparably low mantle velocities are also imaged underneath the outer flank of the Cocos Ridge, where it has been attributed to remnants of mafic material in the upper mantle or a plume signature (Walther, 2003). The core of the forearc margin wedge incorporates a fragment of the Caribbean oceanic plateau (Nicoya complex) (Hauff et al., 1997; Sinton et al., 1997). This igneous rock unit forms the forearc basement and is covered by a sediment apron (Ye et al., 1996). Fronting this unit is the frontal prism, which consists of accreted upper

plate sediment (von Huene et al., 2000).

To the southeast, from the tip of Nicoya Peninsula to the northern limit of Osa Peninsula, numerous bathymetric features dot the incoming plate and upon entry in the trench modulate forearc deformation and morphology (e.g. Dominguez et al., 1998; Ranero and von Huene, 2000; von Huene et al., 2000). In addition to tectonic erosion caused by the impinging bathymetric features (von Huene et al., 1995), outer forearc kinematics are characterized by widespread subsidence resulting from subduction erosion (Lallemand et al., 1992; Vannucchi et al., 2003), i.e. material removal from the base of the upper plate.

One of the major objectives of examining the lateral variations of Qp values is to evaluate lateral seismic velocity and physical state variations of the margin wedge. The seismic velocity structure of the Costa Rican margin wedge has been obtained by a number of refraction experiments (e.g. Ye et al., 1996; Stavenhagen et al., 1998; Christeson et al., 1999; Walther, 2003; Zhu et al., 2009) and reflects the tectonic segmentation into a frontal prism, middle prism and inner prism as introduced by von

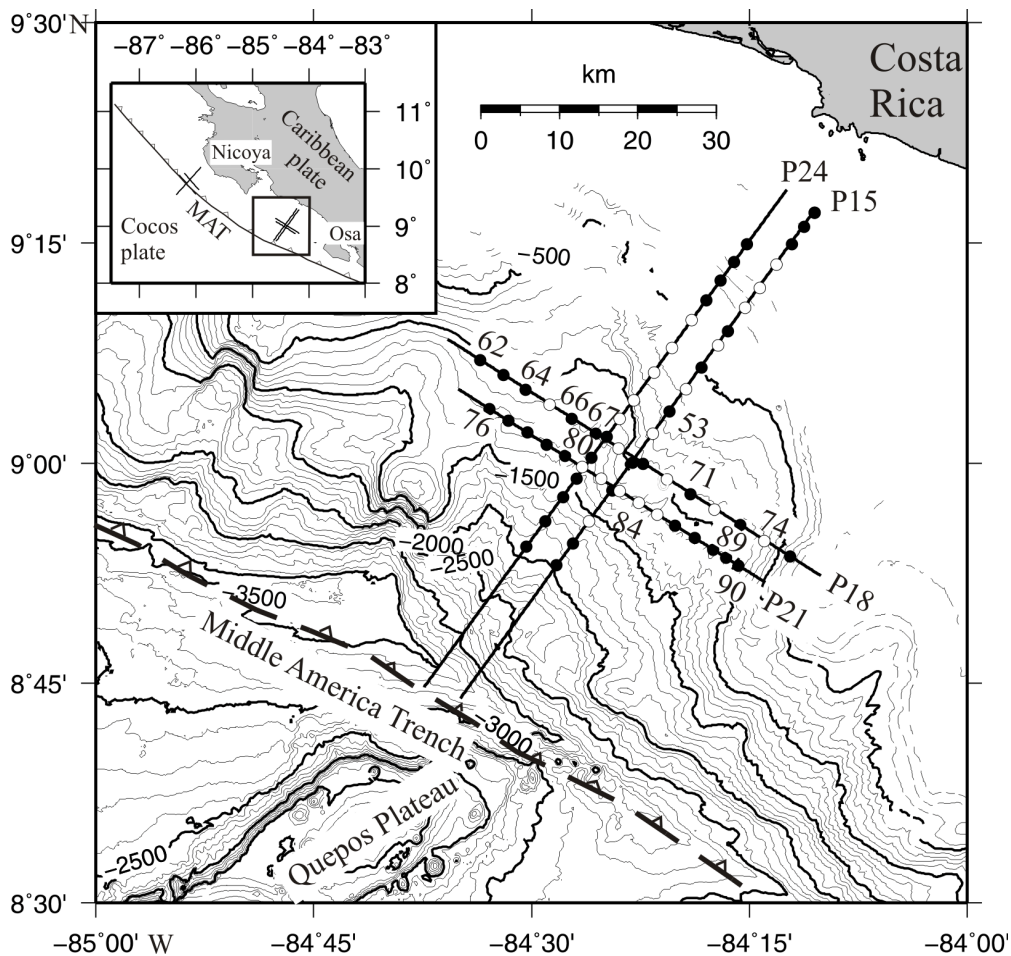


Figure 5.1. Location map of seismic refraction profiles discussed in this study. Circles indicate positions of 40 ocean bottom hydrophones (OBH) (black) and 21 ocean bottom seismometers (OBS) (white) along the two strike and two dip lines. Stations used during amplitude modeling are marked by numbers. Seafloor topography is contoured at 100 m intervals. The inset map shows locations of the previous wide-angle seismic experiment by Christeson et al. (2000) offshore Nicoya Peninsula as well as this study. MAT: Middle America Trench.

Huene et al. (2009). We expect Q_p variations to define these tectonic segments. The high signal-to-noise ratio of the first arrivals of the seismic data presented here facilitates amplitude modeling, as peak amplitudes are clearly identifiable. In this study, we firstly use seismic tomography to verify the velocity structure along two dip lines P15 and P24 and two strike lines P18 and P21 located offshore central Costa Rica (Fig. 1). We then employ the reflectivity method to constrain attenuation and velocity gradients in the margin wedge along the two strike lines. We compare our results to previous investigations of seismic attenuation conducted offshore Nicoya Peninsula, approximately 210 km to the northwest of our lines (Christeson et al., 2000) (Fig. 1). The generally low Q_p values of the margin wedge indicate a highly tectonized frontal and middle prism, characterized by a high degree of fracturing. The seismic attenuation variations from the frontal prism to the middle prism document the lateral variations in lithology and physical state of the rock units.

5.2. Wide-angle Seismic Data

In 2002, a total of 42 IFM-GEOMAR ocean bottom hydrophones (OBH) (Flueh and Bialas, 1996) and 22 ocean bottom seismometers (OBS) (Bialas and Flueh, 1999) were deployed along four seismic profiles located about 25 km northeast of the Quepos Plateau (Zhu et al., 2009) (Fig. 1). Instruments were deployed along two dip lines P15 and P24 and two strike lines P21 and P18 (Fig. 1). The two dip lines P15/P24 were shot with a G-gun cluster (total volume 1800 cu.in) whereas the data along the two strike lines P18/P21 were acquired using a 32 ltr. Boltgun (1952 cu.in). Both source types generated a seismic signal with frequencies from 4 to 40 Hz. A trigger interval of 30 s at a speed of 3.5 knots resulted in an average shotpoint distance of 54 m. Instrument positions on the seafloor were determined by analysis of the water wave arrivals. A time- and offset- dependent frequency filter in addition to a predictive deconvolution was applied to improve data resolution. A total of 32058 first arrival picks and 7789 secondary arrival picks from 61 stations were used as

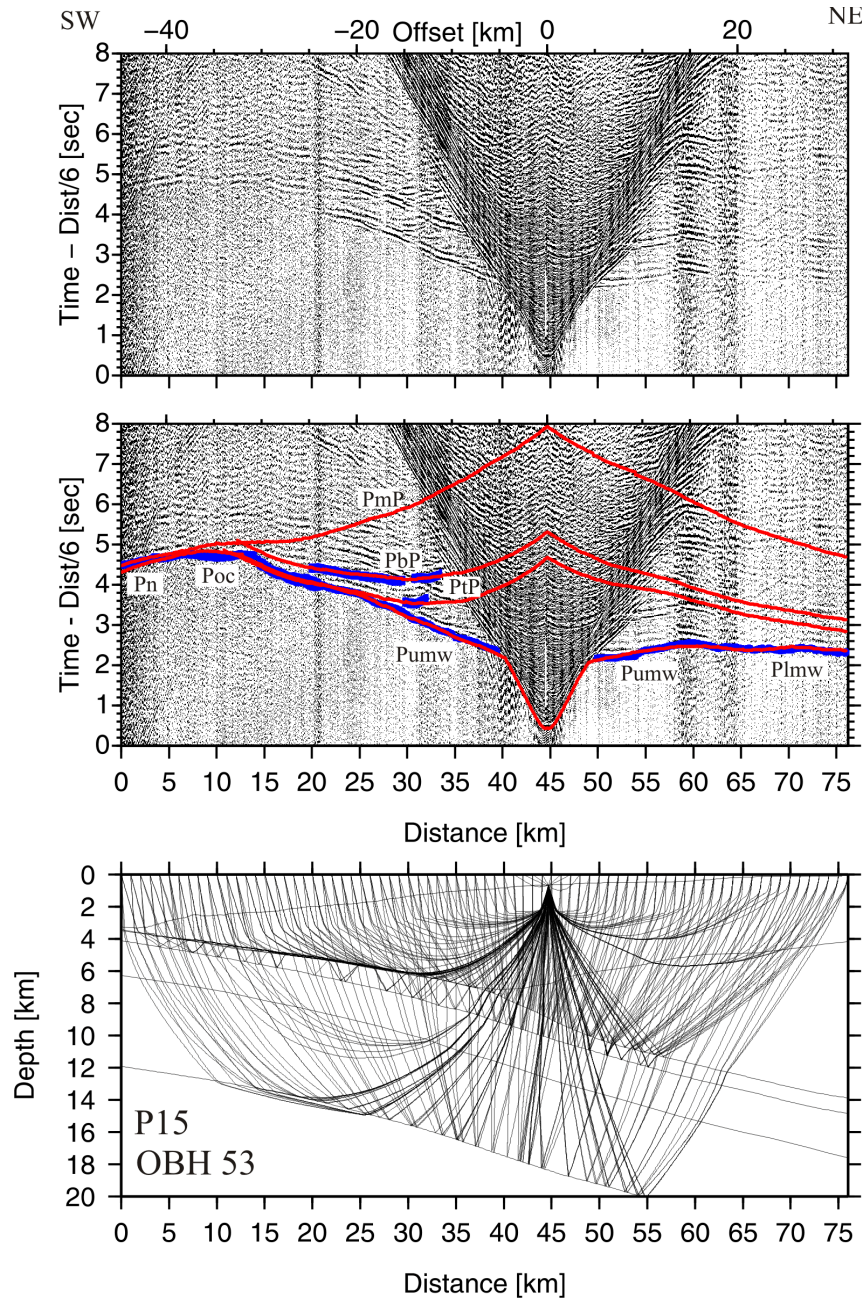


Figure 5.2. Record section and raypaths for OBH 53 deployed on profile P15. Observed data are shown in the upper panel. Picked (blue line with picking error bars) and calculated travel times (red lines) are displayed in the center panel. Ray paths and phase abbreviations are shown in the lower panel. Refracted phase Pumw travels through the upper margin wedge and Plmw travels through the lower margin wedge. Poc is refracted through the oceanic crust. Reflection phases PtP tracks the top of the décollement zone and PbP tracks the bottom of this zone. PmP and Pn phases result from the oceanic crust-mantle boundary.

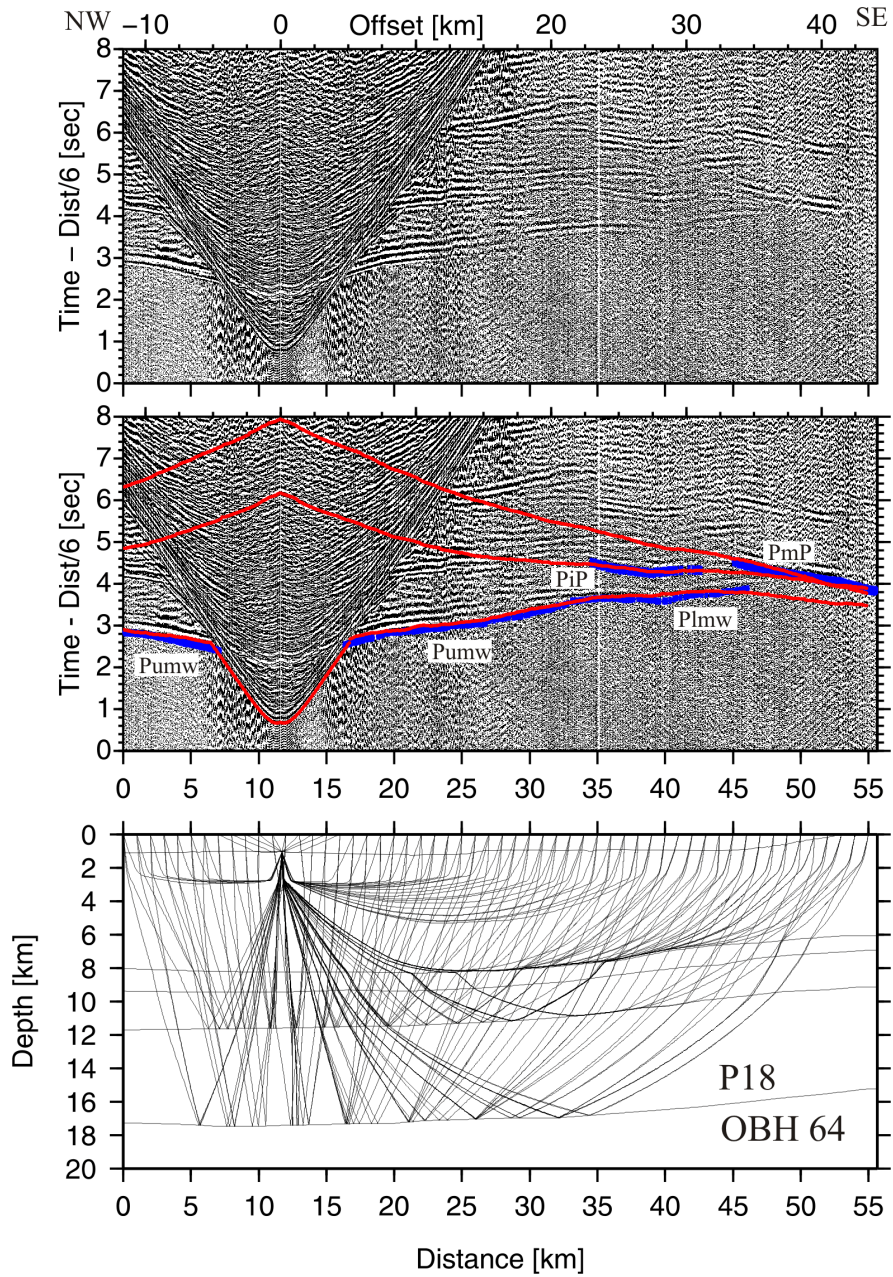


Figure 5.3. Record section and raypaths for OBH 64 deployed on strike line P18. Reflection phase PiP originates at the boundary between oceanic layer 2 and layer 3. Please refer to Figure 5.2 for display information and phase nomenclature.

input to a tomographic inversion. Comparing the reciprocity of the travel times for all possible source-receiver pairs validated phase coherency. Picking of seismic phases was conducted manually, and picking errors were assigned on the basis of the dominant period of the phase as well as data quality. We assigned 50 ms picking

uncertainties at near offsets and 70 ms at far offsets for the first arrivals, and 80 ms for secondary arrivals.

The refractions through the upper margin wedge (Pumw) and the lower margin wedge (Plmw) are clearly observed on the record sections (e.g. Figs. 2-4). Station OBH 53 records refracted arrivals through the oceanic crust (Poc) and the upper mantle (Pn) (Fig. 2). The reflections from the top (PtP) and the bottom (PbP) of the décollement zone are recorded on several stations (e.g. Figs. 2 and 4) as are the intracrustal reflections PiP and crust-mantle boundary reflections (PmP) (Figs. 3 and 4). All of these arrivals are incorporated in the tomographic inversion.

5.3. Seismic Travel Time Tomography

5.3.1 Method

The velocity-depth distribution of the seismic profiles is determined using the joint refraction and reflection travel time inversion method of Korenaga et al. (2000). The sedimentary section of the two dip lines (P15 and P24) has been modeled by forward ray tracing incorporating multichannel seismic reflection data (Zhu et al., 2009) and it is integrated in a starting model as a priori information. The fine mesh we apply in the tomographic inversion is better suited to resolve lateral variations in the short-wavelength structure compared to forward modeling. Lateral velocity variations, as observed e.g. in the upper margin wedge of our profile, are difficult to resolve using a layered model in the forward approach (Zhu et al., 2009). In Figure 5a (profile distance 45-51 km), the high velocity variation within the upper margin wedge imaged by the tomographic inversion is resolved as a robust feature as validated by resolution tests. For all profiles, first arrivals and reflection travel times from floating reflectors were inverted to retrieve the 2-D velocity field. The forward travel time calculation uses a hybrid approach based on the graph method and the ray-bending method (Moser et al., 1992). For the inversion, the velocity field is parameterized as a mesh of nodes hanging below the seafloor with laterally and vertically varying node spacing. Horizontal grid size is 0.25 km, whereas vertical grid size varies from 0.05 km at the top of the model to 0.2 km at the bottom. We used horizontal correlation lengths ranging from 2 km at the top to 8 km at the bottom and vertical correlation lengths varying from 0.5 km at the top to 2 km at the bottom. A floating reflector is represented as an array of linear segments, whose nodal spacing is independent of that used in the velocity grid. The horizontal coordinates of reflector nodes are fixed so that each node has only one degree of freedom in the vertical direction (Korenaga et al., 2000). To incorporate multiple reflectors in the inversion procedure, we used the

top-bottom modeling strategy to update the velocity model, i.e. the final velocity model with the first reflector fixed by damping serves as the initial model for the second reflector and so on. In this study, we chose to invert four reflectors corresponding to (1) the décollement, (2) the oceanic basement, (3) the upper-lower oceanic crust boundary and (4) the crust-mantle boundary (Moho discontinuity).

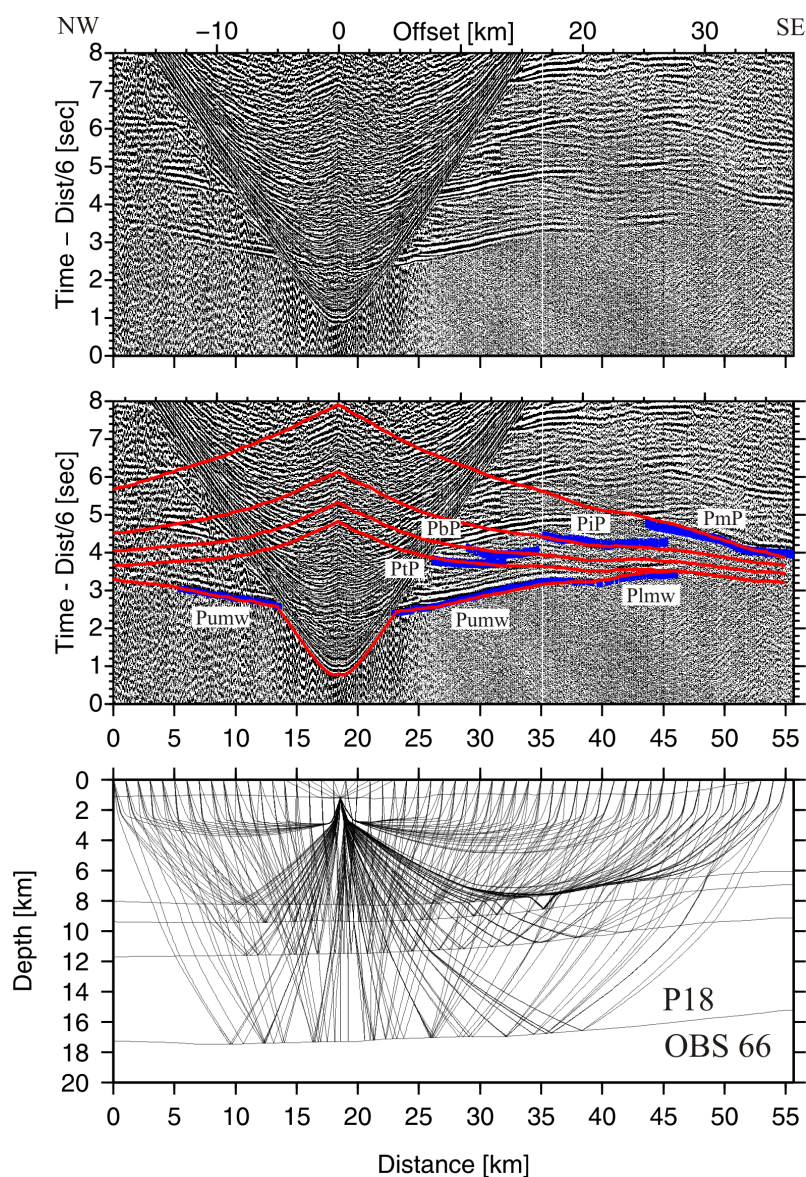


Figure 5.4. Record section and raypaths for OBS 66 deployed on strike line P18. Please refer to Figure 2 for display information and phase nomenclature.

5.3.2 Results of Tomographic Inversion and Interpretation

5.3.2.1 Seismic Structure

The marine forearc is dominated by the upper margin wedge with a high velocity gradient of 0.4/s, which decreases in the lower margin wedge (Fig. 5.5). The tomographic images display laterally increasing seismic velocities within the margin wedge. Near the tip (Fig. 5.5, profile distance km 10-18), seismic velocities increase from 3 km/s to 4.5 km/s over the margin's thickness of ~2 km. From the middle slope to the upper slope, seismic velocities range from 4 km/s to 5.5 km/s and increase from 5.5 km/s to 6.5 km/s in the lower margin wedge. The subducting Caribbean oceanic plate is divided into two layers with distinct vertical velocity gradients: The upper layer is characterized by a large vertical velocity gradient, with velocities ranging from 5.0 km/s to 6.0 km/s and is identified as oceanic layer 2. The lower layer is traced by the 6 km/s isocontour at the top and the Moho interface with velocities of 7.2 km/s at the base and is considered to represent oceanic layer 3. A uniform thickness of 2 km and 5.5 km is observed for layers 2 and 3, respectively. Along all profiles, the décollement zone between the subducting Cocos plate and overriding Caribbean plate is characterized by a velocity inversion with a mean velocity of 4.0 km/s. The thickness of the décollement zone varies from ~1.0 km to ~1.5 km and is continuous up to our model boundaries. The dense instrument spacing of 2.5 km to 3 km along the strike lines resolves fine structural variations of the margin wedge. Along strike line P18, 30 km from the deformation front, P-wave velocities of 4 km/s to 5.2 km/s are identified in the upper margin wedge and its thickness variations do not exceed 1.5 km (Fig. 5.6a). The thin lower margin wedge shows velocities of 5.2 km/s to 5.5 km/s. The seismic structure of the margin wedge as imaged along P18 correlates to strike line P21, located 35 km from the deformation front (Fig. 5.6a). P21 displays an even more homogeneous structure, with layer thickness variations not exceeding 500 m and no considerable velocity variations (Fig. 5.6b). The structure of the lower plate is clearly two-dimensional, and velocities increase with depth and distance from the trench.

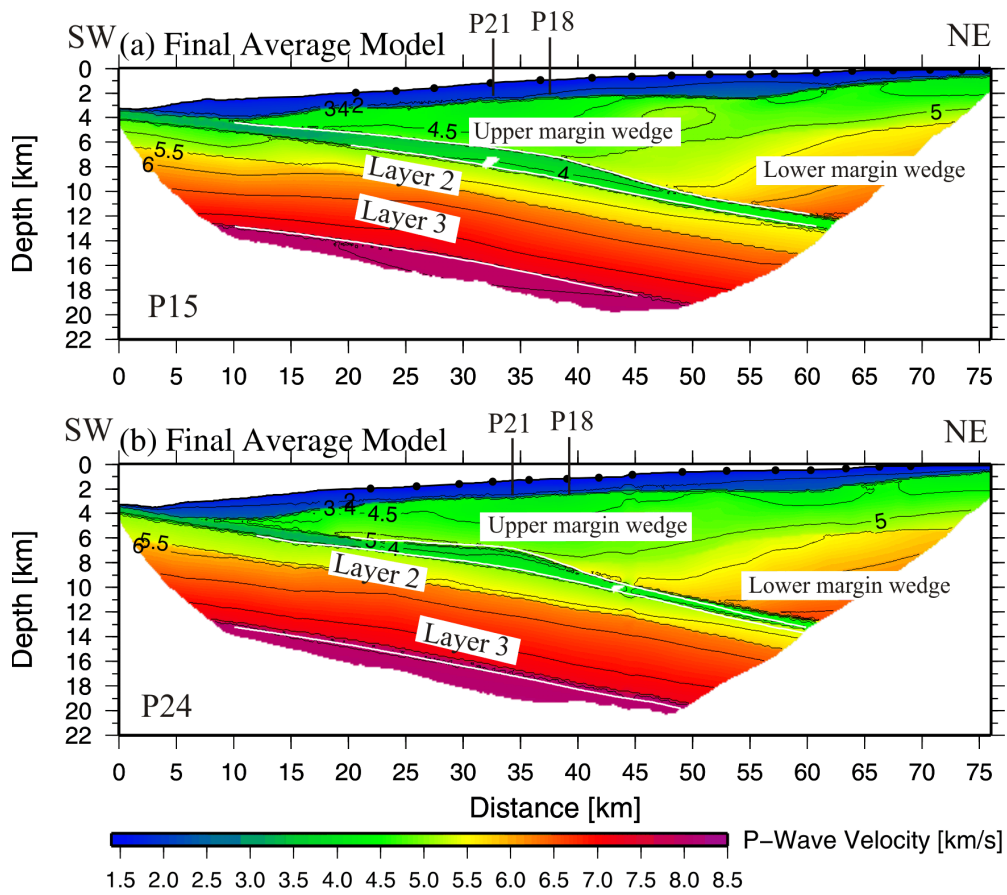


Fig 5.5. (a) Velocity-depth distributions for profiles P15 (a) and P24 (b). The velocity models for P15 and P24 were derived by averaging 100 Monte Carlo ensembles for each line. The corresponding standard deviation of velocity and depth nodes for profile P24 is shown in Figure 5.8. White lines mark reflectors. Contours are drawn at 0.5 km/s intervals.

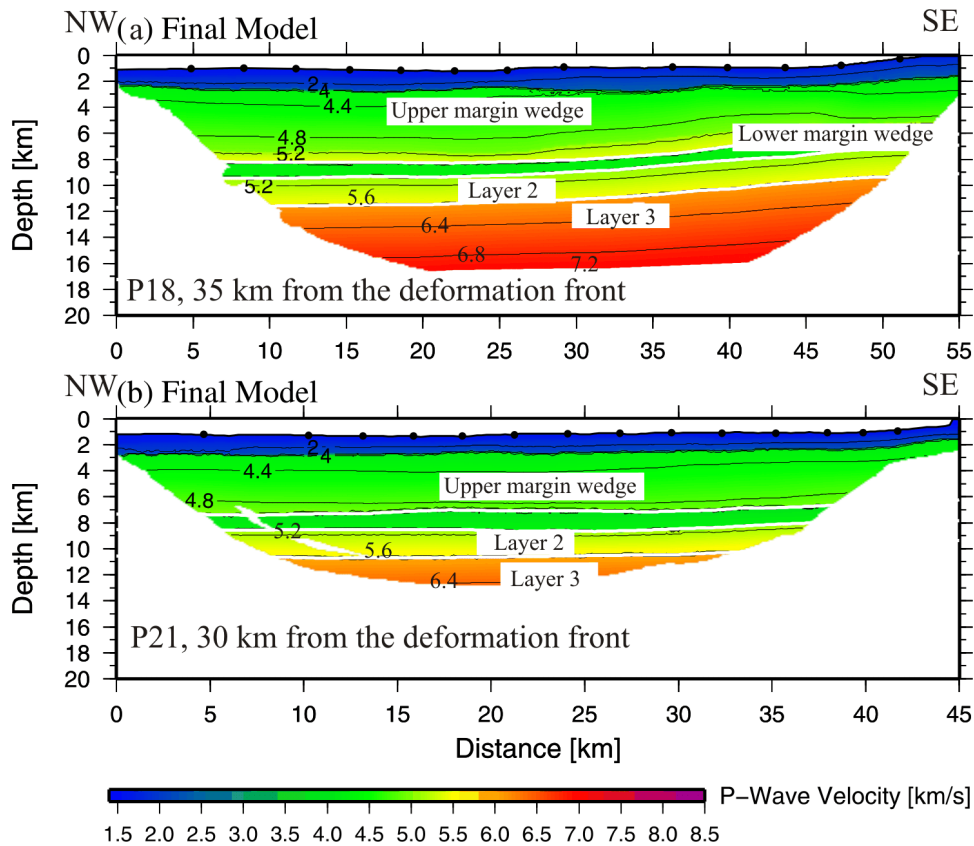


Fig 5.6. Velocity-depth distributions for profiles P18 (a) and P21 (b) derived by tomographic inversion. White lines show reflectors. Contours are drawn at 0.4 km/s intervals.

5.3.2.2 Model Uncertainty and Resolution Tests

Using the inversion scheme described in 3.1, we have to consider two inter-related issues:

- (1) The trade-off between depth and velocity parameters is linked to the reflected phase travel time inversion and depends on the source-receiver geometry. A conventional method to estimate the velocity-depth ambiguity is to perform sensitivity tests, such as checkerboard tests and Gaussian anomaly tests. In this procedure, different synthetic anomalies of various sizes are placed at specific positions in the models to assess at what point these anomalies are well resolved by the travel time inversion.
- (2) Uncertainty estimation in the velocity model, i.e. how well-resolved are the different parts of the model. This may be evaluated by estimating the

influence of the initial model upon the obtained solution, as well as by estimating uncertainties applying a Monte-Carlo analysis. The method involves a number of inversions with a variety of initial models using travel time picks with random errors applied. If all the Monte-Carlo realizations have the same probability and if the initial models cover the full region of non-null probability within the space of parameters, the standard deviation of the obtained solutions can be interpreted as a measure of the final model parameter uncertainty.

To address the first issue, we conducted a resolution test by calculating synthetic data for a perturbed velocity model with a source-receiver geometry identical to the experiment setup. The synthetic data are then inverted with the initial unperturbed model to analyze how well the given perturbations are recovered. The perturbed velocity model is constructed using the final average velocity model with $\pm 5\%$ Gaussian anomalies placed at different positions in the model (Fig. 7). After 6 iterations, the position, shape and amplitude of the velocity anomalies are well recovered within the margin wedge and adequately recovered along the model periphery (Fig. 7). The relative high velocities found at profile distances of 45-52 km at around 4 km depth on profile 15 (Fig. 5a) in the margin wedge are a robust feature of the inversion solution.

Additionally, a nonlinear Monte Carlo uncertainty analysis (Tarantola and Valette, 1982) was conducted to estimate the model uncertainty and dependence of the obtained solutions on the initial model as addressed by the second issue mentioned above. The nonlinear Monte Carlo uncertainty was estimated as a posteriori model covariance matrix (Tarantola, 1987), which can also be approximately expressed by the standard deviation of a number of Monte Carlo realizations (Korenaga et al., 2000). We constructed 100 Monte Carlo ensembles by inverting data with random errors with random initial velocity models (see Appendix). The 100 2-D initial velocity models were built by adding velocity values (randomly chosen between certain predefined limits) on a reference model beneath the basement. In addition, 100 noisy travel time data sets were constructed by adding random phase errors (± 50 ms) and common-receiver errors (± 50 ms) on the original data set (Zhang and Toksöz, 1998; Korenaga et al., 2000). Finally, each velocity model and corresponding reflector were inverted together with a noisy data set to estimate the influence of the starting model and the effect of realistic travel time errors. We used a top-bottom strategy to run the inversion step for each reflector, as described above. We added random velocities on the 2-D forward model of profile P24 including two floating reflectors

(top and base of the décollement zone, random variations within ± 1 km) at the plate interface and one reflector (Moho, random variations within ± 2 km) in the lower plate.

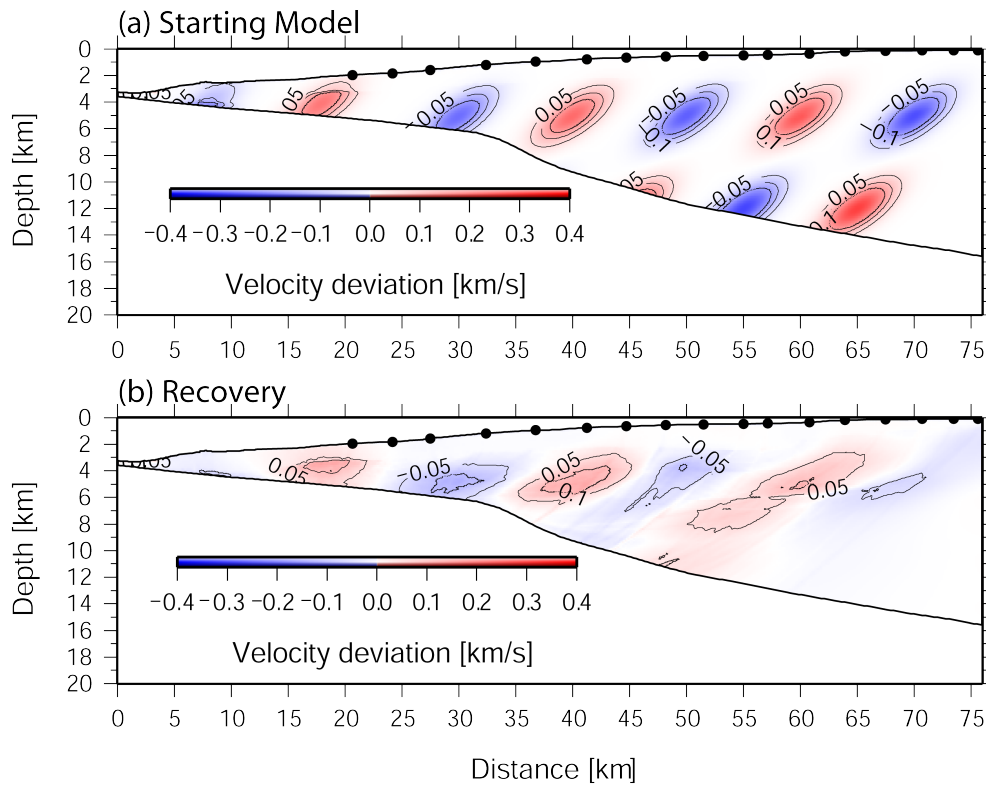


Fig 5.7. Upper plate resolution test for profile P15. (a) Velocity anomalies of $\pm 5\%$ in the synthetic model are given with respect to the initial velocity model. Velocity anomalies are applied to Gaussian anomalies rotated by 30 degrees. The source and receiver geometry used for synthetic travel time calculation is identical to the experiment layout. (b) Recovery obtained after 6 iterations.

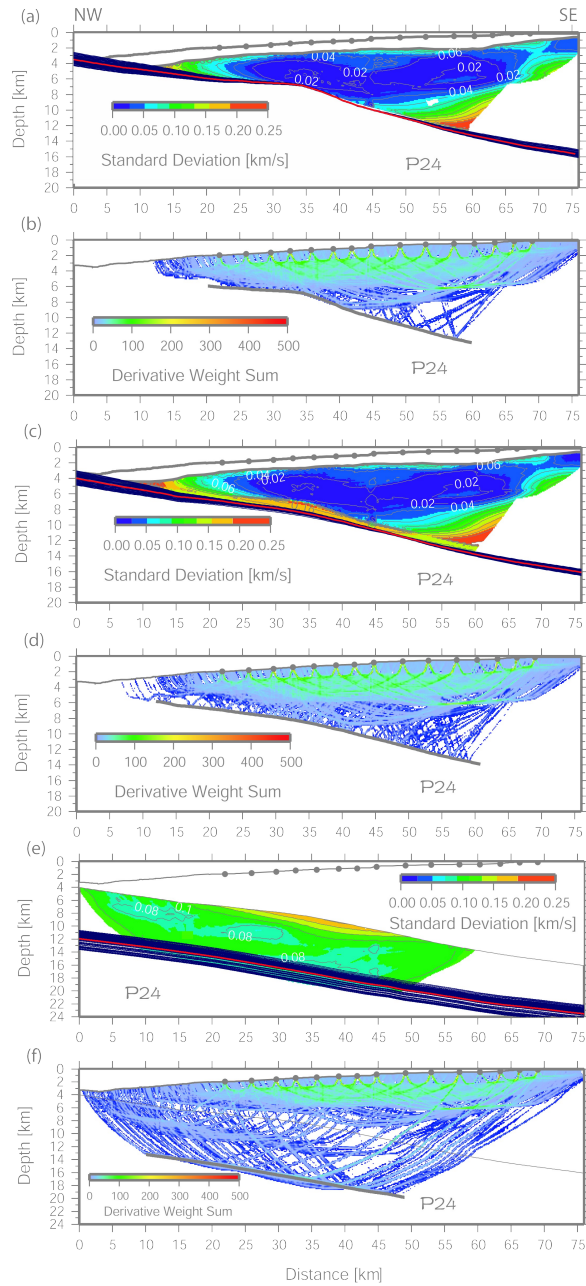


Fig 5.8. Standard deviations for velocity and reflector depth nodes of profile P24 derived from 100 Monte Carlo ensembles (a, c, e) and corresponding derivative weight sum from the average 100 realizations (b, d, f). Red lines show the average depth of reflectors and contours are drawn at 0.02 km/s intervals (a, c, e).

100 input models were tested for each reflector during 10 iterations each, thus reducing the travel time root-mean-square misfits from several hundred ms to about 70-90 ms. The average values and uncertainty of model parameters are obtained by

averaging all Monte Carlo solutions and computing the corresponding standard deviation. The resulting deviation for profile P24 is shown in Figure 8. Velocity uncertainties of the upper plate are usually lower than 0.15 km/s within the margin wedge (Fig. 8a, b). The largest velocity uncertainties occur within the low velocity décollement zone and reach 0.18 km/s here (Fig 8c). The depth uncertainties of the first and the second reflector reach about 500 m within the range of ray coverage. The velocity uncertainties within the subducting oceanic crust are comparable (0.06-0.15 km/s) (Fig. 8e, f). Uncertainties in Moho depth show values around ± 1.5 km.

5.4. Reflectivity method

In this study, the amplitude modeling was performed using the 1D reflectivity code of Sandmeier and Wenzel (1986). The one-dimensional waveform modeling was exclusively applied to strike profiles P18 and P21 because the structural heterogeneity of the two dip lines prohibits one-dimensional modeling based on the reflectivity method along these transects. The 1-D initial velocity-depth model was provided by the tomography results of strike-lines P18 and P21. The modeling procedure is a trial-and-error process in which we propose a model consisting of many plane homogeneous layers, each showing a distinct P wave velocity (V_p), S wave velocity (V_s), density (ρ), and P and S attenuation quality factors (Q_p and Q_s). Velocity gradients are approximated by a stack of layers with corresponding velocity contrasts. Calculated synthetic seismograms are compared with the observed seismograms, until an optimal fit is realized. For our amplitude modeling, we used a constant Poisson ratio of 0.28 and set $Q_p = 2Q_s$ (as used by Spudich and Orcutt, 1980; Christeson et al., 2000). A Q_p value of 300-500 for the crustal and sub-crustal environment is in agreement with earlier observations (Bowman, 1988). Densities were set to 1.5 g/cm^3 for the slope sediments and 1.8 g/cm^3 within the margin wedge (Kimura et al., 1997; Christeson et al., 2000). Densities for the oceanic crust were calculated using the relationship $\rho = 1.85 + 0.165V_p$ (Christensen et al., 1970; Christeson et al., 2000).

As the airgun source signature was unknown, we used a Fuchs-Mueller signal as input source wavelet. The source wavelet is defined by the equation given by Fuchs and Mueller (1971):

$$s(t) = \begin{cases} \sin \delta t - \frac{1}{m} \sin m \delta t & 0 \leq t \leq T \\ 0 & t < 0, t > T \end{cases}$$

Where

$$\delta = \frac{N\pi}{T}, \quad m = \frac{N+2}{N}.$$

N is an integer defining the number of extrema and T is the duration of the wavelet in seconds. For our synthetic seismogram, N=4 and T=0.4 s were used. The frequency content of the Fuchs-Mueller signal used here has corner frequencies of 1/3-18/24 Hz, to simulate the dominant frequencies of the airgun signal recorded in the seismic section. Peak amplitudes of the refracted phases through the margin wedge are picked in the seismic record sections and synthetic seismograms along the two strike lines. The direct wave is used as reference to calibrate the amplitude data while considering the geometry spreading factors.

5.4.1 Strike line P18 and line P21

In our data, frequencies of the refracted waves in the margin wedge mainly focus between 5 Hz and 15 Hz, e.g. for OBS 68 in Figure 9 (traces 200 to 330). Thus it is reasonable to use 12 Hz as the dominant frequency for the source signal during the amplitude modeling.

It is well known that the velocity gradient influences the amplitude of refracted phases (Banda et al., 1982). To verify the sensitivity of our analysis, we compare the amplitude behavior for varying velocity gradients for different Qp values (Fig. 10). We systematically vary the velocity gradient in the upper plate (margin wedge) according to the uncertainties obtained in 3.2.2 and then use the reflectivity method to calculate the synthetic seismograms and obtain the corresponding amplitude-distance curves (Fig. 10). The detailed model parameters are presented in Table 1. The resulting amplitude-distance curves show some variations in the near offset domain (offset < 10 km), but at larger offsets, no significant variation conditional to different velocity gradients is observed (Fig. 10, models m1Q50, m2Q50 and m3Q50). The variations at near offsets are likely mainly related to interference from reflection phases here. The velocity model m1 corresponds to the velocity distribution retrieved by the tomographic inversion as was thus chosen to test the effect of increasing Qp values (Qp of 50, 75, 100, 150, 200) on the amplitudes (Fig. 10, Table 1). The resulting curves in Figure 10 show a relative sensitivity to the analyzed Qp range.

Consequently, we assume that the velocity gradient has a relatively minor influence on our investigation (especially at offset > 10 km), which is expressed within the general uncertainty (Fig. 10).

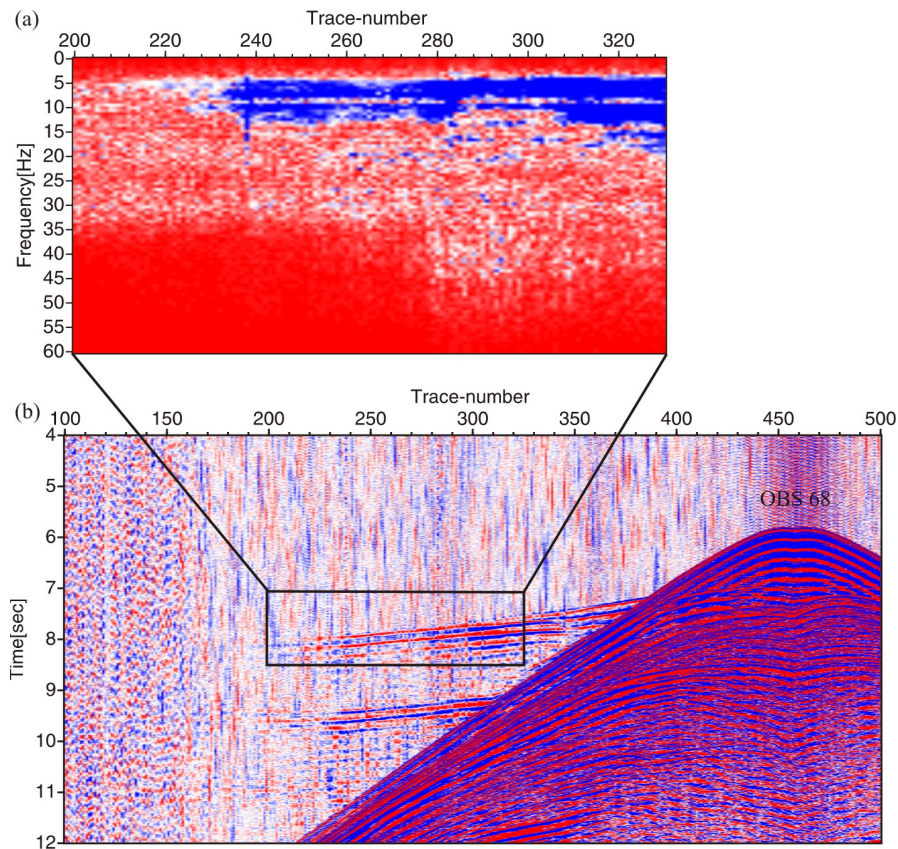


Figure 5.9. Frequency spectrum of OBS 68. (a) Trace numbers from 200 to 330, (b) time domain data of OBS 68. The square area shows the time window from 7 s to 8.5 s used for the frequency spectrum.

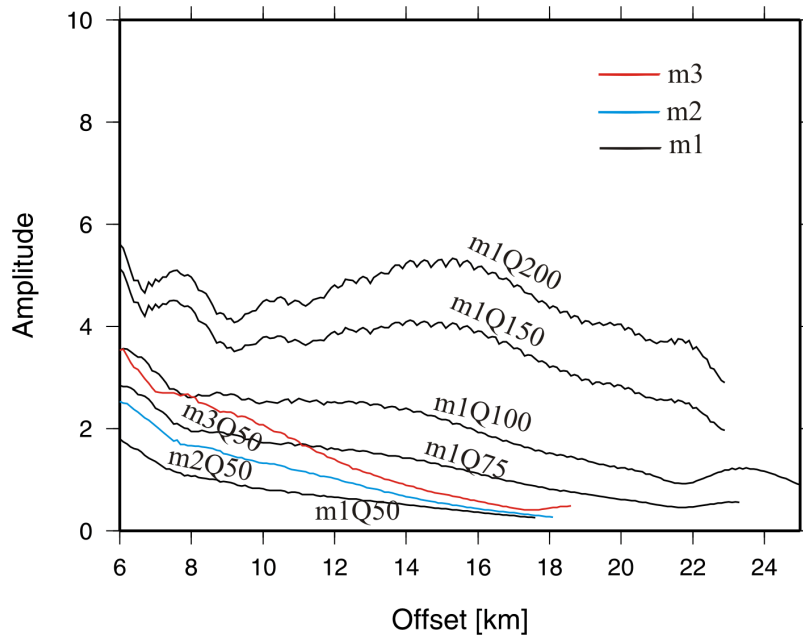


Figure 5.10. Amplitude-distance curves for models m1, m2, and m3 (different positive velocity gradients, see Table 1 for model parameters). Amplitude-distance curves of m1 model with different Q_p values are displayed.

Table 5.1. Model parameters

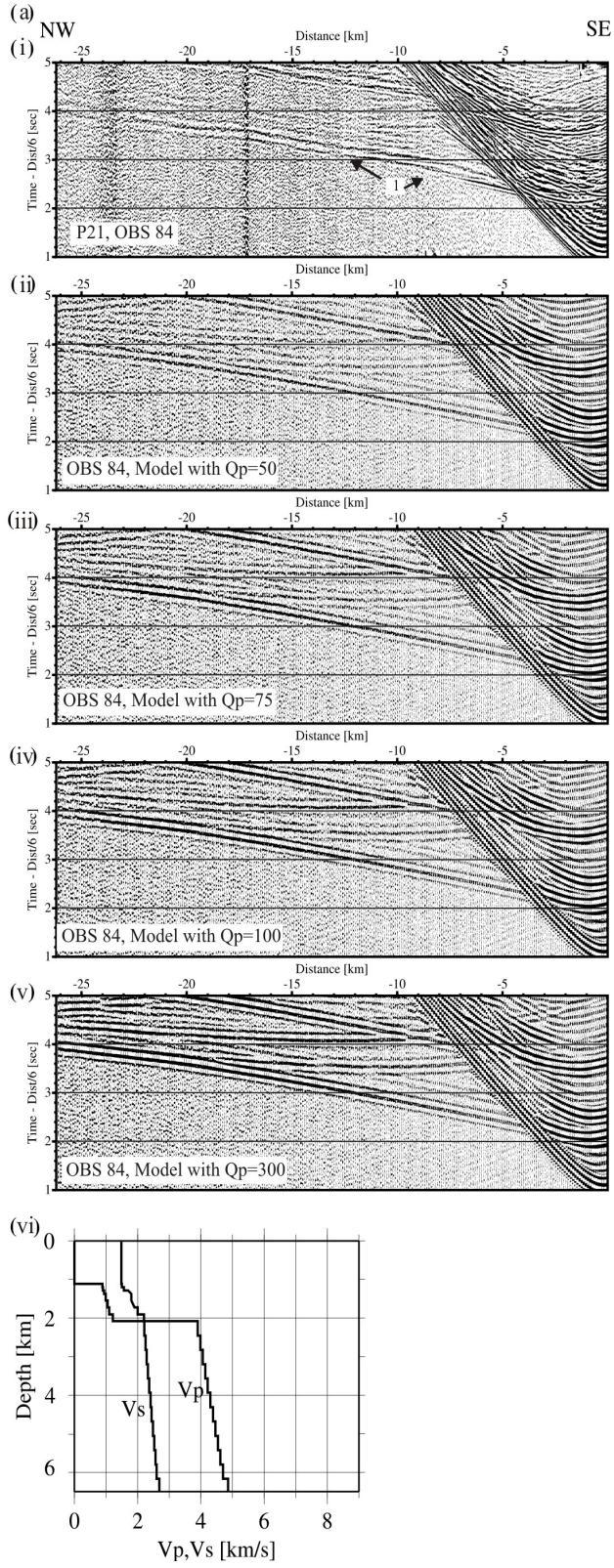
Model	thickness of margin wedge (km)	V_p (km/s)	velocity gradients of layers (km/s/km)
m1	4.46	4.0-4.8	0.18
m2	4.46	3.8-4.8	0.224
m3	4.46	3.9-5.2	0.269

Two record sections along the strike lines P18 and P21 are shown in Figure 11. The locations of OBS 84 and OBH 67 are indicated in Figure 1. The primary travel time characteristic of the record section is interpreted as refracted arrivals through the margin wedge. First arrivals document both the velocities and Q_p within

the margin wedge and are clearly reproduced in the synthetic seismograms (Fig. 11a-b). We calculated synthetic seismograms using different attenuation ($1/Q_p$) values and various vertical velocity gradients to test their effect on the seismic wave field. For OBS 84 displayed in Figure 11a, the velocity-depth function of P21 (Fig. 11a, in panel vi) represents the margin wedge velocity, which is modestly slower (0.2-0.3 km/s) than the corresponding function determined by ray-tracing (Fig. 6b) without including the effect of attenuation. Figure 11b displays the original record section and synthetic seismograms calculated for OBH 67 of strike line P18. The primary arrivals through the upper margin wedge are focused between offsets 5-25 km (Fig. 11b). Again, synthetic seismograms are displayed for the different Q_p values. For both profiles, it is difficult to define the proper Q_p values from the synthetic seismograms, but a Q_p of 300 yields unrealistically high amplitudes in the margin wedge compared to the real data (panels v in Fig. 11a, b). A quantitative estimation of Q_p values is required as introduced below.

5.4.2 Quantitative estimations of Q_p values

In order to estimate the Q_p values of the upper plate in a quantitative manner, we analyse amplitude variations of first arrivals from the margin wedge. The amplitude-offset decay curve is used as a criterion to assess the validity of different Q_p models by comparing the amplitude characteristics of the observed data and synthetic models. The peak amplitude values of the refracted phase from the margin wedge are picked manually using the Hampson-Russell software. This method is applied to the record sections indicated in Figure 1. A prerequisite of this approach is the calibration of amplitudes, usually with reference to the direct/water wave. The peak amplitudes of the direct wave from the synthetic seismograms and real data are matched firstly by applying geometric spreading corrections, and are then applied to the refracted phase. The relative amplitude curves are presented in Figure 12. The amplitudes of the synthetic data decrease fairly smoothly with distance, whereas the recorded data show a rougher variation mainly caused by the complexity of the subsurface generating signal interference compared to the smooth phase of the synthetic model. The lower signal-to-noise ration of the recorded data will enhance this scattering. In addition, although the tomographic images for lines P18 and P21 suggest a fairly smooth structure, the recorded data obviously are not one-dimensional and thus will to some degree violate the most important prerequisite for amplitude modeling. For this reason we conducted the modeling for two profiles at a distance of only approximately 5 km from each other to circumnavigate possible 3-D effects and minimize the effect statistically. For OBS 84, OBH 89, and OBH 90 of strike line



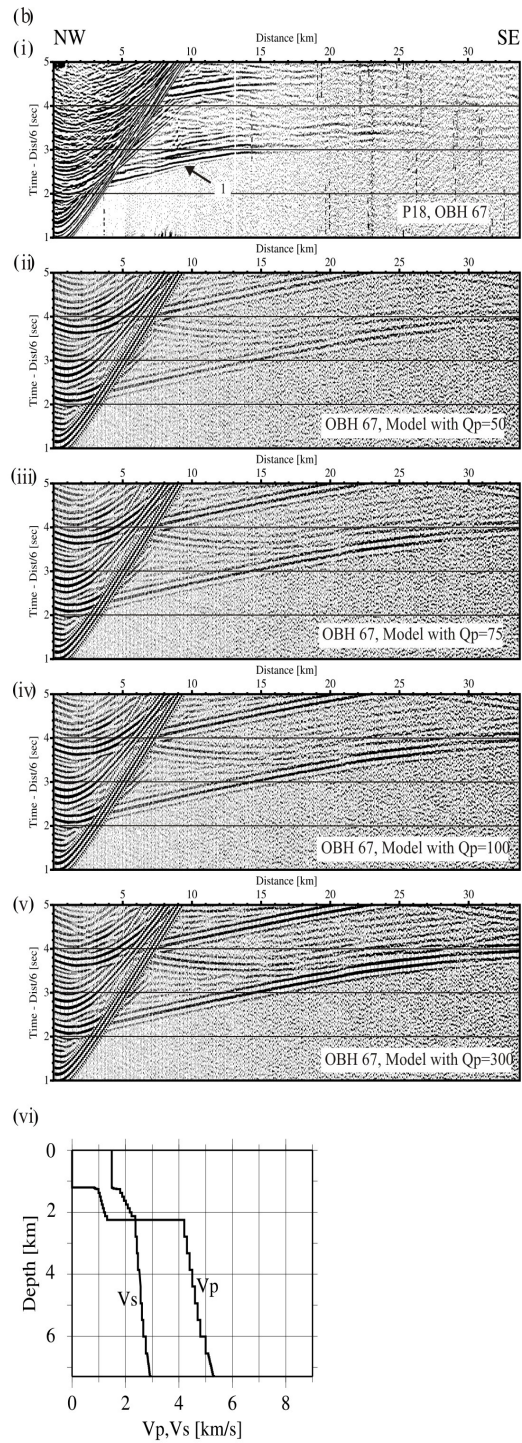


Figure 5.11. Record section and synthetic seismograms of strike line P18 and P21. Ambient noise has been added to the synthetic record sections. Increasing Q_p values of 50, 75, 100, and 300 within the margin wedge are shown in panels ii-v. The velocity-depth function is shown in panel vi. (a) OBS 84, (b) OBH 67

P21, a Q_p value of 50-150 generates comparable amplitudes between the observed and synthetic data (Fig. 12a-c). On average and for offsets greater than 10 km, the amplitude-distance curves of these record sections trend along the $Q_p=75$ synthetic curve. For OBS 68, OBH 71, and OBS 74 of strike line P18, a Q_p value of 50-150 best produces similar amplitude characteristics between the observed and synthetic data (Fig. 12d-f).

5.4.3 Uncertainty estimations of the seismic attenuation

The forward amplitude modeling conducted for the two strike lines returns modest Q_p values of 50-150, which correlate with the observed wavefield and amplitude-distance curves along profiles P18 and P21. Higher Q_p values (> 200) in the margin wedge will generate high peak amplitude values at the related offset (Fig. 12) and will not reproduce a comparable amplitude behavior between the observed and synthetic data. A similar pattern is observed for all stations modeled on the two strike lines, where overestimated Q_p values generate artificially high amplitude arrivals. The less homogeneous velocity distribution and structure of line P18 as discussed in 3.2.1 leads to a higher degree of scattering in the amplitude-distance curves of OBS 68, OBH 71, and OBS 74 (Fig. 12), however, the general trend of all curves on average won't exceed Q_p values of 200.

In addition to the upper plate Q_p values, other factors affecting the modeled amplitude pattern include the vertical velocity gradient of the margin wedge as discussed in 4.1. A high velocity gradient in the margin wedge (e.g. m3 model, velocity gradient of 0.269/s, Table 1) generates relative high amplitudes at corresponding offsets with an identical Q_p of 50. Therefore, high vertical velocity gradients will lead to an underestimation of Q_p values. The amplitude of the refracted phase can be decreased by either a decrease in the vertical velocity gradient or a decrease in the margin wedge Q_p values. In order not to overestimate upper plate Q_p values, we chose a vertical velocity gradient of 0.18/s (m1 model, Table 1) for the margin wedge consistent with the result of the tomographic inversion, yielding a minimum Q_p value here (Fig. 12).

For station OBS 84 and OBH 90 of profile P21 (Fig. 12a, c), the amplitude-distance curves at offsets greater than 14 km closely correlate with the $Q_p=75$ curve. Scattering is higher at the near offsets, which are more affected by the larger variation

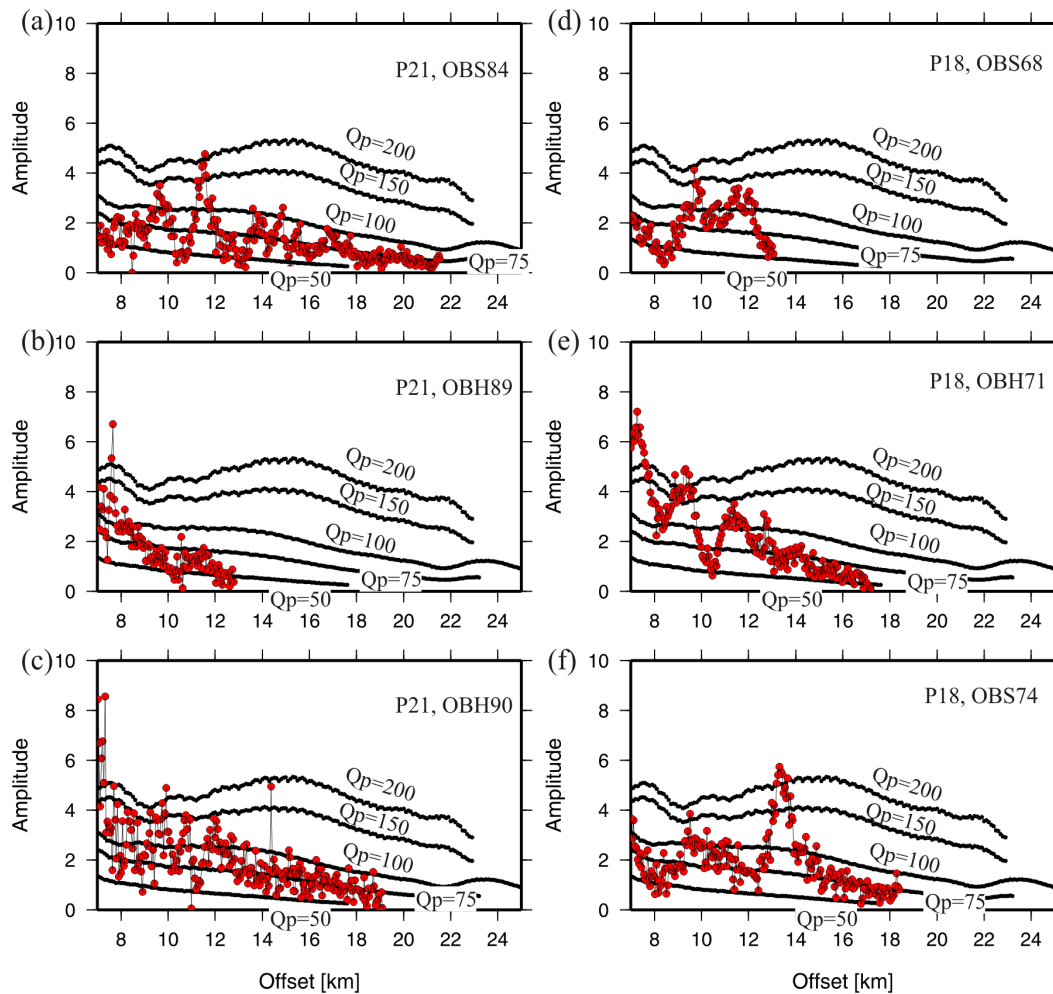


Figure 5.12. Amplitude versus offset variations for refracted phases through the margin wedge of stations OBS 84, OBH 89, OBH 90 along strike line P21, and OBS 68, OBH 71 and OBS 74 along the strike line P18. Red dotted lines show the amplitude decay curves of the record sections. Black lines show a constant Q_p of 50, 75, 100, 150, and 200 in the margin wedge.

of physical properties in the sedimentary cover as well as be interference of sediment reflections. This effect is also observed for station OBH 89 of the same line (Fig. 12b), however amplitudes could only be picked up to an offset of 13 km, impeding the analysis. Even more difficult to analyze due to the lack of far offset amplitude values are the data of OBS 68 of profile P18 (Fig. 12d). As for OBH 89, the low signal-to-noise ratio of this station inhibited exact amplitude picking at offset > 13 km. Both stations, however, seem to follow the general trend not to exceed Q_p values of 200. For OBH 71 (Fig. 12e), the slope of the amplitude-distance curve does not

match the synthetic values. This is associated with the velocity gradient and comparison with curve m3Q50 of Figures 10 implies that the velocity gradient is not matched underneath this station. As discussed in 4.1, the gradient will influence the slope of the curve but is less sensitive to the relative amplitude values. The data of OBS 74 (Fig. 12f) mainly trend around $Q_p=75$ and show a decisive maximum at 12-14 km offset. We interpret this peak to be caused by a low signal-to-noise ratio in the original data and thus to be artificial.

5.5. Discussion

The results of the tomographic inversion reveal more details of the seismic structure in the model space compared to the forward modeling results (Zhu et al., 2009). The fine shear mesh of velocity nodes of the velocity field indicates the P-wave velocity variation from 4.0-4.5 km/s at the tip of the margin to 4.1-6.5 km/s near the coast (Fig. 5). The thickness of the margin wedge increases at the trench axis from several hundred meters to about of 15 km at the coast (Fig. 5). Similar structural units as observed here (upper and lower margin wedge) are also resolved along the north Ecuador-south Colombia margin (Agudelo et al., 2009), where a significant accretionary wedge is missing.

The décollement zone is imaged as a 1-1.5 km thick low velocity zone sandwiched between the margin wedge basement and the subducting Cocos plate. The velocity model of dip lines P15 reveals a zonation of the décollement zone with velocities rapidly increasing from 3.0 km/s to 3.5 km/s from the deformation front over a distance of 15 km (P15). Velocities then remain constant (~ 3.5 -3.6 km/s between 20 and 35 km offset) until they increase again underneath the lower margin wedge (~ 4.2 km/s at 50 km offset) (this velocity increase is not unambiguously resolved for P24). A similar velocity pattern of the underthrust material has also been reported for the erosional south Ecuadorian margin (Calahorrano et al., 2008), where a clear segmentation of the décollement zone could be inferred from pre-stack depth migrated multichannel seismic data. The progressively increasing seismic velocities concur with a reduction in porosity resulting from sediment compaction associated with fluid drainage.

The amplitude of a refracted seismic wave is controlled by the velocity of the medium through which it propagates as well as by the anelastic attenuation characteristics of the medium. The degree of cracking and water or gas in fractures will directly influence seismic attenuation by reducing Q_p values (Bourbié et al.,

1987). This is consistent with the observation that Q_p values generally increase with depth in the oceanic crust, which is attributed to the decrease in fracturing and structural heterogeneity (Wilcock et al., 1995).

In Costa Rica, previous studies have reported high attenuation ($Q_p=25-50$) approximately 10 km landward of the deformation front offshore Nicoya Peninsula (about 210 km northwest of our study area) (Christeson et al., 2000). These values are consistent with the low Q_p values from marine sediment ($Q_p= 25-30$) (Hamilton, 1972) and reflect the sedimentary composition of the highly tectonized frontal prism. This frontal prism is present along the entire ~500 km Costa Rican margin (von Huene et al., 2009) and is self-limiting in size, which is a function of material supply, convergence rate and taper. The width of the frontal prism off Costa Rica does not exceed 15 km landward of the deformation front. Approximately 20 km from the deformation front, Christeson et al. (2000) observe Q_p values of 50-75, which is only slightly lower than our results from strike lines P21 and P18, located 30 km and 35 km from the trench, respectively (Fig. 5). The lower attenuation of our lines ($Q_p = 50-150$) compared to the values ($Q_p=25-50$) recorded on the frontal prism (Christeson et al., 2000, Table 2) reflect the tectonically more stable domain of the middle prism and a change in lithology. The values are consistent with a Nicoya complex composition of the central Costa Rican margin wedge. The Nicoya complex is exposed on Nicoya Peninsula as ophiolitic rocks, composed of massive flows, pillows, dikes, basaltic breccias, gabbros, plagiogranites and radiolarian chert (Kuijpers, 1980). This unit has been interpreted as the seaward extent (Ye et al., 1996; Christeson et al., 1999) of the Caribbean Cretaceous oceanic plateau (Bowland et al., 1988; Sinton et al., 1997). Though attenuation across the middle prism decreases relative to the frontal prism, Q_p values remain comparatively low. This may be associated to the fracturing of the middle prism, which has been documented in numerous studies. Faults penetrate deep into the slope sediment and into the basement rock (McIntosh et al., 1993; Hinz et al., 1996; Ranero and von Huene, 2000). Seismic attenuation is influenced by the material composition, which is reflected in the Q_p structure of the margin wedge. The increase in Q_p values from the frontal prism, to the middle and inner prism allow assessment of the changes in lithology. The overall relative low Q_p may be related to the fluid budget of the margin as expressed in fluid expulsion through mud volcanoes distributed along the margin wedge. The fault pattern is intrinsically related to the hydrogeological system of the margin where the majority of focused fluid seepage occurs on the middle slope (Ranero et al., 2008). Fluid flow constitutes one cause of attenuation, however, only at frequencies below the frequency range of our study (Toksöz et al., 1987).

Table 5.2. Margin wedge velocities and Qp values from wide-angle strike lines

Region	Costa Rica, Nicoya Peninsula		Central Costa Rica	
	10 km	20 km	30 km	35 km
Distances from trench	10 km	20 km	30 km	35 km
Velocity ranges (km/s)	4-4.4	4.4-4.8	3.9-4.9	4.2-5.0 (upper margin wedge) 5.1-5.4 (lower margin wedge)
Thickness of the margin wedge (km)	1.5	3.0	4-4.5	3.5-5 (upper margin wedge) 1-1.5 (lower margin wedge)
Qp	25-50	50-75	50-150	50-150
Reference	Christeson et al., 2000		this study	

5.6. Conclusions

We apply the reflectivity method and incorporate the Q parameter to obtain a 1D model for Qp on the Costa Rican margin wedge (Table 2). By comparison with previous studies (Christeson et al., 2000) we document a lateral decrease of attenuation across the margin wedge with distance from the trench, implying physical and lithologic variations along the lower slope of the marine forearc. This is related to material strength variations associated with a change in lithology from the sediment-dominated frontal prism to the igneous composition of the middle prism of the forearc. Seismic velocities and Qp values of the margin wedge are consistent with a high degree of fracturing as suggested by previous studies (Ranero et al., 2008), which facilitates mass wasting and subduction erosion processes.

Chapter 6

Conclusions and Outlook

Convergent margins are among the tectonically most dynamic regions on earth due to the plate movement and material transfer (erosion, accretion) processes occurring at subduction zones. The Central American continental margin offshore Costa Rica has been a focus of geoscientific research because it provides a spectrum of different subduction styles and scenarios, manifested in the nature of the subducted oceanic crusts, the seismicity pattern and subducted topography. A unifying model of margin tectonics and evolution requires an understanding of the relationship between the different parameters involved. This study contributes towards this goal by supplying a detailed structural and seismic velocity model derived from seismic methods.

Material transfer in a subduction zone involves erosive and accretionary processes, which may occur simultaneously at a single margin or margin segment. At the surface, gravitational mass wasting processes transport slope sediment downslope. This material is partially subducted, partially accreted into a frontal prism. A portion of the subducted and remobilized material is partly returned to the exosphere and partly subducted into the lower mantle. The complex mechanisms of material transfer play a crucial role in the evolution of the margin and have an influence on the nature of the rock units in the overriding upper plate. A verification of the concepts of the origin and the structure of the offshore rock bodies requires detailed knowledge of their velocity-depth characteristics. The modeling and interpretation of the seismic wide-angle data, presented in this thesis, combined with coincident seismic reflection data and amplitude modeling, have enabled us to construct a detailed velocity-depth model covering the Pacific margin off central Costa Rica. The data clearly define two layers within the margin wedge, the high velocity gradient upper margin wedge with velocities of 4.3-5.0 km/s and the reduced velocity gradient lower margin wedge with velocities ranging from 5.2-6.1 km/s. Near the deformation front, a frontal prism characterized by low seismic velocities typical of sediment does not exceed a lateral width of 15 km. Our results thus reveal the basic structural configuration and segmentation of the forearc. One of the so-called 'megalens', which was not

unambiguously revealed by previous work. The leading edge of the lower margin wedge terminates above the ‘megalens’ about 32 km landward of the trench. The two strike-lines confirm the seaward termination of the lower margin wedge. The ‘megalens’ is 15-20 km wide and has a thickness of 1-1.5 km. Its seismic velocities fall between 3.8 km/s and 4.3 km/s and are clearly much lower than the velocities of subducted seamounts or plateaus. The ‘megalens’ is a low velocity body with respect to the margin wedge above and is bounded by thin layers of lower velocities above and below. Our preferred interpretation is that the ‘megalens’ is a mixture product, which consists of a buried sedimentary *mélange* including rocks sheared from the lower plate and highly fractured material derived from the upper plate by basal erosion. The LVZ above the ‘megalens’ shows a discontinuous amplitude distribution in the seismic image caused by fluids and associated localized pore pressure anomalies.

In order to quantify the margin structure, we apply the reflectivity method and incorporate the Q parameter to obtain the Qp variations across the Costa Rica margin wedge. We retrieve a 1D model for Qp across the margin, which provides some information to support the physical and lithologic variations along the lower slope of the marine forearc. By comparison with previous studies (Christeson et al., 2000) we obtain a systematic lateral decrease of attenuation across the margin wedge with distance from the trench. This is related to material strength variations associated with a change in lithology from the sediment-dominated frontal prism to the igneous composition of the middle prism of the forearc. Seismic velocities and Qp values of the margin wedge are consistent with a high degree of fracturing as suggested by previous studies (Ranero et al., 2008), which facilitates the mass wasting and subduction erosion processes.

Outlook

Convergent margins are classified into two pure end-members with accreting or eroding modes of mass transfer in the present literature. A rapid convergence rate enhances the efficiency of sediment subduction and subduction erosion along continental margins (von Huene et al., 2009) as, for example, the rapid convergence rate ($84 \pm 5 \text{ mm yr}^{-1}$) of the Costa Rica subduction zone (DeMets, 2001). Although in this study the detailed velocity structure of the central Costa Rica margin is well constrained, the dynamic evolution of the convergent margin is still vague. The subduction channel model needs to be refined in Costa Rica to extract physical properties (porosity, fluid or effective pressure) such as has been achieved for the

southern Ecuador margin (Calahorrano et al., 2008). However, in Costa Rica it is not easy to support the concept of subduction channel zonation associated with nonlinear variation of physical properties without high-resolution seismic data and ideally corresponding drilling information. This concept thus remains open for further surveying here.

Acknowledgments

I am grateful to the German Academic Exchange Service (Deutscher Akademischer Austausch Dienst - DAAD), which provided me financial support to finish my Ph.D study at IFM-GEOMAR.

I would like to thank Prof. Heidrun Kopp for her continuous support and giant patience to revise my paper, and numerous discussions with her over the past years. She provided me some good ideas and constructed suggestions, especially for reasonable scientific thinking.

I would like to also thank Prof. Ernst Flueh for his patience guiding, especially for important aspect of seismic modeling during my whole time at IFM-GEOMAR. I am very lucky to work with him during one cruise in Auckland. His serious-minded and strong organizations have deeply influenced on me. Many thanks to him for supporting my work.

Dr. D. Klaeschen and C. Papenberg provided me much help to use SEISMOS and Hampson Russell program for amplitude modeling.

Lars Planert and Alexy Shulgin gave me much help for Tomography inversion. Andreas Wittwer and Anne Krabbenhoeft helped me to use the classical forward ray tracing tool (MacRay).

I am very thankful to Mrs. Heike Schaedlich for her numerous help after I obtained a DAAD scholarship.

I am grateful to all colleagues and participants of Cruise SO163 for their help with data acquisition, particularly to the skillful crew of the RV Sonne. Data acquisition was supported by the BMBF.

Many thanks to all members of the FB4 and SFB 574 for very interesting and helpful discussions. Best thanks to my colleague and friends: Martin Schwarth, Jin Chen, Markus Fink, Wolfgang Weinzerl, David Pesquer, Anke Dannowski who let me feel at home over the past years in Kiel.

Finally, I want to thank my family, especially my wife Rongrong Zhang for her encouragement and supporting. She is not only my partner but also my listening of my scientific work in Kiel. She was always to support me when I was happy or not.

Bibliography

1. Abratis, M., Wörner, G., 2001. Ridge collision, slab-window formation, and the flux of Pacific asthenosphere into the Caribbean realm. *Geology*, 29, 127–130.
2. Adam, J., and Reuther, C.-D., 2000. Crustal dynamics and active fault mechanics during subduction erosion: Application of frictional wedge analysis to the north Chilean forearc: *Tectonophysics*, 321, 297–325.
3. Azéma, J., Bourgois, J., Baumgartner, P. O., Tournon, J., Desmet, A., & Aubouin, J., 1985. A tectonic cross-section of the Costa Rican Pacific littoral as a key to the structure of the landward slope of the Middle America Trench off Guatemala, in *Init. Rep. DSDP84*, pp. 831-850, edited by von Huene, R., Aubouin, J., et al., U.S. Gov. Print. Off., Washington, D.C.
4. Banda, E., Deichmann, N., Braile, L. W., and Ansorge, J., 1982. Amplitude study of the Pg phase, *J. Geophys.*, 51, 153-164.
5. Bangs, N., Shipley, T. H., Gulik, S., Moore, G. F., Kuromoto, S., Evolution of the Nankai Trough decollement from the trench into the seismogenic zone: Inference from the dimensional seismic reflection imaging, *Geology*, 32(4), 273-276, 2004.
6. Barckhausen, U., Roeser, H., von Huene, R., 1998. Magnetic signature of upper plate structures and subducting seamounts at the convergent margin off Costa Rica, *J. geophys. Res.*, 103, 7079-7093.
7. Barckhausen, U., Ranero, C. R., von Huene, R., Cande, S. C., & Roeser, H., 2001. Revised tectonic boundaries in the Cocos Plate off Costa Rica: Implication for the segmentation of the convergent margin and for plate tectonic models, *J. geophys. Res.*, 106, 19207-19220.
8. Berrange, J. P., Thopre, R. S., 1988. The geology, geochemistry and emplacement of the Cretaceous-Tertiary ophiolitic Nicoya Complex of the Osa Peninsula, southern Costa Rica, *Tectonophysics*, 147, 193-220.
9. Behrmann, J. H., 1991. Conditions for hydrofracture and the fluid permeability of

accretionary wedges, *Earth Planet. Sci. Lett.*, 107, 550–558.

10. Bialas, J., & Flueh, E. R., 1999. Ocean bottom seismometers, *Sea Technology*, 40(4), 41-46.

11. Bird, P., 2003. An updated digital model of plate boundaries, *Geochem. Geophys. Geosyst.*, 4(3), 1027, doi:10.1029/2001GC000252.

12. Bishop, T.N., K.P. Bube, R.T. Cutler, R.T. Langan, P.L. Love, J.R. Resnick, R.T. Shuey, D.A. Spindler, and H.W. Wyld, 1985. Tomographic determination of velocity and depth in laterally varying media, *Geophysics*, 50, 903-923.

13. Bourbié, T., Coussy, O., and Zinszner, B., 1987. Acoustics of porous media, Gulf Publ. Co., Houston, Tex.

14. Bowland, C. L., Rosencrantz, E., 1988. Upper crustal structure of the western Colombian basin, Caribbean sea, *Geol. Soc. Am. Bull*, 100, 534-546.

15. Bowman, J. R., 1988. Body wave attenuation in the Tonga subduction zone, *J. geophys. Res.*, 93(B3), 2125-2139.

16. Braile, L. W., and Smith, R. B, 1975. Guide to the interpretation of crustal refraction profiles, *Geophys. J. R. astr. Soc*, 40, 145-176.

17. Bundschuh, J., Winograd, M., Day, M., and Alvarado, G., 2007. Geographical, social, economic, and environmental framework and development. In Bundschuh, J. and Alvarado, G., editors, *Central America: Geology, Resources and Hazards*, pp. 1–52. Taylor & Francis.

18. Carr, M. J., 1984, Symmetrical and segmented variation of physical and geochemical characteristics of the Central American volcanic front. *J. Volcanol. Geotherm. Res.*, 20, 231-252.

19. Cerveny V, Molotkov I, Psencik I., 1977. Ray Method in Seismology. University of Karlova, Prague, Czechoslovakia

20. Christensen, N. I., & Shaw, G. H., 1970. Elasticity of mafic rocks from the Mid-

Atlantic Ridge, *Geophys. J. R. astr. Soc.*, 20, 271-284.

21. Christeson, G. L., McIntosh, K. D., Shipley, T. H., Flueh, E. R., & Goedde, H., 1999. Structure of the Costa Rica convergent margin, offshore Nicoya Peninsula, *J. geophys. Res.*, 104, 25443-25468.

22. Christeson, G. L., McIntosh, K. D., & Shipley, T. H., 2000. Seismic attenuation in the Costa Rica margin wedge: amplitude modeling of ocean bottom hydrophone data, *Earth planet. Sci. Lett.*, 179, 391-405.

23. Clift, P., & Vannucchi, P., 2004. Controls on tectonic accretion versus erosion in subduction zones: Implications for the origin and recycling of the continental crust, *Rev. Geophys.*, 42, RG2001, doi: 10.1029/2003RG000127.

24. Cloos, M., and Shreve, R. L., 1988a. Subduction-channel model of prism accretion, melange formation, sediment subduction, and subduction erosion at convergent plate margins: 1. Background and description. *Pure and Applied Geophysics*, 128:3-4, 455-500.

25. Cloos, M., and Shreve, R. L., 1988b. Subduction-channel model of prism accretion, melange formation, sediment subduction, and subduction erosion at convergent plate margins; Part . Implication and discussion. *Pure and Applied Geophysics*, 128:3-4, 501-545.

26. Collot, J.-Y., W. Agudelo, A. Ribodetti, and B. Marcaillou (2008), Origin of a crustal splay fault and its relation to the seismogenic zone and underplating at the erosional north Ecuador-south Colombia oceanic margin, *J. Geophys. Res.*, 113, B12102, doi:10.1029/2008JB005691.

27. De Boer, J. Z., Drummond, M. S., Bordelon, M. J., Defant, M. J., Bellon, H., Maury, R. C., 1995. Cenozoic magmatic phases of the Costa Rican island arc (Cordillera de Talamanca). In: Mann, P. (Ed.), *Geologic and Tectonic Development of the Caribbean Plate Boundary in Southern Central America*. Spec. Pap.-Geol. Soc. Am. 295, pp. 35– 55.

28. DeMets, C., Gordon, R. G., Argus, D. F., & Stein, S., 1990. Current plate motions, *Geophys. J. Int*, 101,425-478.

29. DeMets, C., Gordon, R. G., Argus, D. F., & Stein, S., 1994. Effect of recent revisions to the geomagnetic reversal time scale on estimates of current plate motions, *Geophys. Res. Lett.*, 21(20), 2191-2194.
30. DeMets, C., 2001. A new estimate for present-day Cocos-Caribbean plate motion: Implications for slip along the central American volcanic arc. *Geophys. Res. Lett.*, 28(21), 4043-4046.
31. Dengo, G., Mid America: Tectonic setting for the Pacific margin from southern Mexico to northwestern Columbia. In Nairn, A. E. M., Stechli, F. G., (eds.). 1985. The ocean basins and margins. New York, Plenum Press, 7, 123-180.
32. Dominguez, S., Lallemand, S. E., Malavieille, J., von Huene, R., 1998. Upper plate deformation associated with seamount subduction, *Tectonophysics*, 293, 207-224.
33. Dijkstra, E. W., 1959. A note on two problems in connection with graphs, *Numer. Math.*, 1, 269-271.
34. Dinc, A. N., Koulakov, I., Thorwart, M., Rabbel, W., Flueh, E. R., Arroyo, I., Taylor, W., & Alvarado, G., 2007. Local earthquake tomography of Central Costa Rica: Transition from seamount to ridge subduction, *Geophys. J. Int.*, (submitted).
35. Escalante, G., 1990. The geology of southern Central America and western Colombia. In: G. Dengo and J. E. Case (eds): *The Geology of North America*, vol. H, *the Caribbean Region*. Geological Society of America, Boulder, pp. 201-230.
36. Fisher, Robert L., 1961. Middle America Trench: Topography and structure. *Geol. Soc. Am. Bull.*, 72, 703-720.
37. Flueh, E. R., & Bialas, J., 1996. A digital, high data capacity ocean bottom recorder for seismic investigations, *Int. Underwater Syst. Design*, 18(3), 18-20.
38. Flueh, E. R., Ranero, C. R., von Huene, R., 1999. The Costa Rica Pacific margin: from accretion to erosion. *Zbl. Geol. Paläont.*, 7/8, 669-678.

39. Flueh, E. R. and von Huene, R., 2007. Crustal structure. In Bunddchuh, J. and Alvarado, G., editors, *Central America: Geology, Resources and Hazards*, pp. 267–274. Taylor & Francis.
40. Fuchs, K., & Mueller, G., 1971. Computation of synthetic seismograms with the reflectivity method and comparison with observation, *Geophys. J. R. astr. Soc.*, 23, 417-433.
41. Gardner, T.W., Back, W., Bullard, T.F., Hare, P.W., Kesel, R.H., Lowe, D.R., Menges, C.M., Mora, S.C., Pazzaglia, R.J., Sasowsky, I.D., Troester, J.W., Wells, S.G., 1987. Central America and the Caribbean. In: Graf, W.L. (Ed.), *Geomorphic Systems of North America*. Geol. Soc. Am. Centennial special volume, pp. 343– 402.
42. Gardner, T.W., Verdonk, D., Pinter, N.M., Slingerland, R.L., Furlong, K.P., Bullard, T.F., Wells, S.G., 1992. Quaternary uplift astride the aseismic Cocos Ridge, Pacific Coast, Costa Rica. *Geol. Soc. Amer. Bull.* 104, 219–232.
43. Hamilton, E. L., 1972. Compressional-wave attenuation in marine sediments, *Geophysics*, 37, 620-646.
44. Hamilton, W.B., 2007. Driving mechanism and 3-D circulation of plate tectonics: *Geol. Soc. America Special Paper* 433, p. 1-25.
45. Hauff, F., Hoernle, K., Schmincke, H.-U., and Werner, R., 1997. A mid Cretaceous origin for the Gala'pagos hotspot: Volcanological, petrological and geochemical evidence from Costa Rican oceanic crustal segments: *Geologische Rundschau*, 86, 141–155.
46. Hauff, F., Hoernle, K., van den Bogaard, P., Alvarado, G, and Garbe-Schönberg, D., 2000a. Age and geochemistry of basaltic complexes in western Costa Rica: Contributions to the geotectonic evolution of Central America. *Geochem. Geophys. Geosyst.*, 1, 221–235.
47. Hauff, F., Hoernle, K., Tilton, G., Graham, D., and Kerr, A.C., 2000b. Large volume recycling of oceanic lithosphere: Geochemical evidence from the Caribbean large igneous province. *Earth and Planetary Science Letters*, 174, 247–263

48. Hey, R., 1977. Tectonic evolution of the Cocos-Nazca spreading center, *Geol. Soc. Am. Bull.*, 88, 1404-1420.
49. Hensen, C., Wallmann, K., Schmidt, M., Ranero, C. R., Suess, E., 2004. Fluid expulsion related to mud extrusion off Costa Rica- A window to the subducting slab, *Geology*, 32, 201-204.
50. Hilde, T. W. C., 1983. Sediment subduction vs accretion around the Pacific. *Tectonophysics*, 99, 381-397.
51. Hinz, K., von Huene, R., Ranero, C.R., and PACOMAR Group, 1996. Tectonic structure of the convergent Pacific margin offshore Costa Rica from multichannel seismic reflection data, *Tectonics*, 15(1), 54-66.
52. Hoernle, K., van den Bogaard, P., Werner, R., Lissinna, B., Hauff, F., Alvarado, G, and Garbe-Schönberg, D., 2002. Tectonic and biological evolution of the Americas Missing history (16–71 Ma) of the Galápagos hotspot: Implications for the tectonic and biological evolution of the Americas. *Geology*, 30, 795-798.
53. Ibrahim, A. B., Latham, G. V., and Ladd, J., 1979. Seismic refraction and reflection measurements in Middle America Trench offshore Guatemala. *J. geophys. Res.*, 84(B10), 5643-5649.
54. Kennett, B. L. N., 1977. Towards a more detailed seismic picture of the oceanic crust and mantle, *Mar. Geophys. Res.*, 3, 7-42.
55. Kim, J., Matumoto, T., and Latham, G., 1982. A crustal section of northern Central America as inferred from wide-angle reflections from shallow earthquakes. *Bull. Seismol. Soc. Am.*, 72, 925-940.
56. Kimura, G., Sliver, E., Blum, P., et al., 1997. Proceedings of the Ocean Drilling Program, *Init. Rep.*, Volume 170: College Station, Texas, Ocean Drilling Program, 458 p.
57. Kious, W. J., & Tilling, R. I., 1996. This Dynamic Earth: the Story of Plate Tectonics. U.S. Geological Survey, Denver, Colorado, General Interest Publication.

58. Kodaira, S., Takahashi, N., Nakanishi, A., Miura, S., & Kaneda, Y., 2000. Subducted seamount imaged in the rupture zone of the 1946 Nankaido earthquake, *Science*, 289, 104-106.
59. Kopp, H., Flueh, E. R., Klaeschen, D., Bialas, J., and Reichert, C., 2001. Crustal structure of the central Sunda margin at the onset of oblique subduction, *Geophys. J. Int.*, 147, 449-474.
60. Kopp, H., Flueh, E. R., Petersen, C. J., Weinrebe, W., & Wittwer, A., Meramex Scientists, 2006. The Java margin revisited: Evidence for subduction erosion off Java, *Earth planet. Sci. Lett.*, 242, 130-142.
61. Korenaga, J., Holbrook, W. S., Kent, G. M., Kelemen, P. B., Detrick, R. S., Larsen, H.-C., Hopper, J. R., and Dahl-Jensen, T., 2000. Crustal structure of the southeast Greenland margin from joint refraction and reflection seismic tomography, *J. geophys. Res.*, 105, 21591–21614.
62. Kuijpers, E. P., 1980. The geologic history of the Nicoya Ophiolite Complex, Costa Rica, and its geotectonic significance, *Tectonophysics*, 68, 233-255.
63. Kukowski, N., von Huene, R., Malavieille, J., and Lallemand, S.E., 1994, Sediment accretion against a buttress beneath the Peruvian continental margin at 128S as simulated with sandbox modeling: *Geologische Rundschau*, 83, 822–831.
64. Lallemand, S., Schnurle, P., and Malavieille, J., 1994. Coulomb theory applied to accretionary and nonaccretionary wedges: Possible causes for tectonic erosion and/or frontal accretion. *J. geophys. Res.*, 99(B6), 12,033–12,055
65. Le Pichon, X., and Henry, P., 1992. Erosion and accretion along subduction zones: A model of evolution: Proceedings, Koninklijke Nederlandse Akademie van Wetenschappen, v. 95, p. 297–310.
66. Le Pichon, X., Henry, P., Lallemand, S., 1993. Accretion and erosion in subduction zones: The role of fluids. *Annu. Rev. Earth Planet. Sci.* 21, 307–331.
67. Ligorría, J. P., and Molina, E., 1997. Crustal velocity structure of southern

- Guatemala using refracted and Sp converted waves. *Geofisica International*, 36, 7-16.
68. Luetgert, J. H., 1992. MacRay-Interactive two-dimensional seismic raytracing for the Macintosh, U.S. Geol. Surv. Open File Report 92-356.
69. McIntosh, K., Silver, E., Shipley, T., 1993. Evidence and mechanisms for forearc extension at the accretionary Costa Rica convergent margin, *Tectonics*, 12, 1380-1392.
70. MacMillan, I., Gans, P., Alvarado, G., 2004. Middle Miocene to present plate tectonic history of the southern Central American Volcanic Arc. *Tectonophysics*, 392, 325-348.
71. Mann, P., Rogers, R. D., and Gahagan, L., 2007. Overview of plate tectonic history and its unresolved tectonic problems. In Bunddchuh, J. and Alvarado, G., editors, *Central America: Geology, Resources and Hazards*, pp. 267–274. Taylor & Francis.
72. Marshall, J. S., 2007. Geomorphology and physiography provinces. In Bunddchuh, J. and Alvarado, G., editors, *Central America: Geology, Resources and Hazards*, pp. 75–122. Taylor & Francis.
73. Matumoto, T., Ohtake, M., Latham, G., and Umana, J., 1977. Crustal structure in southern Central America. *Bull. seism. Soc. Am.*, 67, 121–134.
74. Menke, W., Levin, V., Sethi, R., 1995. Seismic attenuation in the crust at the mid-Atlantic plate boundary in south-west Iceland, *Geophys. J. Int*, 122, 175-182.
75. Meschede, M., Zweigel, P., Frisch, W., Voelker, D., 1999a. Melange formation by subduction erosion: the case of the Osa melange in southern Costa Rica, *Terra Nova*, 11, 141-148.
76. Meschede, M., Zweigel, P., & Kiefer, E., 1999b. Subsidence and extension at a convergent plate margin: evidence for subduction erosion off Costa Rica, *Terra Nova*, 11, 112-117.
77. Miura, R., Nakamura, Y., Koda, K., Tokuyama, H., & Coffin, M. F., 2004.

“Rootless” serpentinite seamount on the southern Izu-Bonin forearc: Implications for basal erosion at convergent plate margins, *Geology*, 32, 541-544.

78. Moore, J. C., and Vrolijk, P., 1992. Fluids in accretionary prisms, *Rev. Geophys.*, 30, 113–135.

79. Moser, T.J., 1991. Shortest path calculation of seismic rays, *Geophysics*, 56, 59-67.

80. Moser, T.J., G. Nolet, and R. Snieder, Ray bending revisited, *Bull. Seismol. Soc. Am.*, 82, 259-288, 1992.

81. Mueller, G., 1985. The reflectivity method: A tutorial, *J. Geophysics*, 58, 153-174.

82. Paige, C.C., and M.A. Saunders, 1982. LSQR: An algorithm for sparse linear equations and sparse least squares, *Trans. Math. Software*, 8, 43-71.

83. Papazachos, C., and G. Nolet, P and S deep velocity structure of the Hellenic area obtained by robust nonlinear inversion of travel times, *J. geophys. Res.*, 102, 8349-8367, 1997.

84. Protti, M., Guendel, F., & McNally, K., 1995. Correlation between the age of the subducting Cocos plate and the geometry of the Wadati-Benioff zone under Nicaragua and Costa Rica, in *Geologic and Tectonic Development of the Caribbean Plate Boundary in Southern Central America*, edited by Mann, P., *Geol. Soc. Am. Spec. Pap.*, 295, 309-326.

85. Ranero, C. R., & von Huene, R., 2000. Subduction erosion along the Middle America convergent margin, *Nature*, 404, 748-752.

86. Ranero, C. R., Villasenor, A., Morgan, J. P., and Weinrebe, W., 2005. Relationship between bend-faulting at trenches and intermediate-depth seismicity, *Geochem. Geophys. Geosyst.*, 6, Q12002, doi: 10.1029/2005GC000997.

87. Ranero, C. R., Grevemeyer, I., Sahling, H., Barckhausen, U., Heslen, C., Wallmann, K., Weinrebe, W., Vannucchi, P., von Huene, R., McIntosh, K., 2008. Hydrogeological system of erosional convergent margins and its influence on

tectonics and interplate seismogenesis, *Geochem. Geophys. Geosyst.*, 9, Q03S04, doi: 10.1029/2007GC001679.

88. Ross, D. A., Shor, G. G. Jr., 1965. Reflection profiles across the Middle America Trench. *J. geophys. Res.*, 70, 5551-5572.

89. Sage, F., Collot, J.-Y., & Ranero, C. R., 2006. Interplate patchiness and subduction-erosion mechanisms: Evidence from depth-migrated seismic images at the central Ecuador convergent margin, *Geology*, 34, 997-1000.

90. Sallarès, V., Charvis, P., 2003. Crustal thickness constraints on the geodynamic evolution of the Galapagos Volcanic Province. *Earth and Planetary Science Letters*, 214, 545–559.

91. Sallarès, V., Dañobeitia, J. J., Flueh, E. R., & Leandro, G., 1999. Seismic velocity structure across the middle American landbridge in northern Costa Rica, *J. Geody.*, 27, 327-334.

92. Sallarès, V., Dañobeitia, J. J., & Flueh, E. R., 2001. Lithospheric structure of the Costa Rican Isthmus: Effects of subduction zone magmatism on an oceanic plateau. *J. geophys. Res.*, 106, 621-643.

93. Sallarès, V., and Ranero, C. R., 2005. Structure and tectonics of the erosional convergent margin off Antofagasta, north Chile (23°30'S), *J. geophys. Res.*, 110, B06101, doi:10.1029/2004JB003418.

94. Sandmeier, K. J., & Wenzel, F., 1986. Synthetic seismograms for a complex crustal model, *Geophys. Res. Lett.*, 13(1), 22-25.

95. Shaw, P.R., and J.A. Orcutt, Waveform inversion of seismic refraction data and applications to young Pacific crust, *Geophys. J. R. Astron. Soc.*, 82, 375-414, 1985.

96. Shor, G. G. Jr., Fisher, R. L., 1961. Middle America Trench: seismic-refraction studies. *Geol. Soc. Am. Bull.*, 72, 721-730.

97. Simkin, T., Tilling, R.J., Taggart, J.N., Jones, W.J., and Spall, H., 1989, This Dynamic Planet—World Map of Volcanoes, Earthquakes, and Plate Tectonics: U.S.

Geological Survey. Map I-2800, scale 1:30,000,000.

98. Sinton, C. W., Duncan, R. A. and Denyer, P., 1997. Nicoya Peninsula, Costa Rica: A single suite of Caribbean oceanic plateau magmas, *J. Geophys. Res.*, 102(B7), 15,507–15,520.

99. Soeding, E., Wallmann, K., Suess, E., and Flueh, E., 2003. FS Meteor, cruise report M 54/2-3: Caldera-Curacao: *GEOMAR Report 111*, 366 p.

100. Spudich, P., & Orcutt, J., 1980. Petrology and porosity of an oceanic crustal site: results from wave form modeling of seismic refraction data, *J. geophys. Res.*, B3, 1409-1433.

101. Stavenhagen, A. U., Flueh, E. R., Ranero, C. R., McIntosh, K. D., Shipley, T., Leandro, G., Schulze, A., & Dañobeitia, J. J., 1998. Seismic wide-angle investigations in Costa Rica- a crustal velocity model from the Pacific to the caribbean coast, *Zbl. Geol. Paläont., Teil I*, 3-6: 393-408.

102. Stockwell, J. W., 1999. The CWP/SU: Seismic Un*x package, *Comput. Geosci.*, 25(4), 415– 419.

103. Toksöz, M. N., Wu, R. S., and Schmitt, D. P., 1987. Physical mechanisms contributing to seismic attenuation in the crust, 225-247, in: Erdik, M. O., and Toksöz, M. N., (Eds), *Strong Ground Motion Seismology*, D. Reidel Publishing Company, Dordrecht.

104. Tarantola, A., 1987. *Inverse Problem Theory: Methods for Data Fitting and Model Parameter Estimation* , 613 pp., Elsevier, New York .

105. Tarantola, A., and Valette, B, 1982. Inverse problems = quest for information, *J. Geophysics*, 50, 159-170.

106. Toomey, D.R., and G.R. Foulger, Tomographic inversion of local earthquake data from the Hengill-Grensdalur central volcano complex, Iceland, *J. geophys. Res.*, 94, 17,497-17,510, 1989.

107. Toomey, D.R., S.C. Solomon, and G.M. Purdy, Tomographic imaging of the

shallow crustal structure of the East Pacific Rise at 9°30'N, *J. geophys. Res.*, 99, 24,135-24,157, 1994.

108. Tsuru, T., Park, J.-O., Miura, S., Kodaira, S., Kido, Y., and Hayashi, T., 2002. Along-arc structural variation of the plate boundary at the Japan Trench margin: Implication of interpolate coupling, *J. geophys. Res.*, 107(B12), 2357, doi: 10.1029/2001JB001664.

109. Um, J., and C. Thurber, 1987. A fast algorithm for two-point seismic ray tracing, *Bull. Seismol. Soc. Am.*, 77, 972-986.

110. Van Avendonk, H.J.A., A.J. Harding, and J.A. Orcutt, 1988. A two-dimensional tomographic study of the Clipperton transform fault. *J. geophys. Res.*, 103, 17,885-17,899.

111. Vannucchi, P., Scholl, D. W., Meschede, M., & McDougall-Reid, K., 2001. Tectonic erosion and consequent collapse of the Pacific margin of Costa Rica: Combined implications from ODP Leg 170, seismic offshore data, and regional geology of the Nicoya Peninsula, *Tectonics*, 20, 649-668.

112. Vannucchi, P., Ranero, C. R., Galeotti, S., Straub, S. M., Scholl, D. W., & McDougall-Reid, K., 2003. Fast rates of subduction along the Costa Rica Pacific margin: Implications for nonsteady rates of crustal recycling at subduction zones, *J. geophys. Res.*, 108(B11), 2511, doi: 10.1029/2002JB002207.

113. von Huene, R., 1986. To accrete or not accrete, that is the question, *Geol. Rndsch.*, 75, 1-15.

114. von Huene, R., & Scholl, D. W., 1991. Observations at convergent margins concerning sediment subduction, subduction erosion, and the growth of continental crust, *Rev. Geophys.*, 29, 279-316.

115. von Huene, R., & Flueh, E. R., 1994. A review of marine geophysical studies along the Middle American Trench off Costa Rica and the problematic seaward terminus of continental crust, *Profil* 7, 143-159, Univ. of Stuttgart, Stuttgart, Germany.

116. von Huene, R. et al., 1995. Morphotectonics of the Pacific convergent margin of Costa Rica, in Geologic and tectonic development of the Caribbean Plate Boundary in Southern Central America, edited by Mann, P., *Geol. Soc. Am. Spec. Pap.*, 295, 291-308.
117. von Huene, R., & Lallemand, S., 1990. Tectonic erosion along the Japan and Peru convergent margins, *Geol. Soc. Am. Bull.*, 102, 704-720.
118. von Huene, R., Ranero, C. R., & Weinrebe, W., 2000. Quaternary convergent margin tectonics of Costa Rica, segmentation of the Cocos Plate, and Central American volcanism, *Tectonics*, 19, 314-334.
119. von Huene, R., & Ranero, C. R., 2003. Subduction erosion and basal friction along the sediment-starved convergent margin off Antofagasta, Chile, *J. geophys. Res.*, 108(B2), 2079, doi: 10.1029/2001JB001569.
120. von Huene, R., Ranero, C. R., & Vannucchi, P., 2004. Generic model of subduction erosion, *Geology*, 32, 913-916.
121. von Huene, R., Ranero, C. R., & Scholl, D. W., 2009. Convergent margin structure in high quality geophysical images and current kinematic and dynamic models, in: Subduction Zones Geodynamics, S. Lallemand and F. Funiciello Eds., *Frontiers in Earth Sciences*, vol. 2, pp. 137-157, Springer, Berlin, Heidelberg, in press.
122. Walther, C. H. E., 2003. The crustal structure of the Cocos ridge off Costa Rica, *J. geophys. Res.*, 108(B3), 2136, doi: 10.1029/2001JB000888.
123. Walther, C. H. E., Flueh, E. R., Ranero, C. R., von Huene, R., and Strauch, W., 2000. Crustal structure across the Pacific margin of Nicaragua: evidence for ophiolitic basement and a shallow mantle sliver, *Geophys. J. Int.*, 141, 759-777.
124. Weinrebe, W., & Flueh, E. R., 2002. SUBDUCTION 1, FS SONNE Cruise Report SO163 1&2, Multi-system analysis of fluid recycling and geodynamics at the continental margin off Costa Rica, *GEOMAR Report 106*, 534p.
125. Wang, K., & Hu, Y., 2006. Accretionary prisms in subduction earthquake cycles:

The theory of dynamic Coulomb wedge, *J. geophys. Res.*, 111, B06410, doi: 10.1029/2005JB004094.

126. Werner, R., Hoernle, K., van den Bogaard, P., Hauff, F., Korich, D., and Mrazek, J., 1998, Cocos Ridge and adjacent seamounts off the coast of Costa Rica: Insight into the geodynamic evolution of the Galápagos plume. *Terra Nostra*, v. 5, p. 68.

127. Werner, R., Hoernle, K., Van den Bogaard, P., Ranero, C. R., & von Huene, R., 1999. Drowned 14-m.y-old Galapagos archipelago off the coast of Costa Rica: Implications for tectonic and evolutionary models, *Geology*, 27, 499-502.

128. Wessel, P., & Smith, W. H. F., 1991. Free software helps map and display data, *EOS. Trans. Am. geophys. Un.*, 72, 445-446.

129. Weyl, R., 1980. *Geology of Central America*: Berlin-Stuttgart, Borntraeger, 371 p.

130. White, W. M., McBirney, A. R., and Duncan, R. A., 1993. Petrology and geochemistry of the Galápagos Islands: Portrait of a pathological mantle plume. *J. geophys. Res.*, 98 (B11), 19,533–19,563.

131. White, R.S., D. McKenzie, and R.K. O'Nions, 1992. Oceanic crustal thickness from seismic measurements and rare earth element inversions, *J. Geophys. Res.*, 97, 19,683-19,715.

132. Wilcock, W. S. D., Solomon, S. C., Purdy, G. M., Toomey, D. R., 1995. Seismic attenuation structure of the East Pacific Rise near 9°30'N, *J. Geophys. Res.*, 100, 24,147-24,165.

133. Ye, S., Bialas, J., Flueh, E. R., Stavenhagen, A., von Huene, R., Leandro, G., Hinz, K., 1996. Crustal structure of the Middle American Trench off Costa Rica from wide-angle seismic data, *Tectonics*, 15, 1006-1021.

134. Zelt, C.A., and R.B. Smith, Seismic travelttime inversion for 2-D crustal velocity structure, *Geophys. J. Int.*, 108, 16-34, 1992.

135. Zelt, B. C., Taylor, B., & Goodliffe, A. M., 2001. 3-D Crustal velocity structure

at the rift tip in the western Woodlark basin, *Geophys. Res. Lett.*, 28(15), 3015-3018.

136. Zhang, J., and Toksoz, M. N., 1998. Nonlinear refraction traveltime tomography, *Geophysics*, 63, 1726-1773.

137. Zhu, J., H. Kopp, E. R. Flueh, D. Klaeschen, C. Papenberg, L. Planert, 2009. Crustal structure of the central Costa Rica subduction zone: implications for basal erosion from seismic wide-angle data, *Geophys. J. Int.*, 178, 1112-1131.

Appendix A

Selected seismic record sections of lines P15, P24, P18, P22

Table A.1. Phase nomenclature for wide-angle arrivals observed in the seismic record sections displayed in Figures A.1 to A.11

Phase	Description
Pumw	refraction through the upper margin wedge
Plmw	refraction through the lower margin wedge
PtP	reflection from the top of the ‘megalens’
PbP	reflection from the bottom of the ‘megalens’
PiP	reflection from the top of lower oceanic crust
Poc	refraction through the oceanic crust
PmP	reflection from crust-mantle boundary
Pn	refraction through the upper mantle

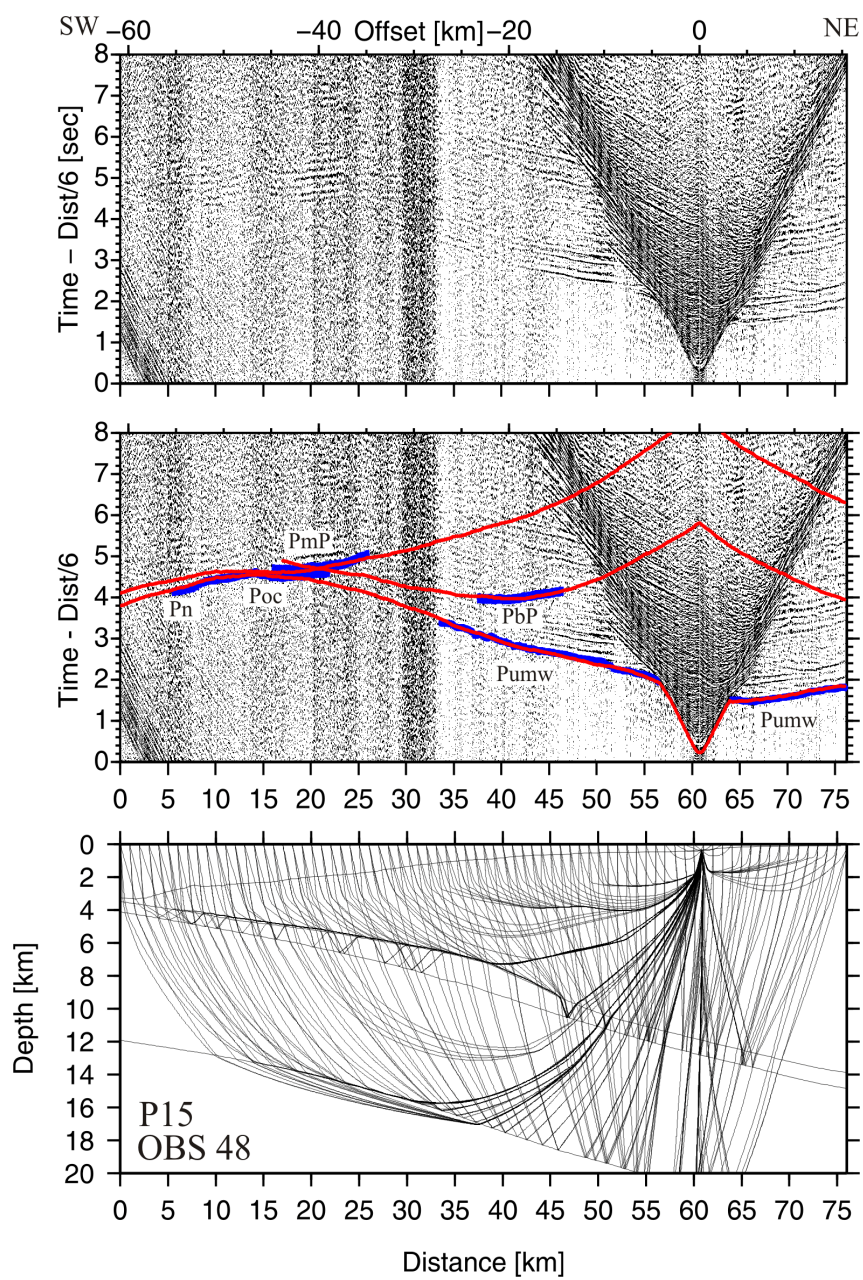


Figure A.1: Dip line P15, OBS48.

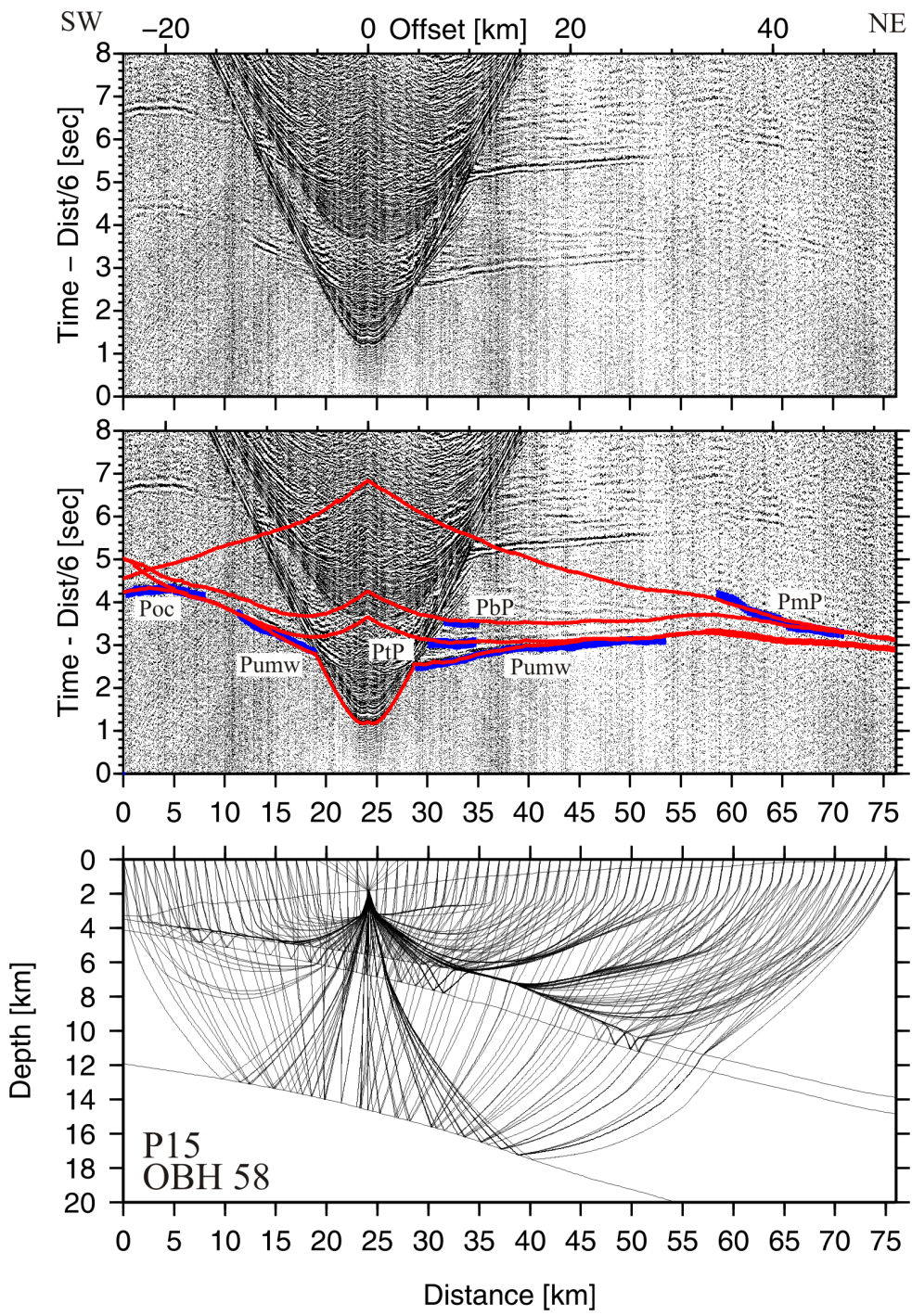


Figure A.2: Dip line P15, OBH58.

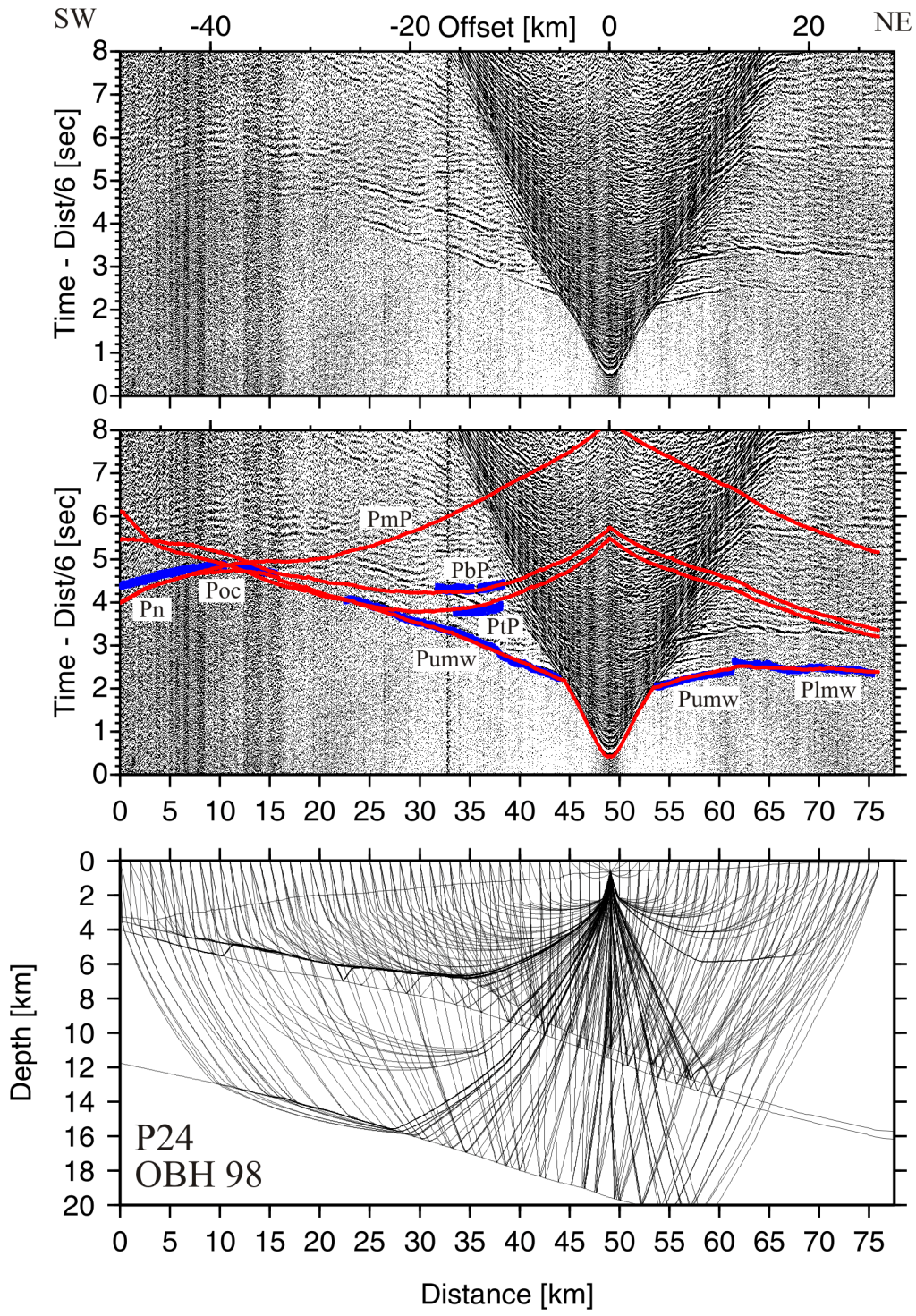


Figure A.3: Dip line P24, OBH98.

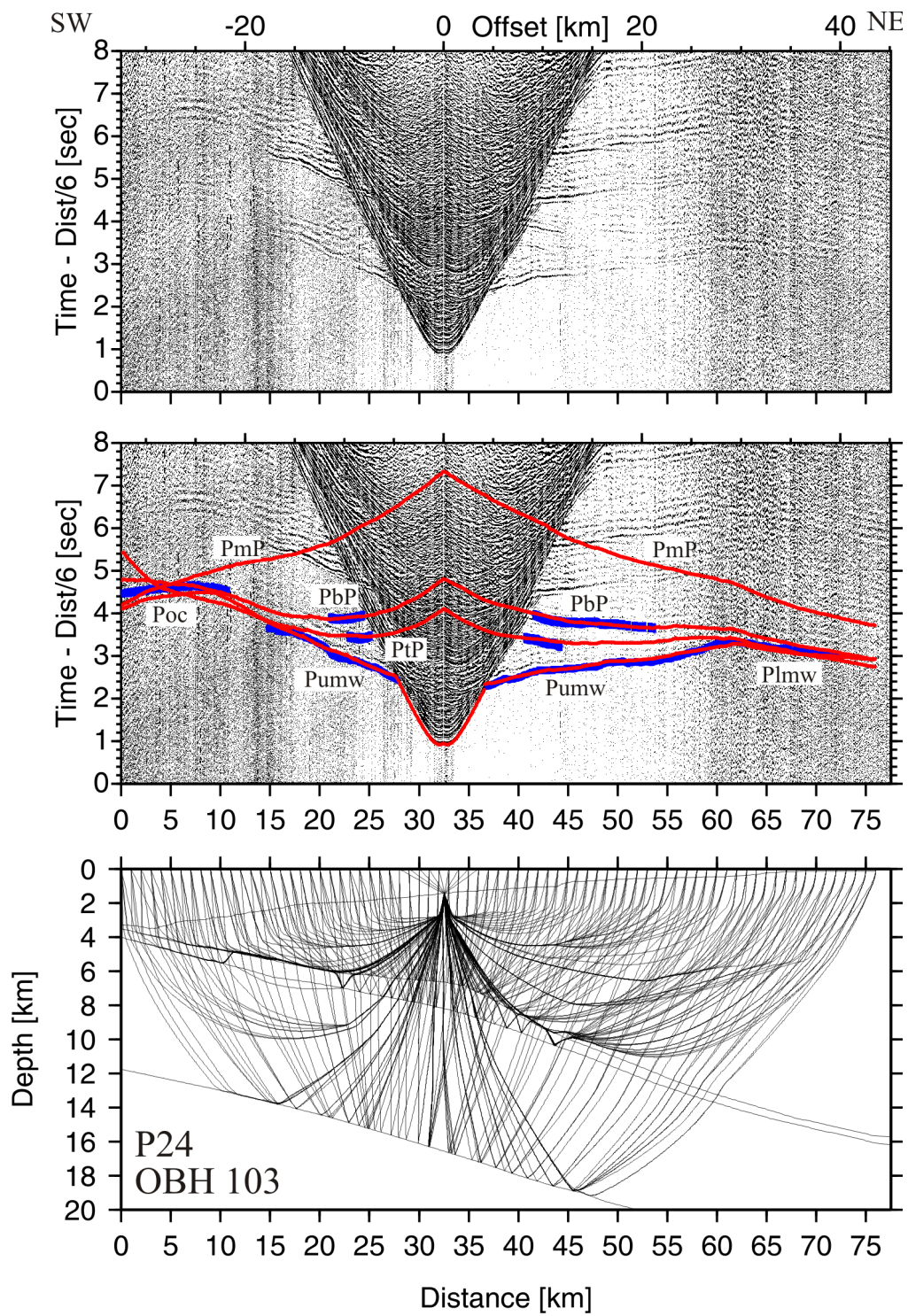


Figure A.4: Dip line P24, OBH103.

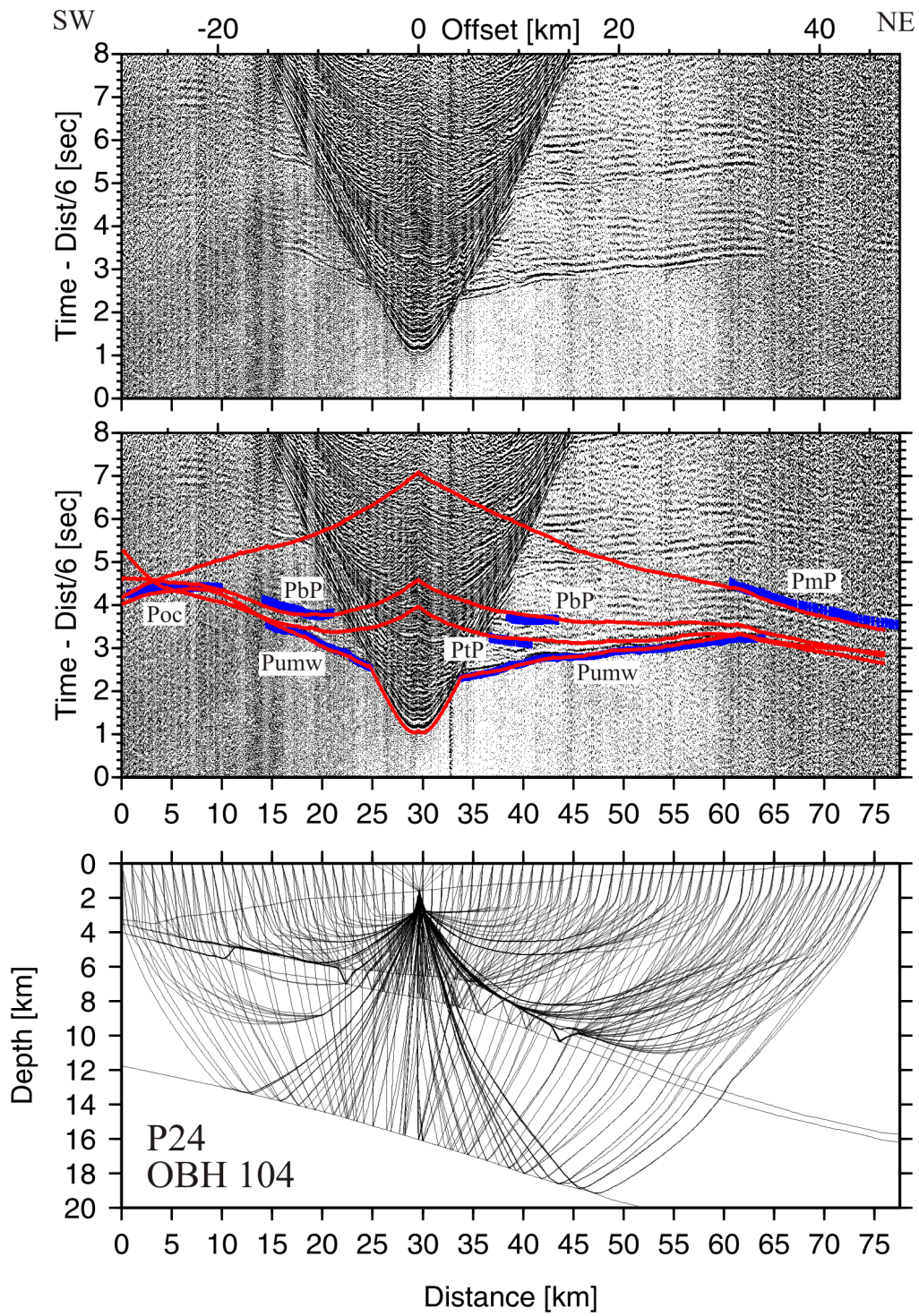


Figure A.5: Dip line P24, OBH104.

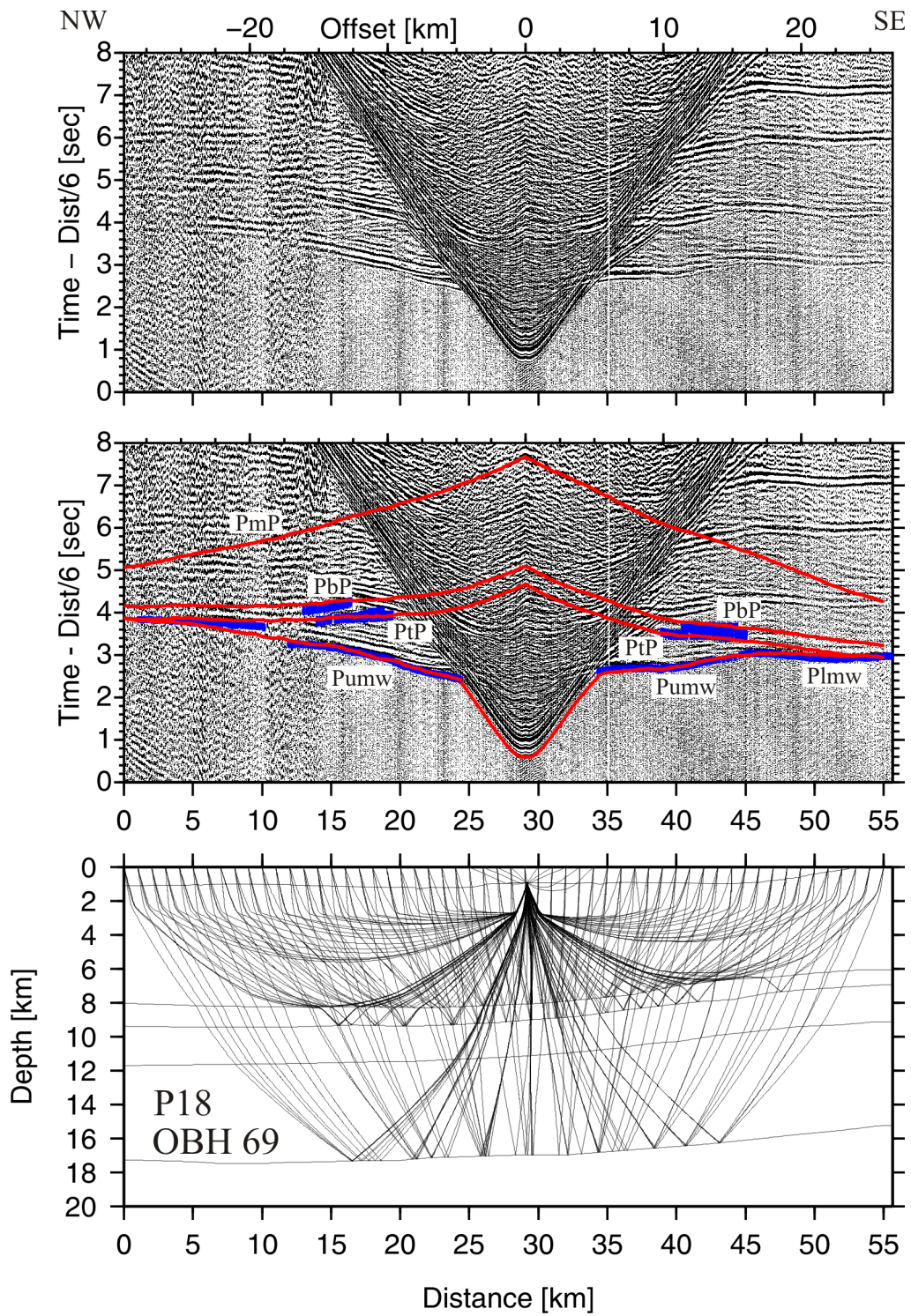


Figure A.6: Strike line P18, OBH69.

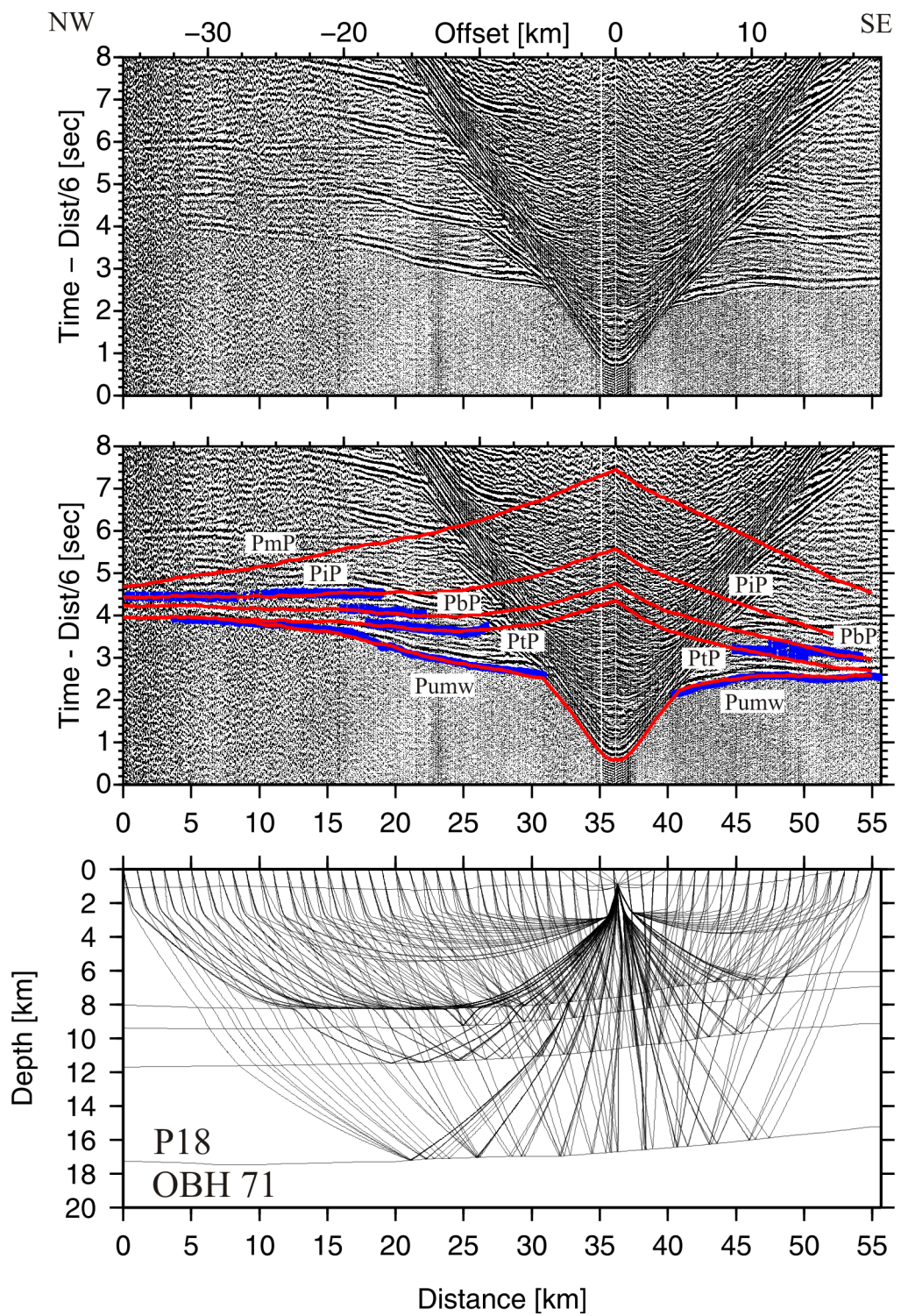


Figure A.7: Strike line P18, OBH71.

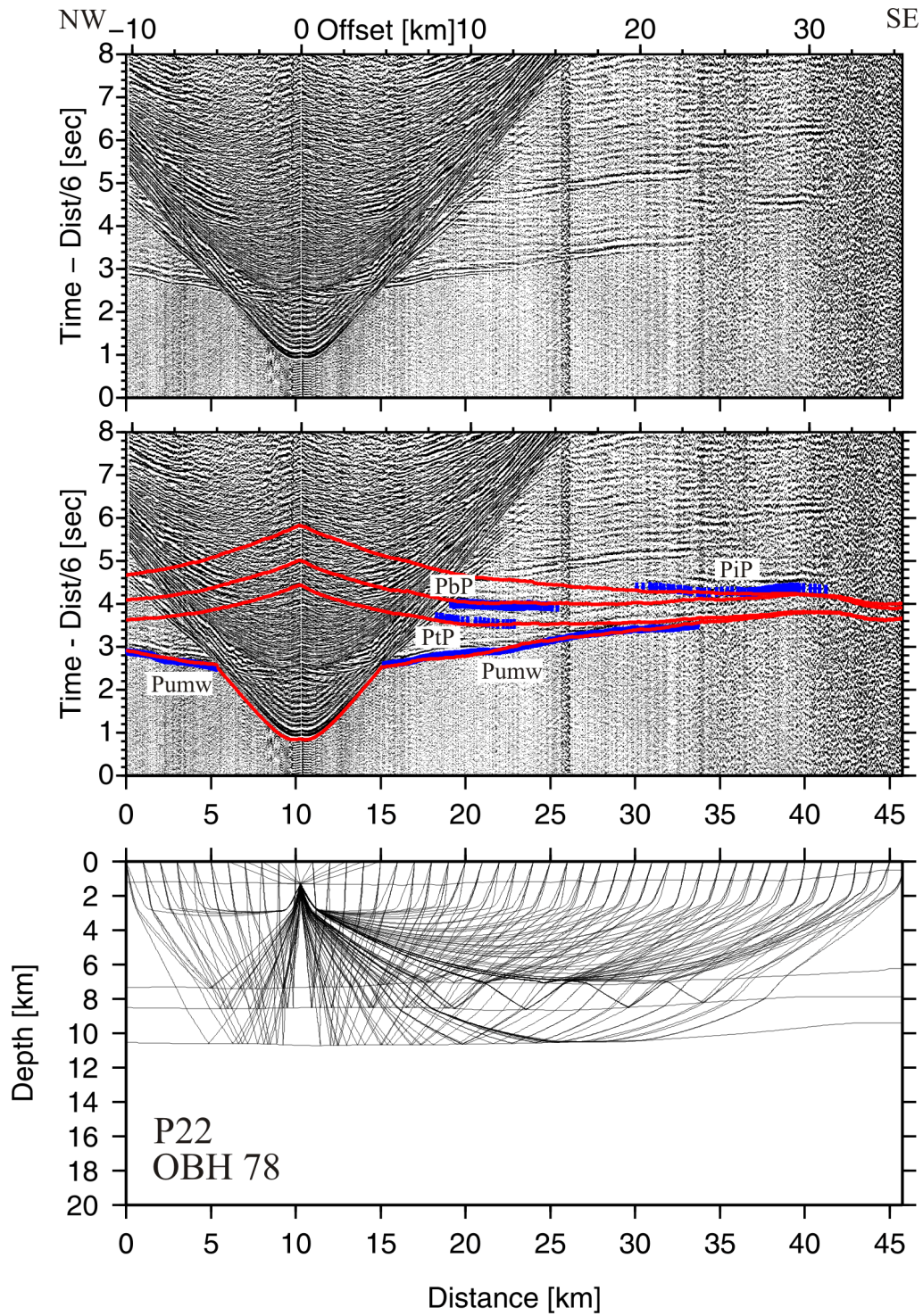


Figure A.8: Strike line P22, OBH78.

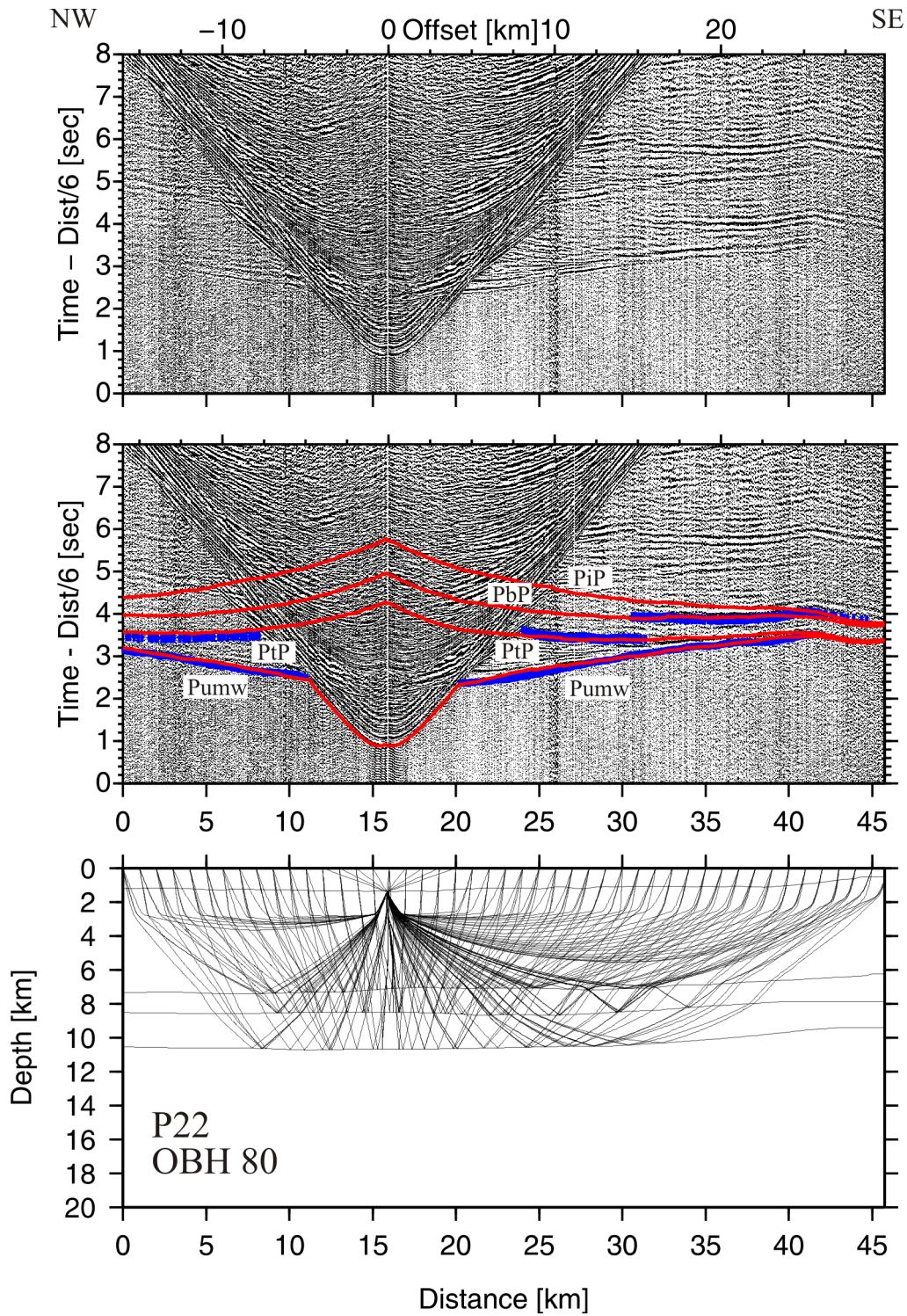


Figure A.9: Strike line P22, OBH80.

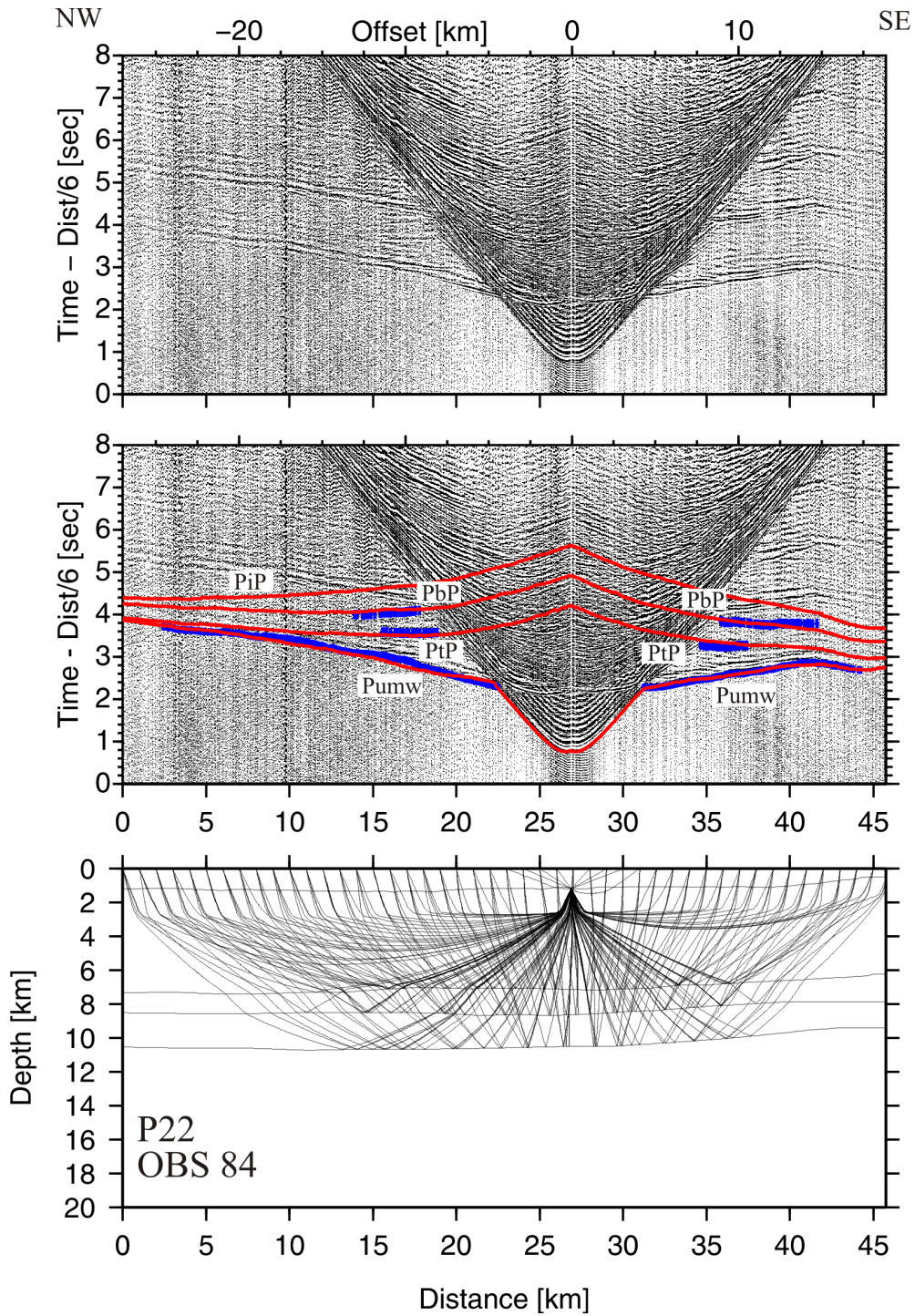


Figure A.10: Strike line P22, OBS84.

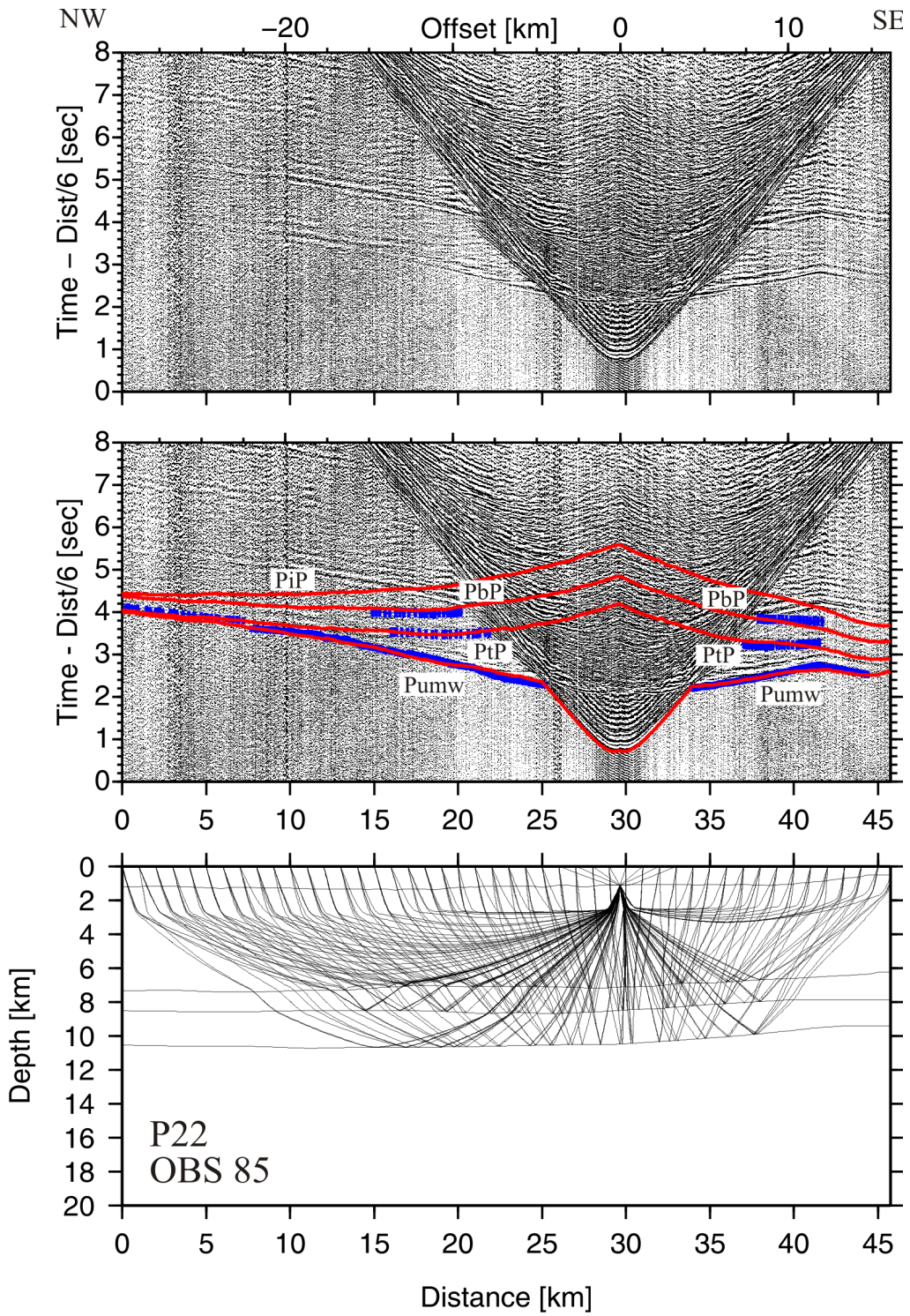


Figure A.11: Strike line P22, OBS85.

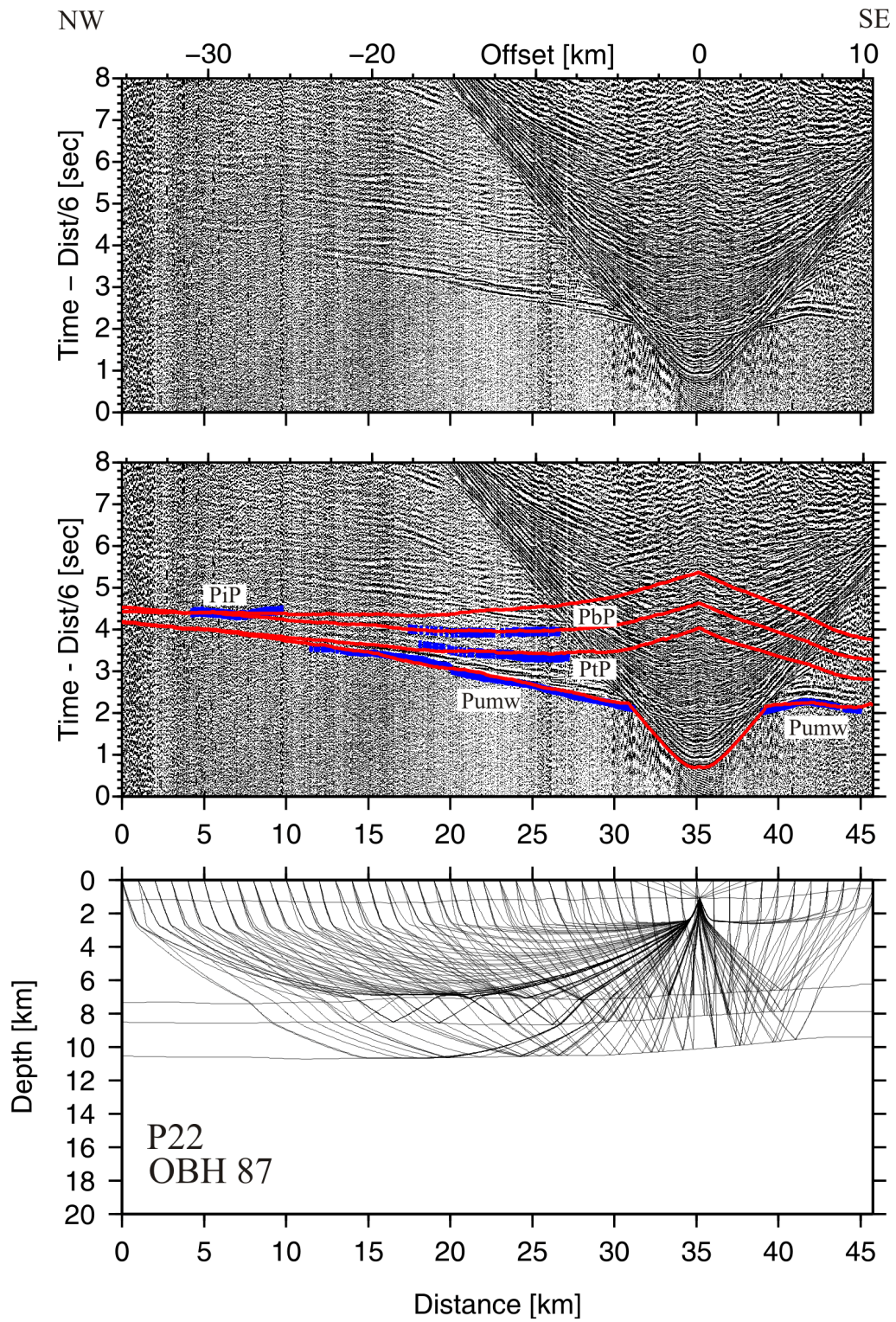
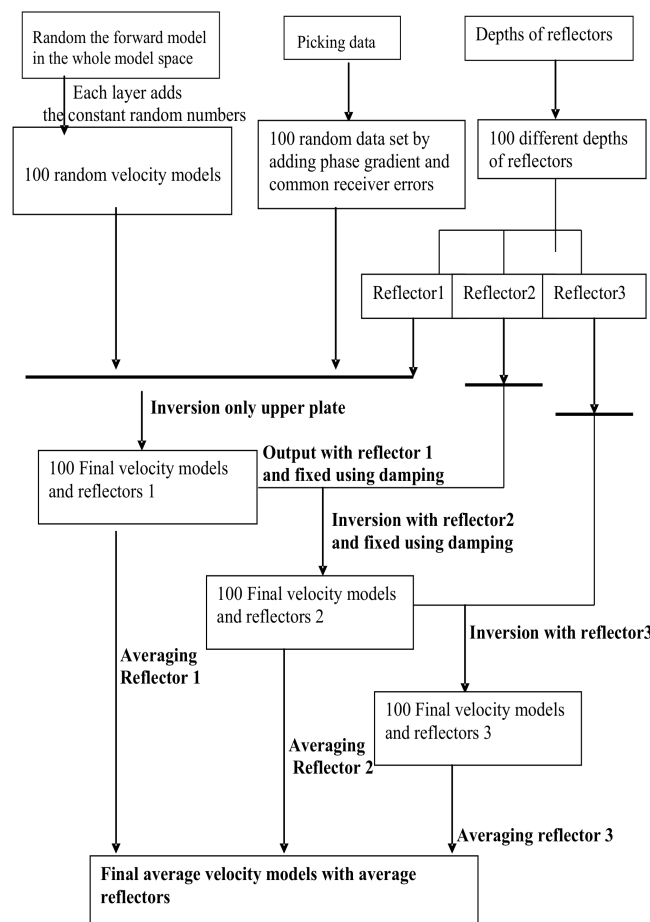


Figure A.11: Strike line P22, OBH87.

Appendix B

Monte Carlo analysis

A practical way to estimate the model uncertainty for tomographic inversion is the Monte Carlo method (Tarantola and Valette, 1982; Tarantola, 1987; Korenaga et al., 2000). The nonlinear Monte Carlo uncertainty was estimated as a posteriori model covariance matrix (Tarantola, 1987), which can also be approximately expressed by the standard deviation of a number of Monte Carlo realizations assuming that all realizations have the same probability (Korenaga et al., 2000). Commonly, 100 random initial velocity models are generated by adding the predefined random numbers to velocity values and depth ranges of a reflector on a 1-D reference model. In this study we vary a 2D forward modeling velocity fields by adding the constant random values at the same layer and also vary the depths of the different reflectors to construct 100 2D random velocity models. A detailed description is provided in Chapter 5. The detailed process flow is displayed in the following chart:



Appendix C

Seismic attenuation along the strike lines P18 and P21

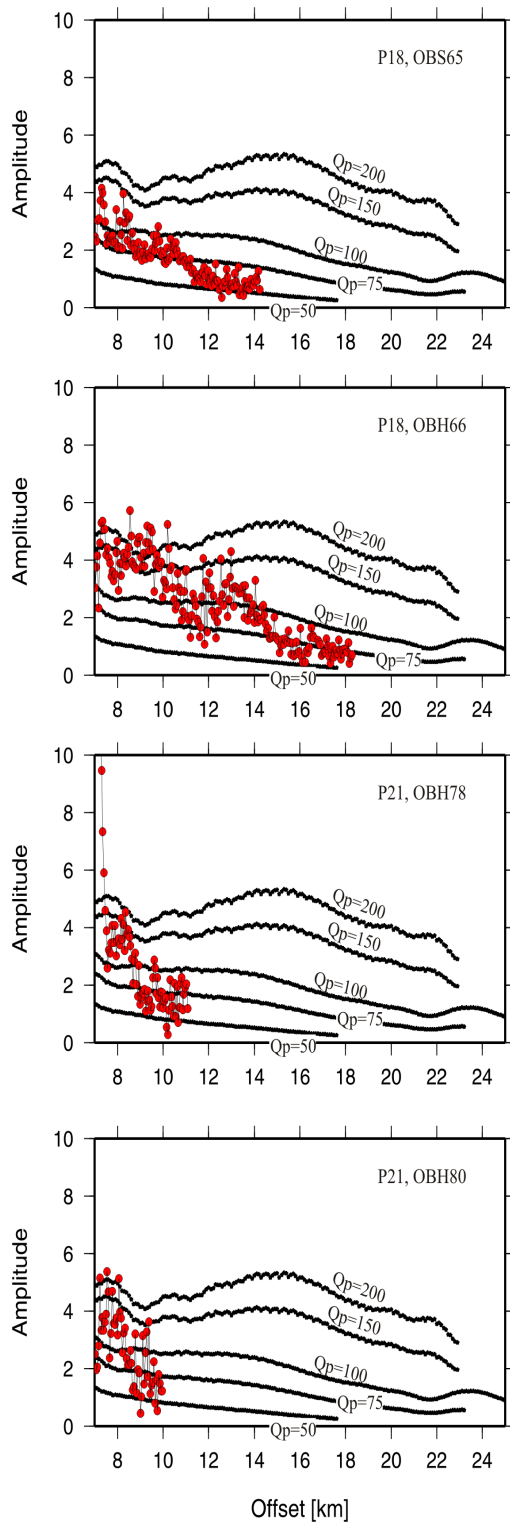


Figure C.1. Amplitude versus offset variations for refracted phases through the margin wedge.

Appendix D

Synthetic seismograms with different Q_p values

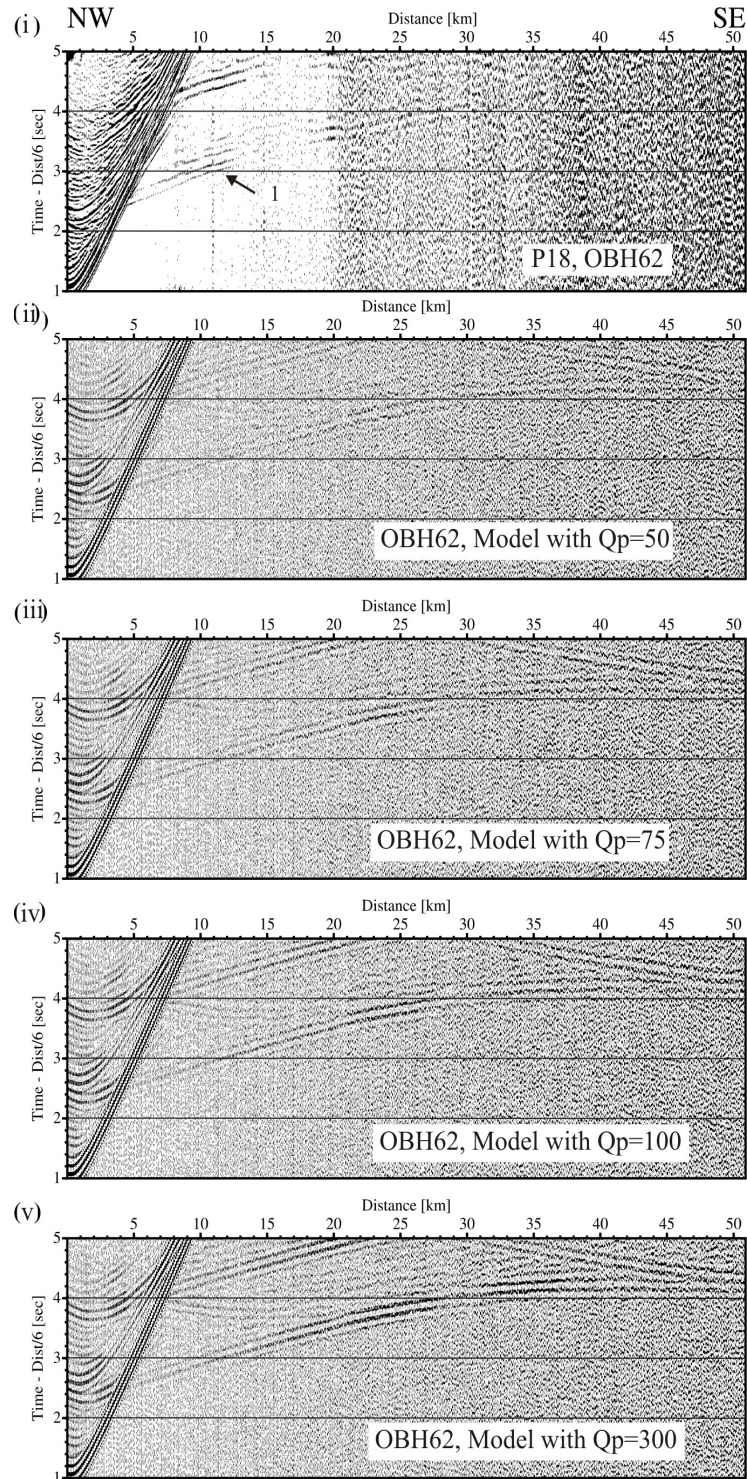


Figure D.1. Synthetic seismogram with different Q_p values for station OBH62.

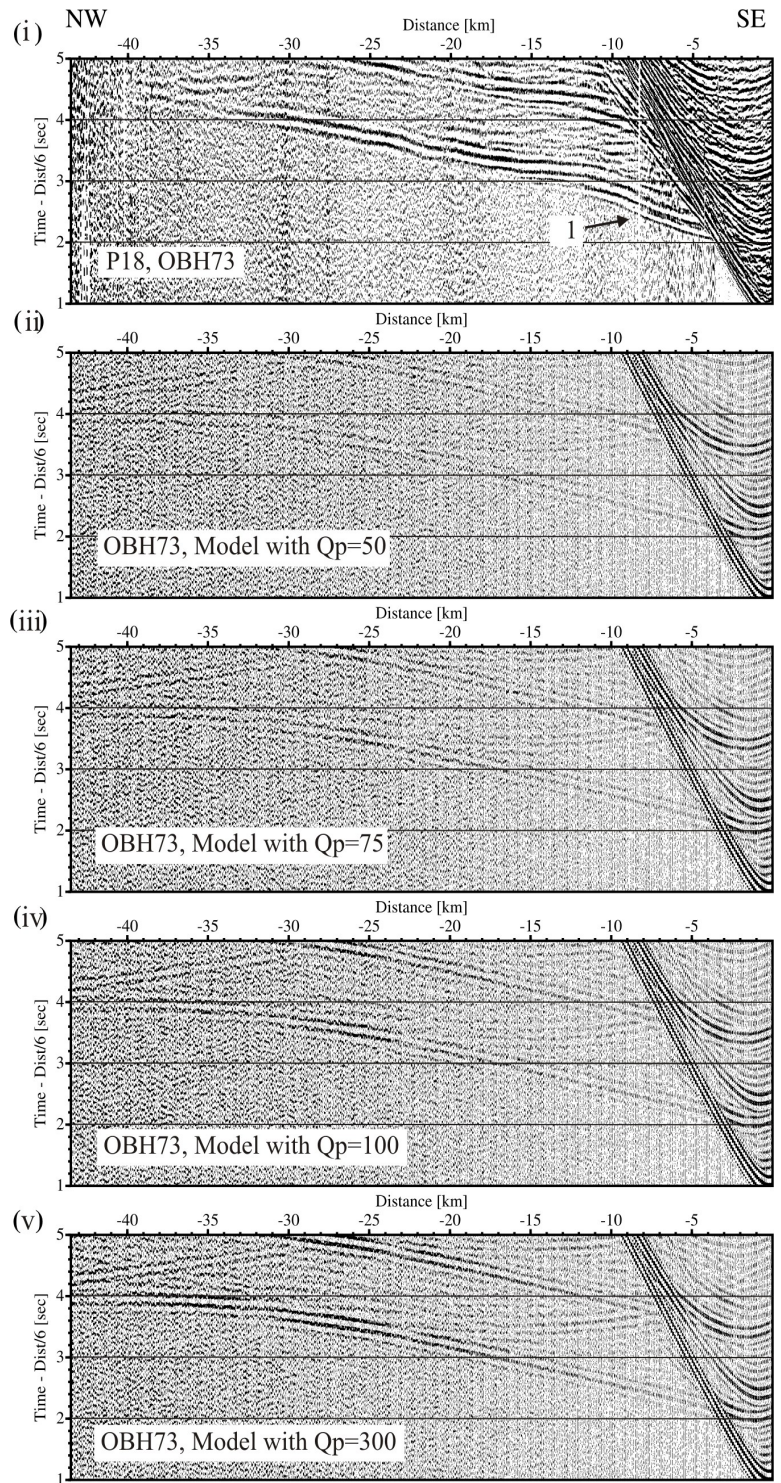


Figure D.2. Synthetic seismogram with different Q_p values for station OBH73.

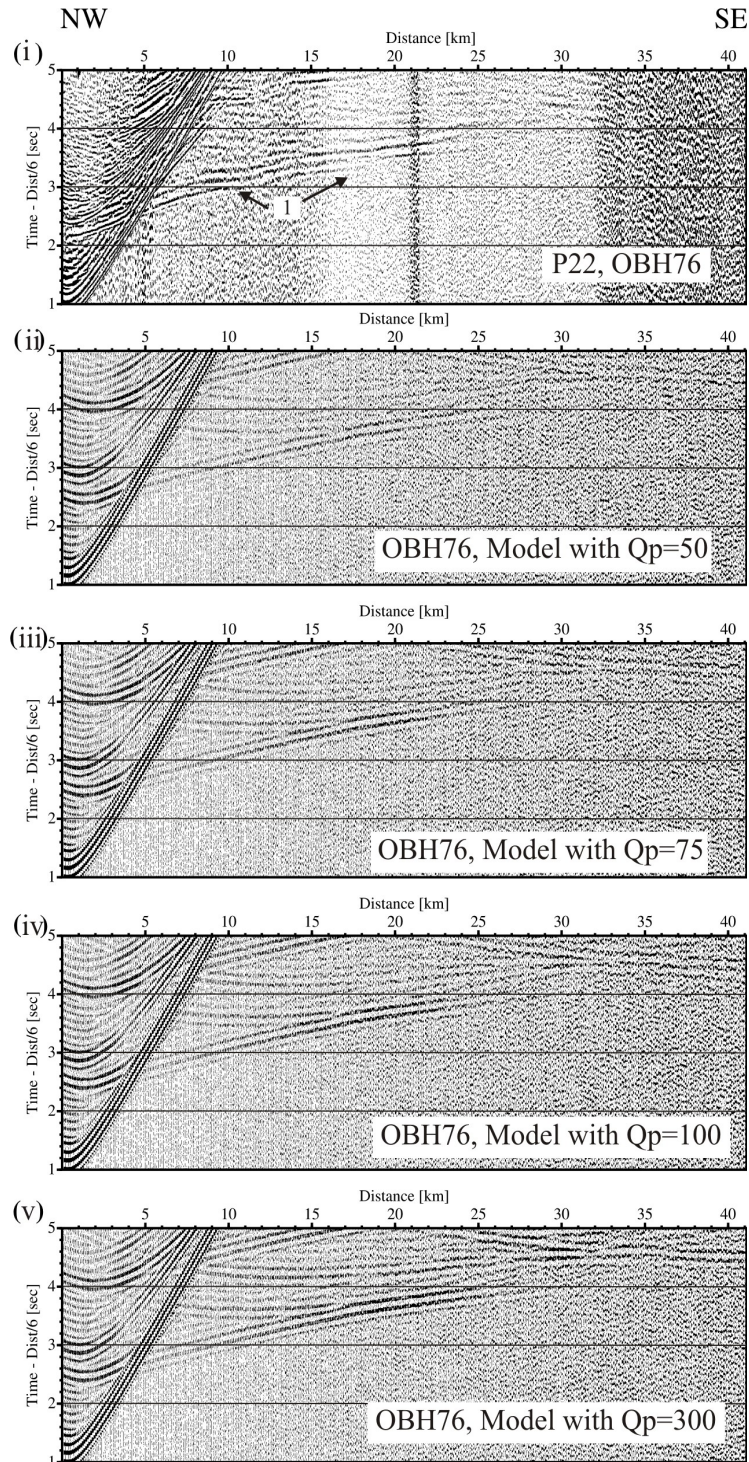


Figure D.3. Synthetic seismogram with different Q_p values for station OBH76.

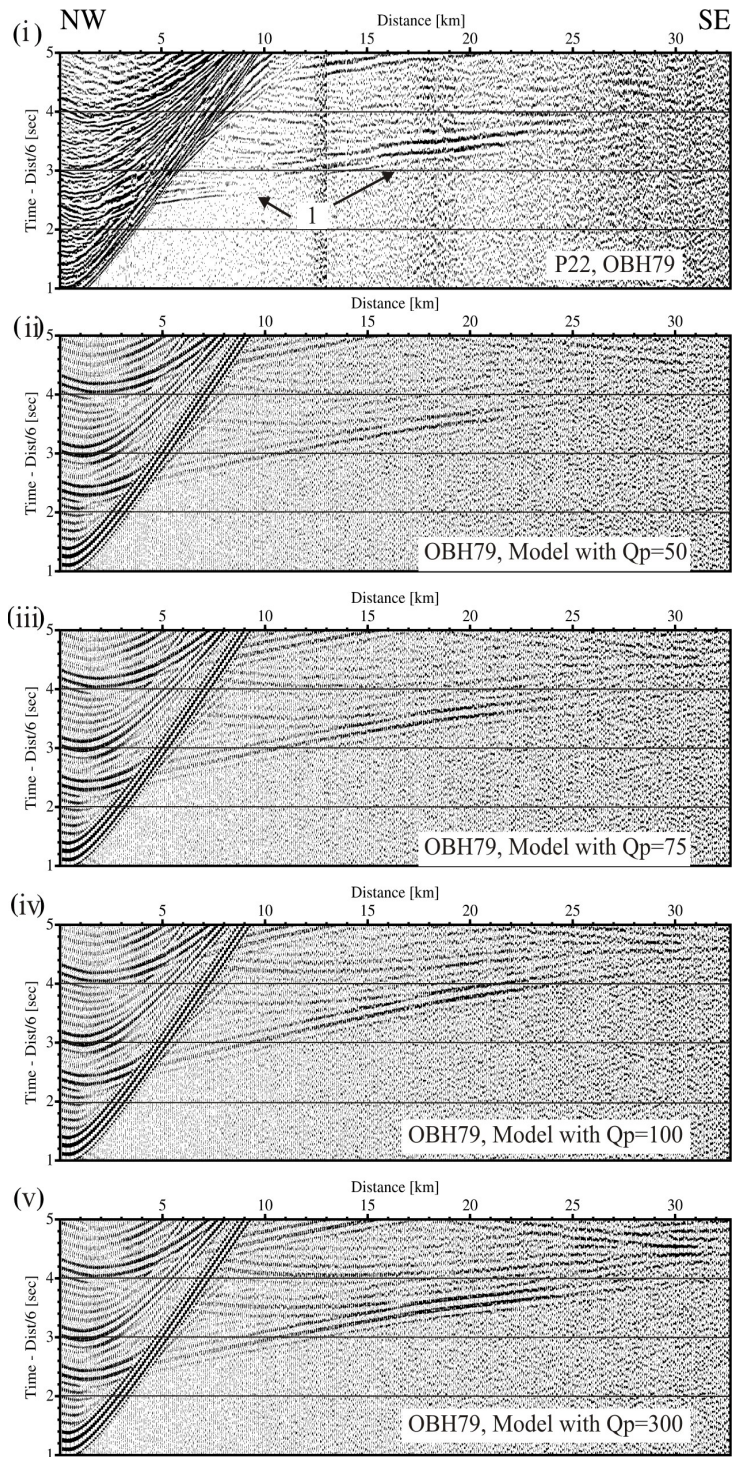


Figure D.4. Synthetic seismogram with different Q_p values for station OBH79.

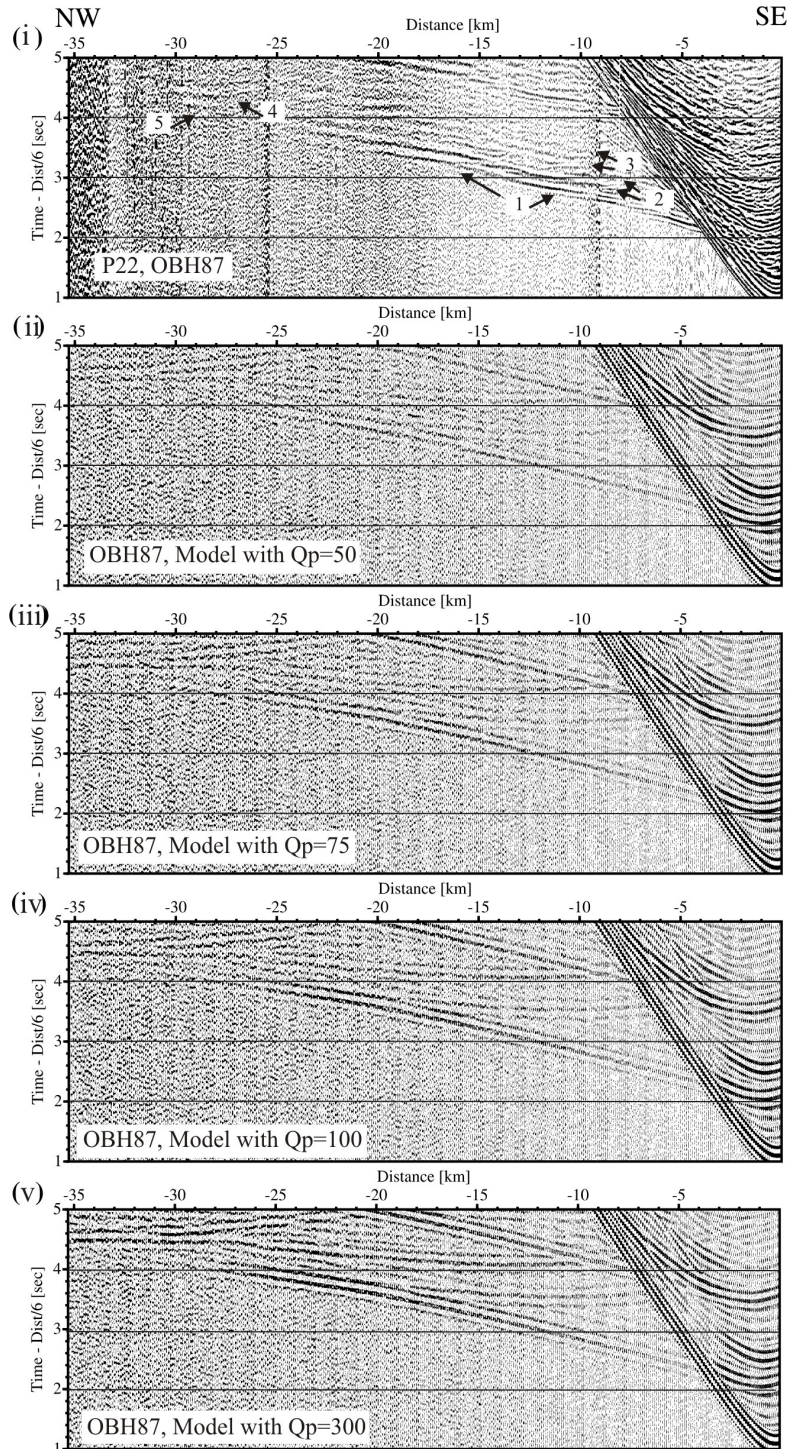


Figure D.5. Synthetic seismogram with different Q_p values for station OBH87.

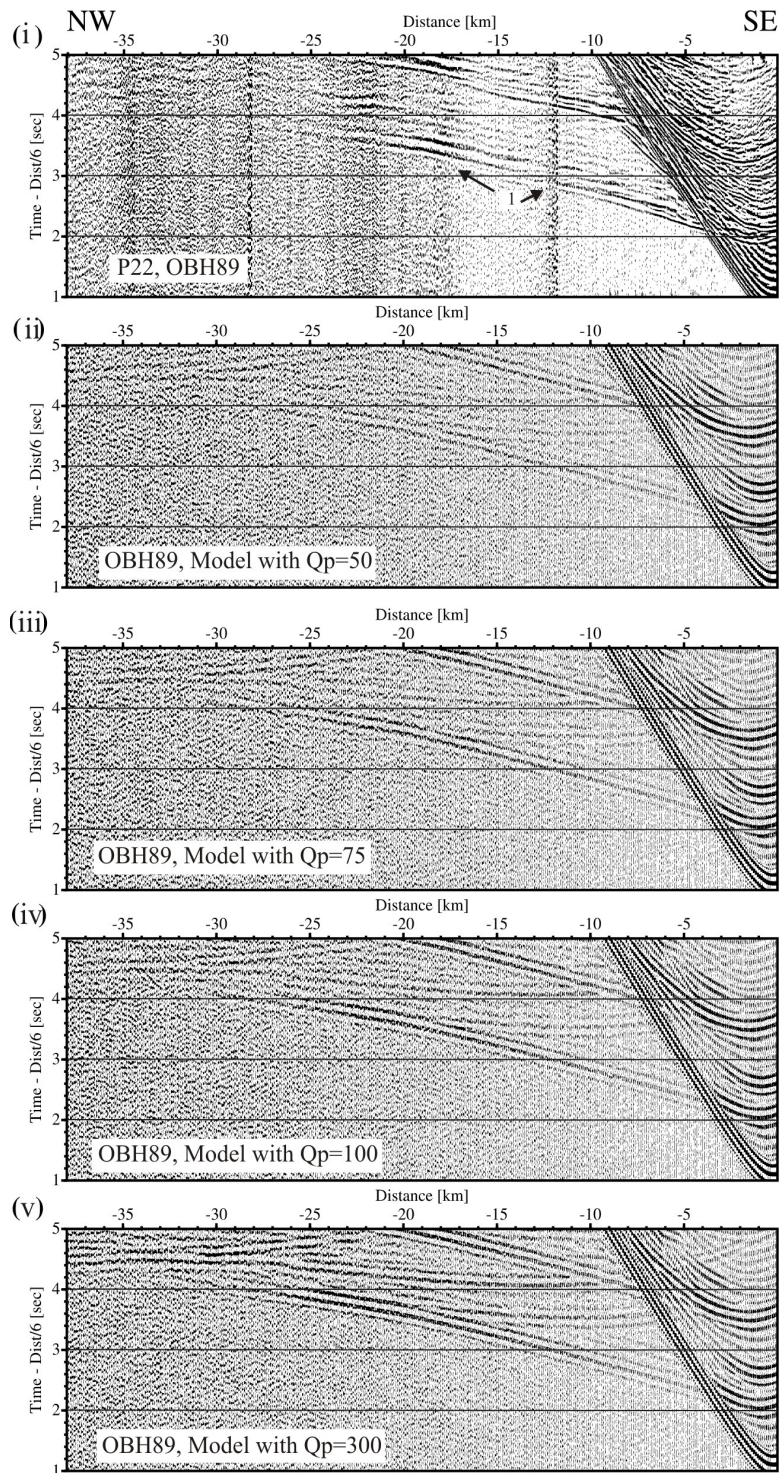


Figure D.6. Synthetic seismogram with different Q_p values for station OBH89.

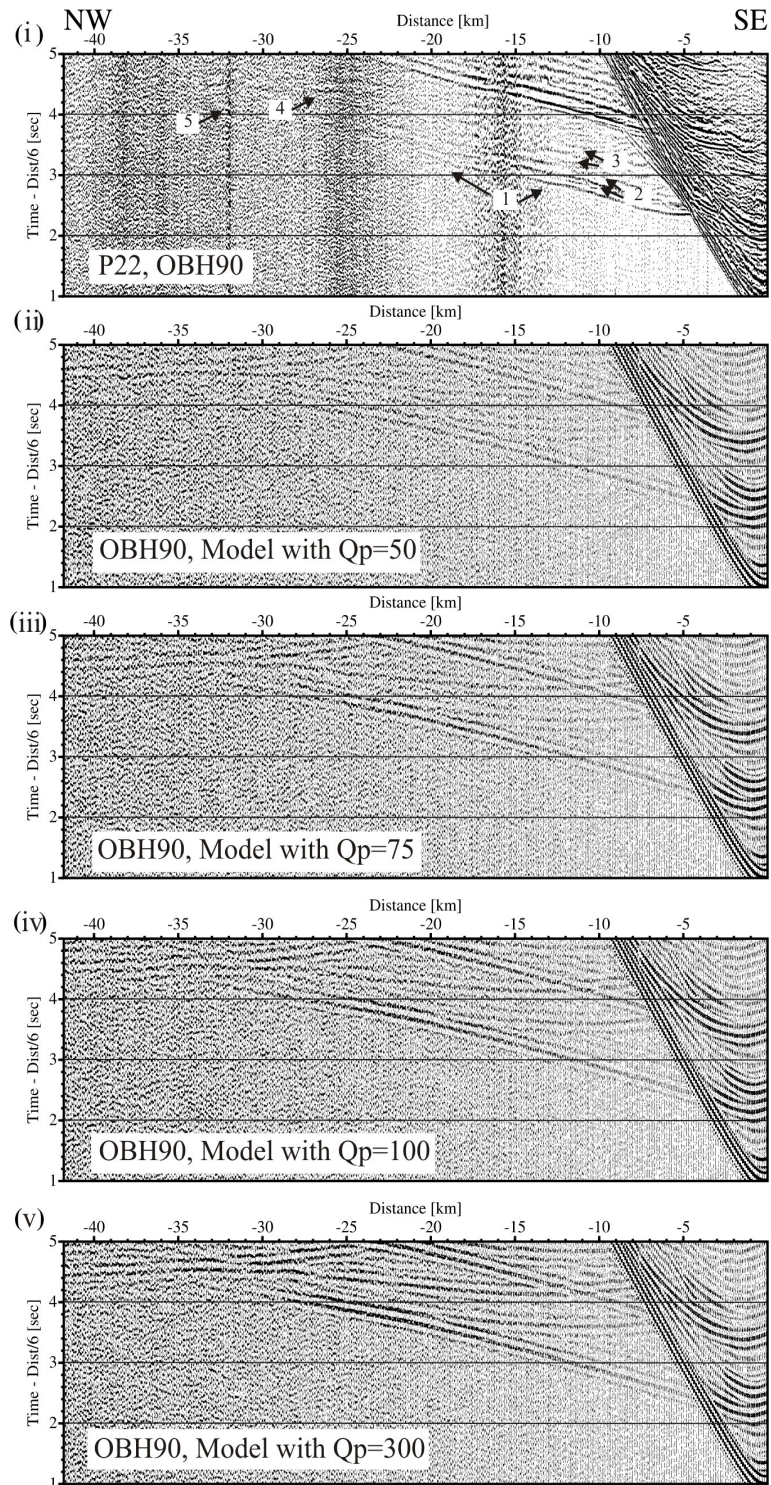


Figure D.7. Synthetic seismogram with different Q_p values for station OBH90.

Curriculum Vitae

Personal data:

Name: Junjiang Zhu

Date and Place of birth: 18 June 1976, Xinjiang, P. R. China

Nationality: P. R. China

Education:

1993-1996 The No.1 Senior Middle School of Shawan County, Xinjiang, P. R. China

1996-2000 China University of Geosciences (Wuhan), Hubei Province, P. R. China

2000-2003 South China Sea Institute of Oceanology, Chinese Academy of Sciences,
Guangzhou, P. R. China

2004-2005 Tongji University, Shanghai, P. R. China

June 2005- September 2005 Goethe-Institut, Goettingen, Germany

Since October, 2005 PhD Student at the Leibniz-Institute of Marine Sciences IFM-
GEOMAR at the University of Kiel, Germany
SFB 574 Volatile und Fluide in Subduktionszonen

Eidesstattliche Erklärung

Hiermit erkläre ich, dass die vorliegende Abhandlung, abgesehen der Beratung durch meine akademischen Lehrer, nach Inhalt und Form meine eigene Arbeit darstellt. Ferner habe ich weder diese noch eine ähnliche Arbeit an einer anderen Abteilung oder Hochschule im Rahmen eines Prüfungsverfahrens vorgelegt.

Junjiang Zhu

Kiel